THE EFFECT OF CEMENT MECHANICAL PROPERTIES AND RESERVOIR COMPACTION ON HPHT WELL INTEGRITY

A Dissertation

by

ZHAOGUANG YUAN

Submitted to the Office of Graduate Studies of
Texas A&M University
in partial fulfillment of the requirements for the degree of

DOCTOR OF PHILOSOPHY

Approved by:

Co-Chairs of Committee,	Jerome J. Schubert
	Catalin Teodoriu
Committee Members,	Gene Beck
	Paolo Gardoni
Head of Department,	A. Daniel Hill

December 2012

Major Subject: Petroleum Engineering

ABSTRACT

In the life of a well, the cement sheath not only provides zonal isolation but also supports casing and increases casing-collapse resistance. Due to the high-pressure, high-temperature (HPHT) conditions, the cement sheath plays an important role in maintaining wellbore integrity. During the production process in HPHT wells, the pressure differential inside the casing and the surrounding formation is larger than the conventional wells. The stress induced by fluid withdrawal in highly compact reservoirs can cause the cement and the casing failure in these wells. These present a greater challenge to the wellbore integrity than the conventional wells.

To have reliable data, extensive experimental work on Class G cement was carried out to measure the principal parameters for mechanical structural calculations. The experiment was also set up to simulate conditions under which cement low-cycle fatigue failure could occur. Zero-based cyclic pressure was applied to the casing in the cement low-cycle fatigue test. Three types of cement (72-lbm/ft^3, 101-lbm/ft^3 and 118-lbm/ft^3) were cured and tested at 300ºF to study the cement mechanical properties under high-temperature conditions over the long term. The tests included a 1-year mechanical properties measurement such as compressive strength development; i.e., Young's modulus and Poisson's ratio. Finite element methods (FEM) were used to study the casing buckling deformation characteristics of reservoir compaction in some south Texas wells.

The 2D and 3D FEM models were built to study the effects of mechanical properties and reservoir compaction on HPHT well integrity. As the confining pressure increases, the cement shows more plasticity and can withstand more pressure cycles. The cement with a higher Poisson's ratio and lower Young's modulus showed better low-cycle fatigue behavior. Casing collapse resistance is very sensitive to void location, cement Poisson's ratio, cement Young's modulus, and pore pressure. Casing eccentricity and voids shape have minor effect on the casing-collapse resistance. Casing shear failure, tension failure, and buckling failure are the most likely failure modes in reservoir compaction. For different casing wall thickness, the critical buckling strain is almost identical.

This study presents a better understanding of casing failure and cement failure in HPHT wells. The results of the study will help improve cement and casing design to maintain wellbore integrity that can in turn be expected to extend throughout the life of the well.

DEDICATION

To my parents- thank you for your support and the values that you have taught me in my life.

ACKNOWLEDGEMENTS

I would like to thank my committee chair, Dr. Jerome Schubert for serving as my advisor and a good friend. Your support and teaching has been invaluable during my studies at the Petroleum Department.

I would like to thank my committee co-chair, Dr. Catalin Teodoriu for serving as my co-advisor. Thanks for your help on the experimental study.

I would like to thank my committee members, Dr. Paolo Gardoni and Dr. Gene Beck for your guidance and support throughout the course of this research.

Thanks also go to my friends and colleagues and the department faculty and staff for making my time at Texas A&M University a great experience. I also want to extend my gratitude to the Crisman Institute for sponsoring my Ph.D study.

Finally, thanks to my mother and father for their encouragement and love.

NOMENCLATURE

A	Cement high- cycle fatigue failure constant
B	Cement high -cycle fatigue failure constant
C	Rock internal strength, psi
C_r	Volumetric solid-grain compressibility, psi^{-1}
C_{bc}	Volumetric bulk-volume compressibility, psi^{-1}
E	Young's modulus, psi
F	Critical force, lbf
G	Cement low- cycle fatigue failure constant
h	Reservoir thickness, ft
HPHT	High pressure high temperature
I	Area moment of inertia
IRR	Internal rate of return
K	Column effective length factor
L	Unsupported length of column, in.
M	Cement low -cycle fatigue failure constant
NPV	Net present value
N_f	Cement cycles to failure
OD	Outside diameter, in
P_c	Casing collapse pressure, psi
P_{f0}	Initial pore pressure, psi

R_b	Wellbore radius, in
R_d	Radius of depletion, ft
S_r	Radial stress, psi
S_θ	Tangential stress or hoop stress, psi
S_{v0}	Initial vertical stress, psi
S_{h0}	Initial horizontal stress, psi
t	Casing wall thickness, in.
v	Poisson's ratio
X	Vector of random variables
γ	Cement low- cycle fatigue failure constant
Z	Cement low -cycle fatigue failure constant
θ	Angle, degree
μ	Internal frictional coefficient
λ_v	Ratio of effective vertical stress and vertical Stress
α	Biot's constant
σ_y	Yield stress, psi
$\sigma_v^{'}$	Effective vertical Stress, psi
$\sigma_1^{'}$	Effective first principal stress, psi
$\sigma_2^{'}$	Effective second principal stress, psi
$\sigma_3^{'}$	Effective third principal stress, psi
σ_1	First principal stress, psi.
σ_2	Second principal stress, psi.
σ_3	Third principal stress, psi.

σ_{eqv}	Equivalent stress, psi.
σ_s	Compressive strength, psi
σ_t	Tensile strength, psi.
ε_p	Plastic strain
ε_1 , ε_2 , ε_3	Multiaxial total strain division
$\Delta\ \varepsilon$	Total strain
$\Delta\ \sigma_1$, $\Delta\ \sigma_2$	Cement low- cycle elastic stress, psi
ΔS_v	Change in vertical stress, psi
ΔP_f	Change in pore pressure, psi
ΔS_h	Change in horizontal stress, psi
ΔP_d	Depletion pressure, psi
ΔP_b	Drawdown pressure, psi

TABLE OF CONTENTS

CHAPTER

CHAPTER

LIST OF FIGURES

Page

LIST OF TABLES

Page

CHAPTER I

INTRODUCTION

1.1 Problem Descriptions and Research Objective

Wellbore integrity problems include cement failure, casing failure, and formation failure. This research focuses on the effects of cement mechanical properties and reservoir compaction on high pressure high temperature (HPHT) well integrity. The cement failure studied here is low-cycle cement-fatigue failure and cementing complications. The problems related to reservoir compaction in a south Texas field are casing failures and formation failures. The cement failure in this field is not considered because the cement bond log shows the cement sheath is in good contact with the casing and the formation.

The Low-cycle cement-fatigue is new to petroleum engineer. Due to the HPHT cycles experienced in the process of hydraulic fracturing, production and stream injection, the failure probability of low-cycle cement fatigue is high in these wells and is likely to cause the failure of the zonal isolation and increase the casing failure probability.

Casing eccentricity, cement voids and cement channels usually are cementing complications in HPHT gas wells. Wellbores with the cementing complications usually have higher cement and casing failure probability than the wellbores without any cement problems. The sensitivities of the cement and formation mechanical properties to stress distribution in casing-cement-formation system, the effects of hole angle, and cement complications on HPHT well integrity are hardly studied.

Casing failure probability is high in a south Texas field. The formation sands are over-pressured where the pore pressure ranges from 0.85 to 0.93 psi/ft. Casing damage has been experienced in over 11 wells from 18 that have been drilled in the area, near 61% of total wells were damaged during their production life. To identify and avoid the casing failure problems in this field is very important for the future drilled wells.

The objective of the research is to study the low-cycle cement-fatigue failure mechanism, the effects of hole angle, and cementing voids, cementing channels on casing-cement-formation system, casing buckling failure, collapse failure and tension failure mechanism in reservoir compaction.

1.2 Methods

1.2.1 Experimental Study

1.2.1.1 Test Sample Preparation

The Class G cement composition is shown in Table 1.

Table 1 Class G cement composition

Class G (oz)	Water (oz)	Water/Cement	Density (lbm/gal)
27.937	21.311	0.45	15.77

The cement mixtures are blended for 10 minutes. The blender, which has a lower rev/min with a paddle-shaped mixer, is shown in Figure 1. After the blending process is completed, the nonhydrated cement mixture was mixed under the API 10B-recommended mixture guidelines.

Figure 1 Cement blender

Figure 2 API mixer

The nonhydrated cement mixture was placed in a conical flask in the mixing chamber (Figure 2) where it was mixed with water with a blender speed of 4,000 rev/min. As this mixing continued

for 15 seconds, all of the dry cement should be inside the chamber. After 15 seconds of initial mixing, the mixing rate was increased to 12,000 rev/min for another 35 seconds. The total mixing time of the cement mixture should be 50 seconds. After the mixing has been completed, the cement mixture is then poured into the curing mold (see Figure 3), which contains nine 2 x 2 x 2-in. blocks.

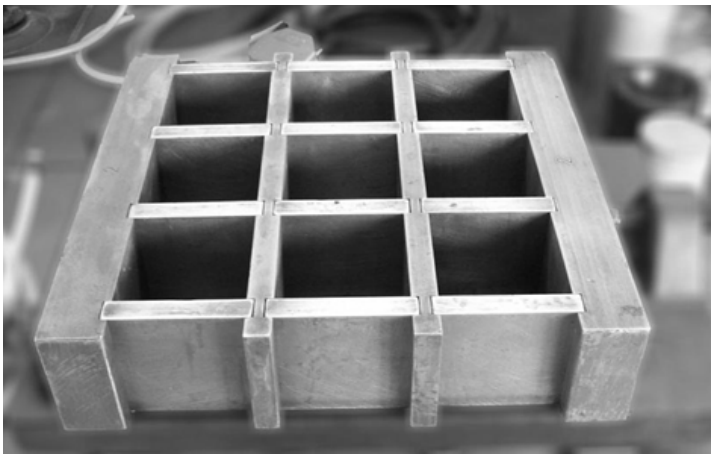

Figure 3 Curing mold

The various cements were cured under three different conditions: (1) room condition; (2) 167°F at atmospheric pressure; (3) 212°F with a pressure of 2,610 psi.

The samples were then placed in an oven, which was held at a temperature of 167^0F under atmospheric pressure. The third condition was made possible by autoclave. The pump filled the autoclave with water and with a pressure of 2,610 psi. Then the autoclave was heated up to 212°F. The 2,610-psi pressure and 212°F-temperature were held constant during the curing time. Additional details are presented in Chapter III.

1.2.1.2 Class G Cement Experimental Tests

Young's Modulus and Poisson's Ratio Measurements

An Ultra-Epoch 4 (Figure 4) is an ultrasonic flaw detector and can be used to measure Poisson's ratio and Young's modulus of the various cements. The Ultra-Epoch 4 can measure the

velocities of shear and compressive waves; thus, Poisson's ratio and Young's modulus can be calculated.

The relationships between the velocities of shear and compressive waves and the material properties of a homogeneous, isotropic, elastic solid are presented in Chapter II. Shear waves do not propagate in liquids and gases; therefore, shear wave velocities in a fluid medium are zero.

Figure 4 Ultra-Epoch 4

Compressive Strength Test

The compressive strength of cement was measured by using a hydraulic press (presented in Chapter III), which has a load range from 0 to 88,185 lbf and an accuracy of 220 lbf.

Tensile Strength Test

The tensile strength test is also called a Brazilian test (Figure 5). The cylinder sample height is 2 in. and the diameter of the cylinder sample is also 2 in. The tensile strength can be calculated by using Equation (1.1):

$$\sigma = \frac{2P}{\pi LD} \tag{1.1}$$

where P is load in lbf, L is sample length in ft, and D is sample diameter in ft.

Figure 5 Brazilian test

Low-Cycle Fatigue Test

In the process of hydraulic fracturing and production, the packer provides an upward force within the casing. Of concern to the operator is that these operations may damage the cement. The cyclic-load test is used to evaluate any damage caused to the cement. For the cyclic-load test, Class G cement was used. In this test, six samples are prepared and the test was performed by using the hydraulic press. The load was increased to a specific load value which was then decreased to zero, and then increased again to a certain value until the sample failed. More details are presented in Chapter III.

1.2.2 Finite Element Methods

The basic steps for finite element methods include building models, meshing, applying boundary conditions, solve, and post-process. In the analysis for our research, 2D and 3D finite element models were built. After the cement mechanical properties were measured, the data can be used as input to study the effect of cement mechanical properties on the HPHT well integrity.

1.2.2.1 2D Structural Elements

PLANE42 Element

The PLANE42 element (Figure 6) is used for 2D modeling of solid structures and can be used as a plane element (plane stress or plane strain) or as an axisymmetric element. The PLANE42 element is defined by four nodes having two degrees of freedom at each node: translations in the

nodal x and y directions. The element has plasticity, creep, swelling, stress stiffening, large deflection, and large strain capabilities.

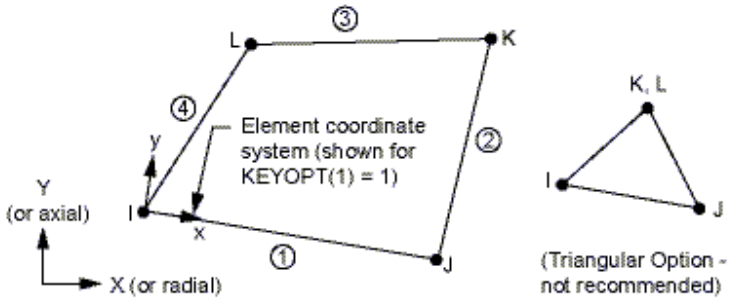

Figure 6 PLANE42 geometry

PLANE82 Element

The PLANE82 (Figure 7), a higher order version of the 2D, four-node element PLANE42, provides improved accuracy compared with PLANE42 for mixed (quadrilateral-triangular) automatic meshes and can tolerate irregular shapes without a significant loss of accuracy. The eight-node elements have compatible displacement shapes and are well suited for modeling curved boundaries.

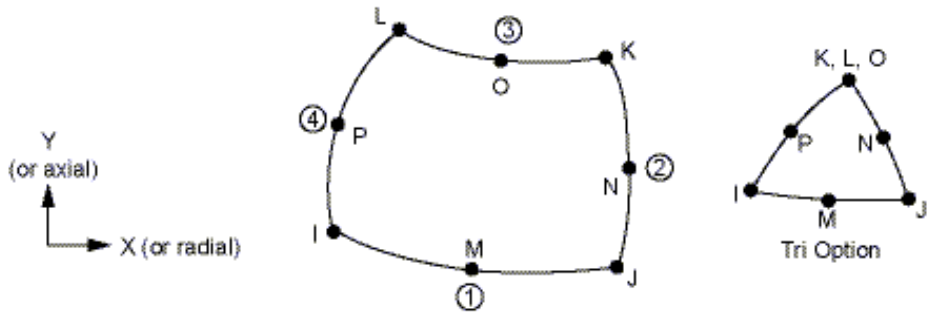

Figure 7 PLANE82 geometry

1.2.2.2 3D Structural Elements

SOLID45 Element

The SOLID45 element (Figure 8) is used for the 3D modeling of solid structures. This element is defined by eight nodes having three degrees of freedom at each node: translations in the nodal x, y, and z directions.

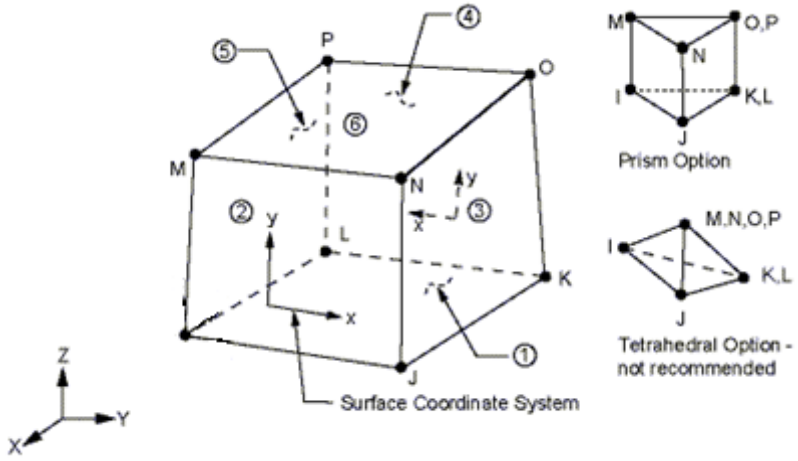

Figure 8 SOLID45 geometry

SOLID95 Element

The SOLID95 element (Figure 9), a higher order version of the 3D eight-node SOLID45 element, can tolerate irregular shapes without a significant loss of accuracy. The SOLID95 element has compatible displacement shapes and is well suited to model curved boundaries. The element is defined by 20 nodes having three degrees of freedom per node: translations in the nodal x, y, and z directions.

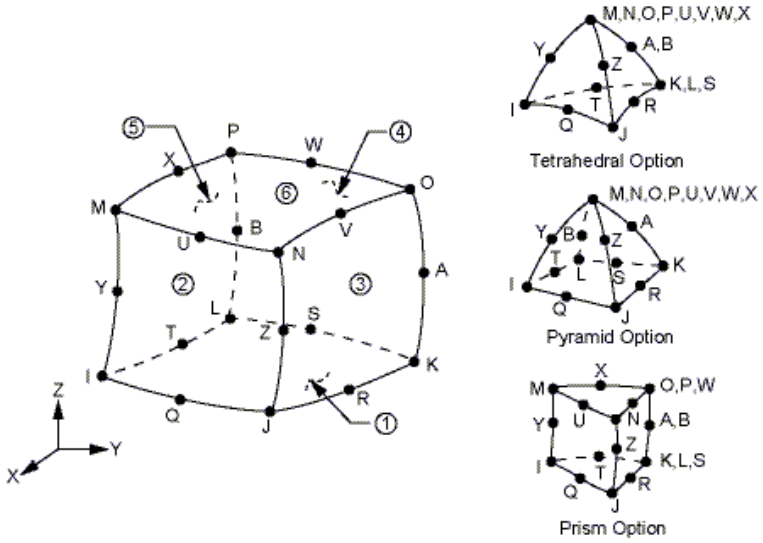

Figure 9 SOLID95 geometry

1.3 Chapter Descriptions

Chapter II presents the testing method and the testing results for Class G cement which is cured under three different conditions. The results of the mechanical properties of Class G cement then are used as the input data for wellbore integrity finite element analysis in Chapter III and Chapter IV.

Chapter III shows the results of the experimental study of low-cycle cement-fatigue failure. Then the test results are used as input data for the theory analysis of low-cycle fatigue under uniaxial-strain ranges and multiaxial-strain ranges, simultaneously, the effects of temperature on low-cycle cement fatigue are studied.

Chapter IV studies the HPHT gas well cementing complications such as cementing voids, cement channeling, and casing eccentricity in two-dimension (2D) and three-dimension (3D) wellbores. The sensitivities of the cement and formation mechanical properties to the wellbore failure probability are analyzed in 2D wells. The effect of hole angle and cementing complications on wellbore integrity are studied in 3D wells.

Chapter V analyzes the cement failure probability of three types of cement (72-lbm/ft^3, 101-lbm/ft^3, and 118-lbm/ft^3) in the Ghawar oilfield in the eastern province of Saudi Arabia. The

highest failure envelopes for each type of cement are plotted and the effects of time on the cement failure probability are also studied.

Chapter VI shows the casing buckling failure characteristics in reservoir compaction. Casing wall thickness, wellbore diameters and unsupported casing lengths are considered as the variables for casing buckling analysis.

Chapter VII studies the casing failure characteristics in a south Texas field. Formation shear failure, fault and facture activated by pore-pressure reduction, and casing tension failure may be the causes for the casing failure in this south Texas field. Workability operational limits are made for each formation based on the study.

Chapter VIII presents the conclusions for each chapter and the discussions for future study.

CHAPTER II

EXPERIMENTAL MEASUREMENTS OF CLASS G CEMENT MECHANICAL PARAMETERS*

2.1 Introduction

Providing zonal isolation for the life of a well and allow the safe and economic production of oil and gas is the main purpose of the annular cement. For an oil/gas well to maintain its integrity and produce effectively and economically, a complete zonal isolation must be achieved during the life of the well. This complete zonal isolation can be compromised due to factors that come into play during the operative life of the completed well. Such factors may come in the form of thermal or pressure loads generally regarded as HPHT loads, which can manifest themselves as static/cyclic loads or both, depending on how they are exerted.

Oilwell cement is subjected to failure mainly by the process of:

- Debonding
- Radial cracking
- Cement plastic deformation

These are not new failure modes but rather a petroleum engineer's term for the usual failure modes in the mechanics of materials. Debonding can also be regarded as shear failure and can exist in two forms; debonding from casing and debonding from the formation. It is however important to note that debonding can also occur as a result of cement shrinkage and in this case, cannot be regarded as a failure due to shear failure. Radial cracking is a failure mode by fracture that results from the gradual growth of cracks when the cement is subjected to fatigue loading. Usually, the surface exhibits no sign of deformation and will finally fail under a gradually increasing load perpendicular to the loading axis in tension and inclined to the loading axis in

compression. Plastic deformation is as a result of yielding failure that usually leads to the shape change of the material involved.

Cook and Young (1999) discuss different classical theories of failure for brittle materials such as maximum normal stress and Mohr-Coulomb's criteria, which may partially define some of the failure modes described previously. These failure criteria are used to predict if a given material, in this case, cement, will fail under a given stress condition. Concrete under triaxial stresses fails in a unique manner and the Mohr-Coulomb's criterion can be used to approximately predict failure when concrete is under compressive and tensile stresses.

The research methods used on oilwell cements can be divided into two categories, laboratory tests and finite element methods. For laboratory tests, one of the earliest testing methods that simulated field conditions was used to test cement-sheath failure (Goodwin and Crook 1992). The cement system was mixed and pumped into the annulus, and then cured at 350ºF by circulating hot (350ºF) oil through the inner casing. The annulus pressure was maintained at 500 psi during the curing phase. The inner casing pressure was increased from 2,000 psi to 10,000 psi in 2000-psi increments. The casing, cement, and formation are assumed to be thermo-elastic materials, and the steel/cement interface and cement/formation interfaces are assumed to be either fully bounded or unbounded (Thiercelin et al. 1997). Two field examples are studied. One field example focuses on the influence wellbore pressure has on the cement behavior and the other example addresses the influence brought about by an increase in wellbore temperature. In subsequent geothermal well studies, plain and fiber-reinforced cements were tested for mechanical properties (Philippacopoulos and Berndt 2001). Selected plain cement formulations were tested in uniaxial and triaxial compression at an elevated temperature of 392ºF. To obtain improved cement mechanical properties for actual field conditions, the cement mechanical properties were measured under wellbore conditions (Reddy et al. 2005) with a temperature of 190ºF and 3,000-psi pressure. Portland- and nonPortland-based cement formulations containing a variety of admixtures and foamed-cement samples were used. Another model with cement cured under higher temperatures was used for testing the long-term HPHT condition on the properties of cements (Stiles 2006). The specimens were placed inside of pressure-curing vessels fitted with threaded caps on both ends. The sealed curing vessels were placed in an oven that had been preheated to 645ºF and were maintained at that temperature for the duration of the curing cycle. Based upon steam tables, the pressure inside of the curing vessels was 2,133 psi at a

temperature of 645ºF. The curing vessels were removed from the oven at time intervals of 1, 2, 4, 8, 12, and 34 months.

For the FEM analysis, FEM models are straightforward to build. Simulating a cement sheath under different operating conditions has been studied extensively because it does not require any special test equipment. What is most important is the input data and selecting the correct FEM model. The best way to study HPHT well cement failure is by combining the laboratory test and FEM methods. Problems associated with conventional cement in the petroleum industry are shear failures and debonding between the cement and casing. The effect of casing eccentricity, voids, cement channels, and pore pressure decline on the collapse resistance of casing was previously studied (Berger et al. 2004). The presence of voids and cement channels can significantly reduce the possibility of casing collapse. The casing eccentricity has a minor effect on casing collapse. A stress-modeling and risk-analysis methodology was proposed using a complementary suite of software tools (Laidler and Taoutaou 2007).The stress distribution in the cement and the casing is well known under different scenarios (Rodriguez et al. 2003; Nabipour and Joodi 2010). However, an experimental study is required to confirm that the simulation results still need to be improved.

A new analytical model (Teodoriu et al. 2010) is capable of determining the cement-casing-rock interaction. It has also been shown that the results are strongly influenced by the quality of cement properties because steel and rock properties are well documented in the literature. Analytical methods, as well as numerical methods, require precise input data to improve the results obtained. Therefore, it is of utmost importance that the properties of well cements be measured, if possible, under in situ conditions. In the following section, attempts to characterize Class G cement are presented; hence, to measure the principal parameters for mechanical structural calculations, including compressive and tensile strength, Young's modulus, and Poisson's ratio.

2.2 Experimental Test Steps

Class G cement is commonly used in western Europe; therefore, our efforts focus on generating an accurate data package for this cement to be used as reference for other cement recipes.

The Class G cement composition had a water cement factor of 0.45 and no other additives had been added. The density of the slurry was 15.77-lbm/gal.

The methods used for measuring mechanical properties are described below.

(1) Sample Preparation

Cement samples were cured in 2-in. by 2-in. metal molds with a height of 5-in. The tops of the samples were cut back to approximately 4-in., and surface grinding equipment was used to prepare the end surfaces once the samples cured and were removed from the molds. The cement was mixed according to API specifications.

The samples were then immersed in autoclaves filled with water, after which the temperature of 212ºF and the pressure of 2,610 psi and pressure were applied. Before performing the measurements, the samples were allowed to cool down and the pressure was removed.

(2) Young's Modulus, Poisson's Ratio, and Compressive Strength Measurement

Conventional unconfined and confined compressive strength tests were performed on cubic samples to determine the compressive strength. The samples tested were nominal 2-in. by 2-in. cubes. The Ultra‑Epoch 4 instrument was used to measure Poisson's ratio and Young's modulus of the various cements. This instrument can measure the velocities of shear and compressive waves; thus, allowing for Poisson's ratio and Young's modulus to be calculated. The relationships between the velocities of shear and compressive waves and the material properties of a homogeneous, isotropic, elastic solid are shown in Equation (2.1) and Equation (2.2). Shear waves do not propagate in liquids and gases; therefore, shear-wave velocities in a fluid medium are zero. Poisson's ratio is calculated using the Equation (2.1).

$$\nu = \frac{1-2\left(\frac{V_T}{V_L}\right)^2}{2-2\left(\frac{V_T}{V_L}\right)^2} \tag{2.1}$$

$$E = \frac{V_L^2 \rho (1+\nu)(1-2\nu)}{1-\nu} \tag{2.2}$$

where V_L = shear (transverse) velocity, ft/sec

V_T = longitudinal velocity, ft/sec

ρ = density, lbm/gal

2.3 Cement Compressive Strength Test

For the Class G cement compressive strength, Figure 10 shows that after one day, the compressive strength is 870 psi, and the compressive strength increased significantly between 1 day and 20 days. After 20 days, the compressive strength increased only slightly with time. For the cement cured at 167ºF, it can be shown that in one day, the compressive strength of Class G cement reached 5,221psi. The compressive strength increased from 5,221 psi at 1 day to 9,282 psi at 14 days, and after that, the compressive strength almost remained constant at 9,282 psi. The compressive strength of Class G cement cured under the conditions of 212ºF and 2,610 psi is 6,817 psi, and then remained essentially constant. The compressive strength at 14 days is basically the same as that at 3 days. Due the low number of samples for the HPHT test, we can only extrapolate that at HPHT conditions, the cement compressive strength will develop rapidly and then remain constant.

All HPHT tests have been performed at a maximum of 40 days curing time, and these tests do not reflect the temperature degradation of cement that is observed in steam injection or geothermal wells.

Figure 11 shows that at room conditions, Poisson's ratio was essentially constant at approximately 0.3. For the cement cured at 167ºF, Poisson's ratio was 0.3 after 3 days and then decreased to 0.2 after 12 days after which time, it remained constant at 0.2. After 14 days of curing under the conditions of 212ºF and 2,610 psi, Poisson's ratio remained constant at 0.2 between 6 and 14 days; however, after 21 days of curing at 212ºF and 2,610 psi, Poisson's ratio did not change significantly.

Figure 12 shows that Young's modulus slightly increases from 1.74E6 psi at 11 days to 2.32E6 psi at 43 days and after 20 days, Young's modulus remained steady at 2.32E6 psi. For the cement cured at 167ºF, the Young's modulus also showed a clear trend; i.e., between 3 and 16 days, Young's modulus increased from 1.74E6 psi to 2.49E6 psi.

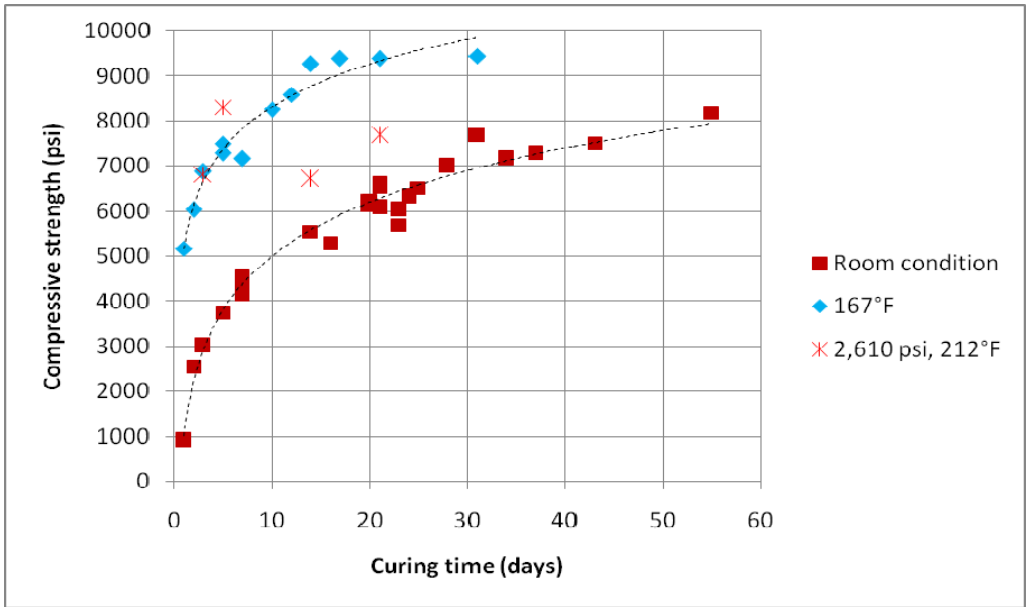

Figure 10 Compressive strength of Class G cement as a function of curing time

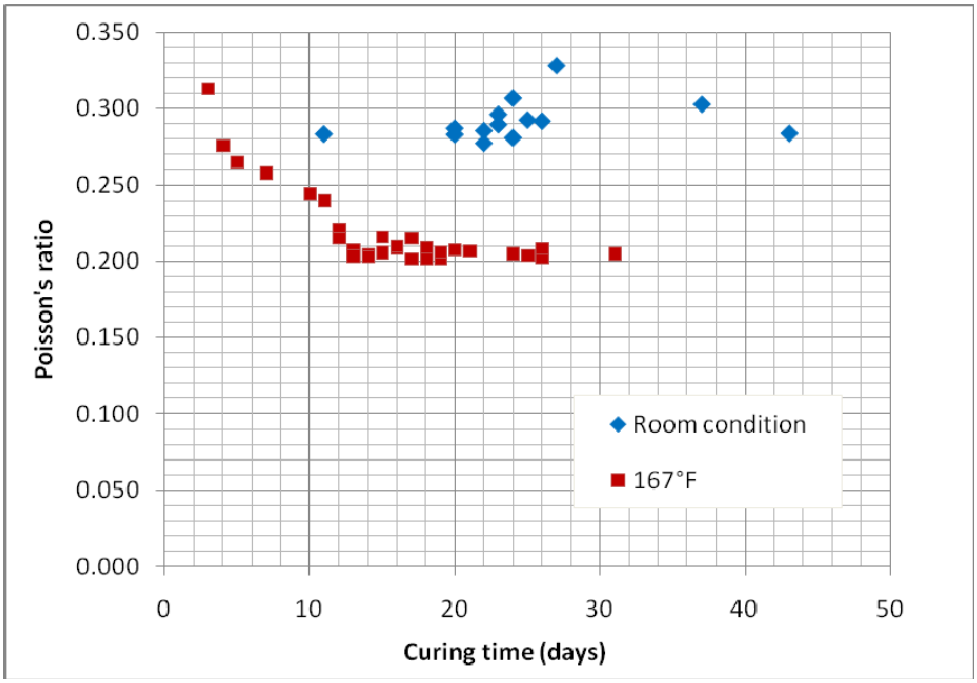

Figure 11 Poisson's ratio behavior for Class G cement

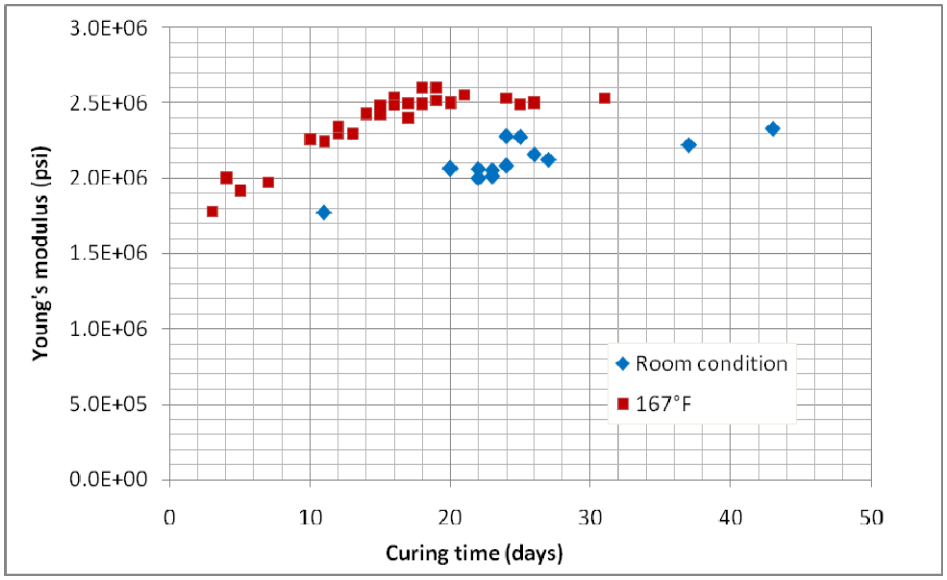

Figure 12 Young's modulus behavior for Class G cement

2.4 Cement Tensile Strength Test

This cement tensile strength test is also known as the Brazilian test. Class G cements were prepared for this particular test. The Class G cements were cured under three different conditions: air under water at room conditions and at 167ºF and dry under water at the same two temperatures. The cylinder sample diameter was 2-in. and its height was also 2-in.. Tensile strength was measured using a Brazilian splitting tensile test after the ASTM D 3967 procedure. Samples, which were split in the center, were cured in cylindrical molds. As shown in Figure 13, the tensile strengths were measured after seven days in which the Class G cement cured at 167ºF had the highest tensile strength value, which is 537 psi. Class G cement cured under water had the second highest tensile strength value, while the Class G cement cured in dry air had the lowest tensile strength value, which was on the order of 363 psi. As the time moved on, at 21 days, the tensile strength of Class G cement cured at 167ºF increased significantly; i.e., it reached 827 psi. For the Class G cement cured under water, the tensile strength at 21 days was almost equal to the one measured at 7 days. The tensile strength is about 15% of the compressive strength. This result is similar to that in the literature.

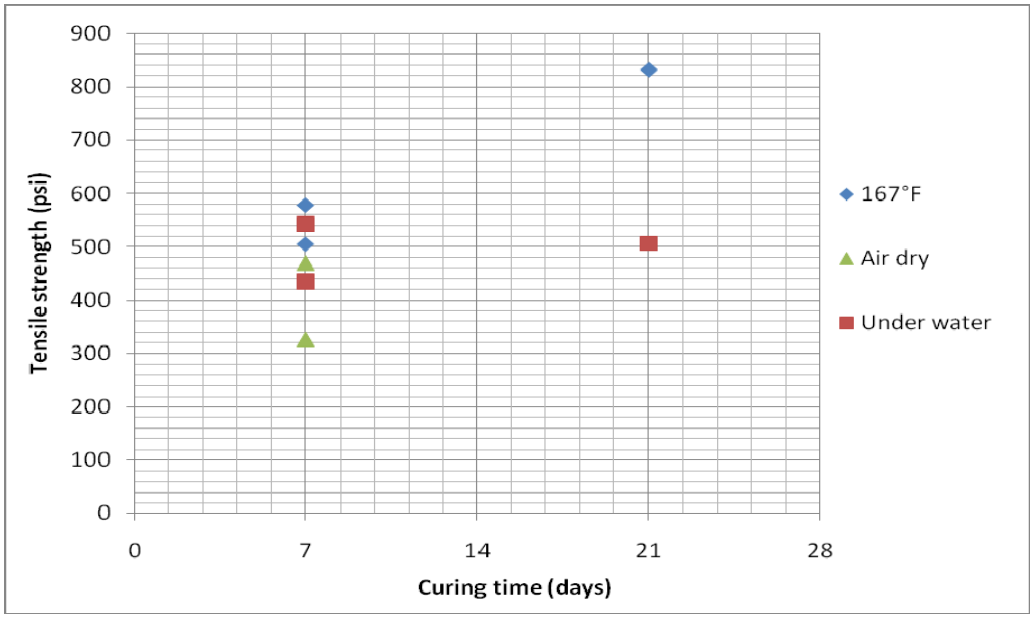

Figure 13 Tensile strength evaluation of Class G cement

2.5 Conclusions and Discussions

2.5.1 Conclusions

The study provides an excellent set of data for Class G cement evaluation that can be used when mechanical studies of cement, such as finite element studies, are required.

It had been observed by this study that under low-temperature conditions, the mechanical properties of cement became independent of time, so that this values (stabilized values) can be easily used for integrity calculations.

The fact that the compressive strength of the cement increased with curing temperature showed stabilization around 10,152 psi. The stabilized Young's modulus is twice the number reported by various authors, but the measured value at the corresponding lower curing time is comparable. Finally, the Poisson's ratio was found to be approximately 0.2.

2.5.2 Discussions

The compressive strength of Class G cement at room temperature reaches a stabilized value of about 9,717 psi after more than 70 curing days. This value should be used for calculations of surface casing-cement interaction. At elevated temperatures, the stabilized compressive strength reaches even higher values, around 10,152 to 10,877 psi.

Both tests showed that if we extrapolate the experimental points, Young's modulus will stabilize at 2.47E6 psi after a longer curing time. This value should be used for further numerical work where the cement is exposed to temperatures less than 167ºF.

Poisson's ratio showed different behavior between the room temperature sample and those samples cured at 167ºF. In this case, the curing temperature plays a very important role. The measured values of Poisson's ratio vary between 0.3 at room temperature and 0.2 at 167ºF. The limited number of HPHT tests on Class G cement reveals that a Poisson's ratio of 0.2 is more than adequate for engineering use when cement properties are considered.

Table 2 Strength parameters of Class G cement reported by various authors

	Wehling, 2008	Morris, 2003	Le, 2000	This work after 72 hr	This work after stabilization
Compressive Strength (psi)	7,107	5,801	5,366	6,962	8,702
Tensile Strength (psi)	290	290	n/a	n/a	435
Young's Modulus (psi)	1.26E6	7.83E5	9.57E5	1.74E6	2.47E6
Poisson Ratio	0.15	n/a	n/a	0.2	0.2

The major problem in comparing these values is the curing time of the cement and the cement additives. It must be noted that our cement samples were Class G cement and fresh water; whereas the reference cement was cured at room conditions. The other investigations used the following curing conditions:

• The samples tested by Morris et al. (2003) were cured at 183.2°F and 2,916 psi pressure and developed the strength of 5,801 within 48 hours.

• The samples tested by Le et al. (2000) were cured at a temperature of 170.6°F and a pressure of 5,366 psi for 72 hours

Our samples were tested up to 60 days and the final values were also extrapolated so that the cement properties became independent of time.

CHAPTER III

LOW-CYCLE CEMENT FATIGUE FAILURE EXPERIMENTAL STUDY AND THE EFFECTS ON HPHT WELL INTEGRITY

3.1 Introduction

Material fatigue includes low-cycle and high-cycle fatigue. The high-cycle fatigue occurs at more than 1,000 cycles and the material deforms at a lower load, usually less than 2/3 of the yield stress. The deformation is in the elastic range. The high-cycle fatigue behavior is usually described by the Stress-N equation. The typical cement paste high-cycle fatigue equation is given as follows:

$$Log(N_f) = A\frac{\sigma}{\sigma_s} + B \text{ , (Typically, A=-0.109, B=11.4)} \quad (3.1)$$

The low-cycle fatigue in the life of cement occurs below approximately 1,000 cycles. The primary parameter governing the life of the cement appears to be plastic strain per cycle as measured on a gross scale. For greater cement life, elastic strain also assumes importance; perhaps the governing variable is still plastic strain per cycle, but the plastic strain is highly localized at imperfections in the structure and difficult to measure or compute. At approximately 1,000 cycles and above, it becomes more appropriate to regard total strain-elastic plus plastic as the primary variable.

The theory of thermo-poro-elasticity was used to predict the various modes of cement failure. A stress-modeling and risk-analysis methodology was proposed using a complementary suite of software tools (Laidler and Taoutaou 2007). However, rarely is research performed on cement fatigue and cement failure in the field of petroleum engineering. In the area of cyclic steam-injection wells, there has been some research performed on casing fatigue and casing failure. Experiment and numerical model were built to study the casing thermal stress in steam-injection wells (Joao et al. 1997). The material properties were measured at different temperatures and used as input data for the numerical simulation. The casing-fatigue life is about 80 cycles for some steam-injection wells (Jiang et al. 2008). Two equations, Nerber's rule and the Mansion equation, were used to predict the low-cycle casing failure in the study. The local stress/strain

concept was applied to predict low-cycle casing fatigue exposed to various loads (Teodoriu et al. 2008). The prediction shows an acceptable match with the experimental results.

Some researchers have carried out research on cement- and concrete-fatigue failure in the field of civil engineering. There are some experiments that have been performed on the fatigue failure of Portland cement concrete and paving concrete. The cement-fatigue behavior was studied by changing the water cement ratio (Antrim 1968). He found that the preexisting cracks in the cement paste with higher porosity required a longer time to develop. This result was attributed to the less brittle nature of the cement paste when it contained a large amount of porosity, which helps in the adaptation to the stress fields. Murdock (1965) proposed that the behavior of materials containing cement-hardened paste was controlled by the deformation capacity of their structure. When this capacity was worn out by the fatigue cycling, the specimen broke.

The fatigue behavior of cement-hardened paste in compression loading was studied in detail (Alliche and Francois 1986). The samples were immersed in water at room temperature. The deformations of the specimens during fatigue in compression display three stages. The first stage corresponds to an increase of both axial and radial deformations. During the second stage, which occupies most of the cement's life, the rate of longitudinal deformation remains constant while there is almost no radial deformation. During the third stage, the maximum deformation increased suddenly and shortly before the complete failure of the specimen.

The flexural fatigue behavior of cement was investigated under conditions of constant stress by Joshi et al. (2004). Test results showed that grouped fatigue data followed a log-normal distribution. In orthopedic biomechanics, the probabilistic method was used to analyze the risk of failure of a cemented femoral component of a total hip replacement system and cement mantle of acetabular replacements (Daniel et al. 2001; Nikolaus et al. 2007). The uncertainty and variability in critical system parameters such as joint loading, material properties, and failure properties are considered in the computational model.

The low-cycle cement fatigue is still new in the petroleum industry and much more research needs to be carried out to better understand the process. This study proposed the use of some laboratory test ideas and results and used low-cycle fatigue equations, combining the finite element methods to predict cement failure according to the field conditions.

3.2 Low-Cycle Cement Fatigue Experimental Test

3.2.1 Cement Mechanical Property Measurement

Class G cement was mixed with a water/cement ratio of 0.45 and density of 15.77-lbm/gal. The cements will be cured under three conditions: (1) room conditions; (2) 167ºF temperature and at atmospheric pressure; (3) 212ºF temperature with 2,610-psi pressure. The samples cured under the second condition were placed in the oven, which is held at a temperature of 167ºF at atmospheric pressure. The third condition was made possible by use of an autoclave (Figure 14).

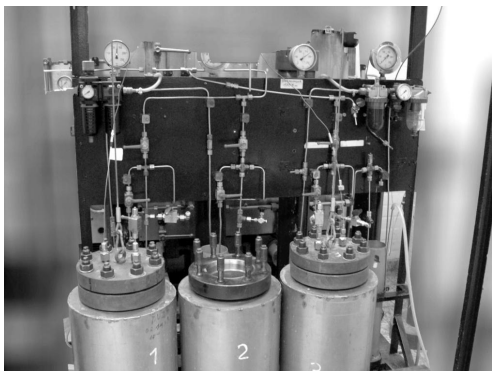

Figure 14 Auto-Clave

The pump filled the autoclave with water and provided a pressure of 2,610 psi. Then the autoclave was heated up to 212ºF. The pressure of 2,610 psi and temperature of 212ºF was held constant during the curing time. All of the cement samples were cured for two weeks. The cement mechanical Young's modulus, Poisson's ratio, and compressive ultimate strength were measured at the end of the two-week period.

3.2.2 Low-Cycle Cement Fatigue Test

In cyclic steam-injection wells, the steam is injected into the well periodically, and the casing and cement may have fatigue failure due to the HPHT conditions. Also, in the process of hydraulic fracturing and production, the cement may experience very high temporary pressure,

which can cause the cement to fail. These operations may damage the cement. Cyclic load testing is being used to study the cement damage.

Class G cement was mixed for this test. The composition is in the same cement-to-water ratio as the cement prepared for the mechanical property test. In this test, six samples will be prepared as shown in Figure 15. The sample dimensions are shown in Table 3 and Figure 16. The samples were cured under room condition for two weeks.

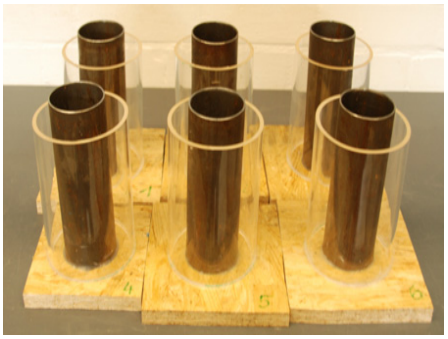

Figure 15 Low-cycle cement test samples

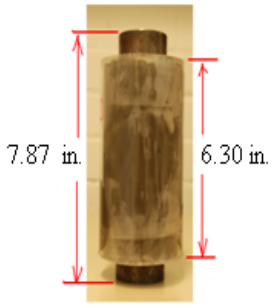

Figure 16 Low-cycle cement sample dimensions

Table 3 Low-cycle cement sample dimensions

Casing ID (in.)	Casing OD (in.)	Wellbore ID (in.)	Cement Length (in.)	Casing Length (in.)
2.60	2.76	4.33	6.30	7.87

The low-cycle cement fatigue test was carried out by using a hydraulic press (Figure 17). The applied load is zero-based cyclic force (Figure 18). The load was increased to a predetermined value, then released to zero, then increased to the same value and released to zero multiple times until the sample fails. The load force was set to 55,115 lbf and 77,162 lbf to evaluate and determine the cement low-cycle fatigue failure characteristics.

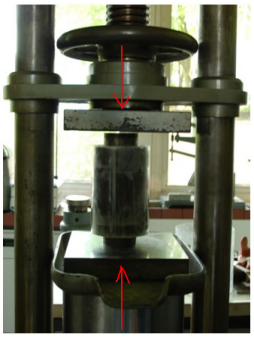

Figure 17 Hydraulic press

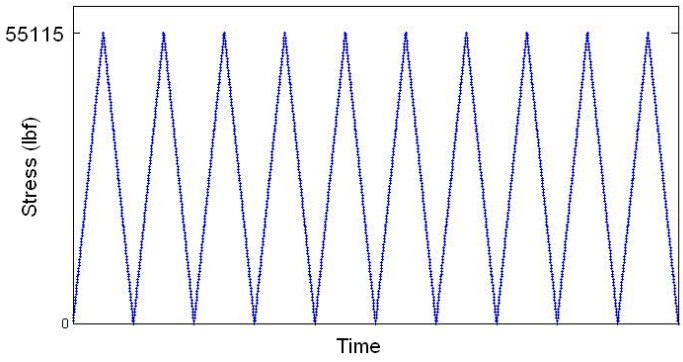

Figure 18 Zero-based cyclic load

3.2.3 Experimental Test Results

The mechanical properties for the cement cured under three conditions are shown in Table 4. The cement cured at 167ºF and 14.7 psi has the highest Young's modulus, compressive strength, and the lowest Poisson's ratio compared to the cement cured under the other two sets of conditions. For the cement cured at 212ºF and 2,610 psi, the class G cement shrinkage was clearly observed. The low-cycle fatigue experimental test results are shown in Table 5. At the zero-based load of 55,115 lbf, the samples failed at an average of 15 cycles. When the zero-based load was increased to 77,162 lbf, the samples failed in an average of 4 cycles. A failed sample is shown in Figure 19.

Table 4 Cement mechanical property test results

Curing Conditions	Young's Modulus (psi)	Poisson's Ratio	Compressive Strength (psi)
Room Condition	2.2050e6	0.30	8085
167ºF, 14.7 psi	2.6460e6	0.20	8820
212ºF, 2,610 psi	2.3520e6	0.26	8232

Table 5 Low-cycle fatigue experimental test results

Load (lbf)	Cycles	Conditions
55,115	15	Failure
55,115	17	Failure
55,115	14	Failure
77,162	4	Failure
77,162	5	Failure
77,162	4	Failure

Figure 19 Low-cycle failed cement sample

3.3 Finite Element Analysis

3.3.1 Cement Behavior under High Confining Pressure

Before the finite element analysis, it is important to know the cement behavior under high-confining pressure and low-cycle fatigue. The cement triaxial test shows the plastic behavior when the confining pressure is very high (Philippacopoulos and Berndt 2001). Usually, the primary parameter governing the material low-cycle fatigue is plastic strain. In the study, the plastic strain is also used as the primary parameter for the cement low-cycle fatigue. There are

many plastic models that describe the material cyclic behavior. The cyclic behavior is quite different among materials.

The application of an alternating pattern of external mechanical or thermal loading does not always result in a cyclically repetitive condition of stress and strain. The materials are divided into cyclically strain-hardening materials and cyclically strain-softening materials. The effect of strain hardening corresponds to hardening of material response; more accurately to increase the resistance to deformation of the material subjected to cyclic loading.

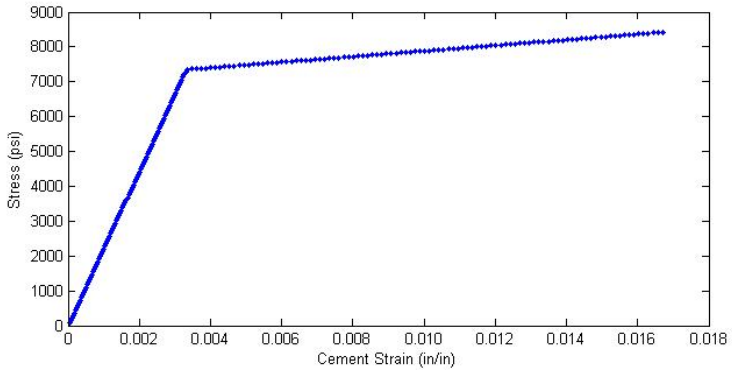

Figure 20 Cement bilinear isotropic behavior
(Room conditions and 4,000 psi confining pressure)

The cement plasticity behavior is shown by bilinear isotropic hardening (Figure 20). The bilinear stress-strain curve requires the input of yield strength and tangent modulus. The slope of the first segment in the curve is equivalent to the Young's modulus of the material while the slope of the second segment is the tangent modulus. The bilinear isotropic-hardening model correctly reproduces the plastic behavior of the cement. The material cyclic-hardening behavior is not considered in the cement-fatigue analysis because the cement cyclic-hardening behavior is not seen clearly in the test. The characteristic of the bilinear isotropic model that the peak stress and shape of the cyclic hardening remain the same even after several cycles make the bilinear isotropic model a good choice to describe the cement plastic behavior.

3.3.2 Cement Strain and Stress

ANSYS was the platform used to develop codes for the FEM analysis to calculate cement strain and stress distribution. The interface between the casing and the cement is assumed to be perfectly bonded. Element SOLID45 is used for the 3D modeling of solid structures. The element is defined by eight nodes having three degree of freedom at each node. The element has plasticity, creep, swelling, stress stiffening, large deflection, and large strain capabilities.

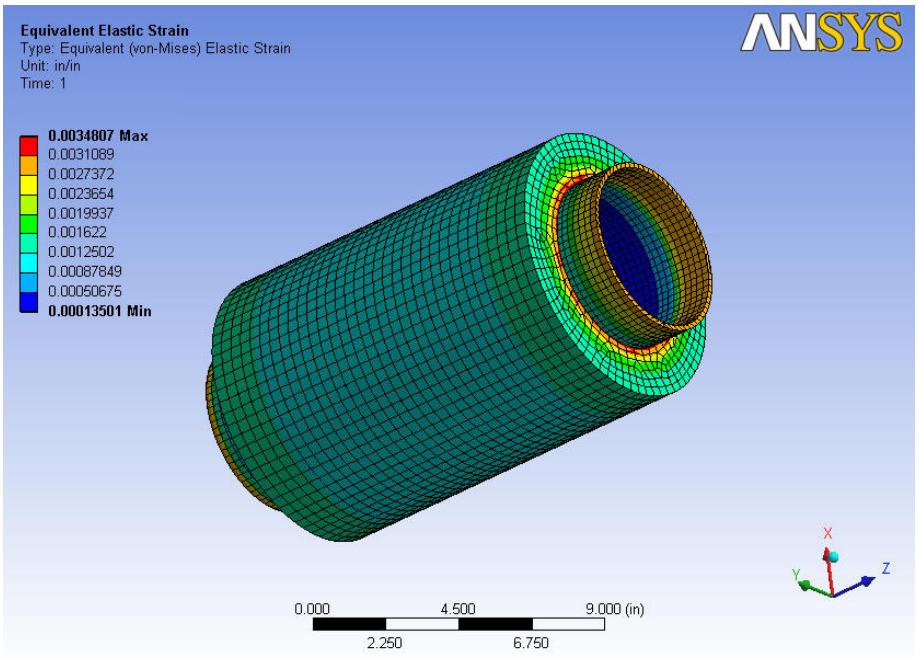

Figure 21 Cement elastic strain at a confining pressure of 4,000 psi and a force of 55,115 lbf

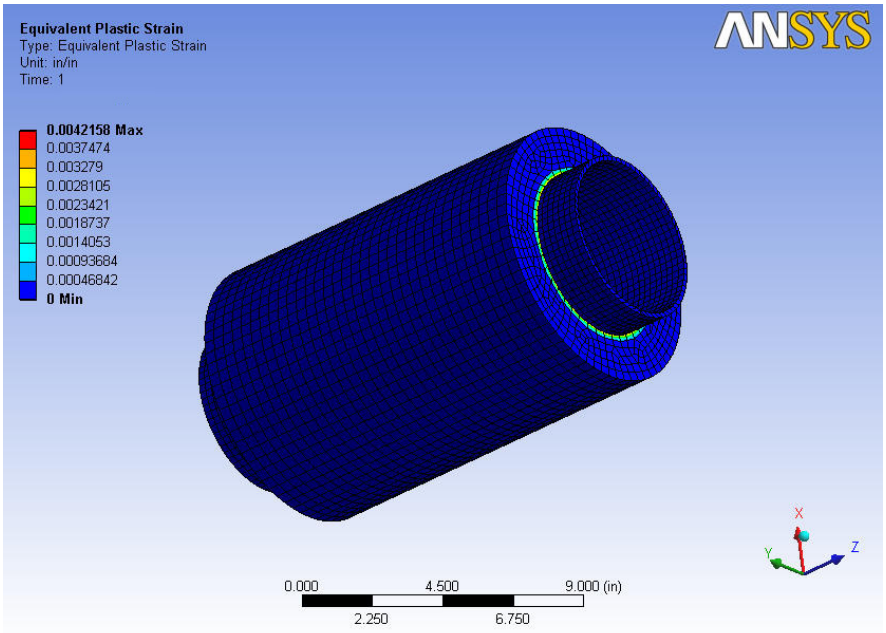

Figure 22 Cement plastic strain at a confining pressure of 4,000 psi and a force of 55,115 lbf

According to the simulation results shown in Figure 21 and Figure 22, for the cement cured for 14 days at different loads and number of cycles, the elastic-strain and plastic-strain distribution in the cement can be determined.

3.4 Low-Cycle Cement-Fatigue Results

3.4.1 Low-Cycle Fatigue under Uniaxial-Strain Ranges

Without confining pressure, this test falls in the uniaxial-strain ranges. The equations describing the low-cycle cement fatigue are as follows:

$$\Delta\varepsilon = \varepsilon_p + \frac{\Delta\sigma}{E} = MN_f^z + \frac{G}{E}N_f^\gamma \qquad (3.2)$$

The constants M, z, G, and γ are regarded as properties that vary from material to material and which can be best determined experimentally from strain-cycling test. The four constants can be determined from tests at only two fixed strain-range levels. If the cement total strain, cement

elastic stress, and fatigue cycles at two points are known, then the constants for Equation 3.2 can be calculated by the following equations.

$$\gamma = \frac{\log(\Delta\sigma_1) - \log(\Delta\sigma_2)}{\log N_1 - \log N_2} \tag{3.3}$$

$$G = \Delta\sigma_1 N_1^{-\gamma} \tag{3.4}$$

$$z = \frac{\log\left(\Delta\varepsilon_1 - \frac{\Delta\sigma_1}{E}\right) - \log\left(\Delta\varepsilon_2 - \frac{\Delta\sigma_2}{E}\right)}{\log N_1 - \log N_2} \tag{3.5}$$

$$M = \left(\Delta\varepsilon_1 - \frac{\Delta\sigma_1}{E}\right) N_1^{-z} \tag{3.6}$$

In the study, data from Table 6, test results, and FEM analysis, the plastic strain and elastic strain can be calculated separately according to the load and cycles. Then, the four constants are expressed as follows:

$$\gamma = \frac{\log\left(\frac{\varepsilon_{e1}}{\varepsilon_{e2}}\right)}{\log\left(\frac{N_{f1}}{N_{f2}}\right)} \tag{3.7}$$

$$G = \frac{\varepsilon_{e1} \cdot E}{N_{f1}^{\gamma}} \tag{3.8}$$

$$z = \frac{\log\left(\frac{\varepsilon_{p1}}{\varepsilon_{p2}}\right)}{\log\left(\frac{N_{f1}}{N_{f2}}\right)} \tag{3.9}$$

$$M = \frac{\varepsilon_{p1}}{N_{f1}^{z}} \tag{3.10}$$

With zero confining pressure, the Stain-N relationship is shown in Figure 23. It is clear that the Strain-N relationship is almost identical to the cement cured under the three previously defined conditions.

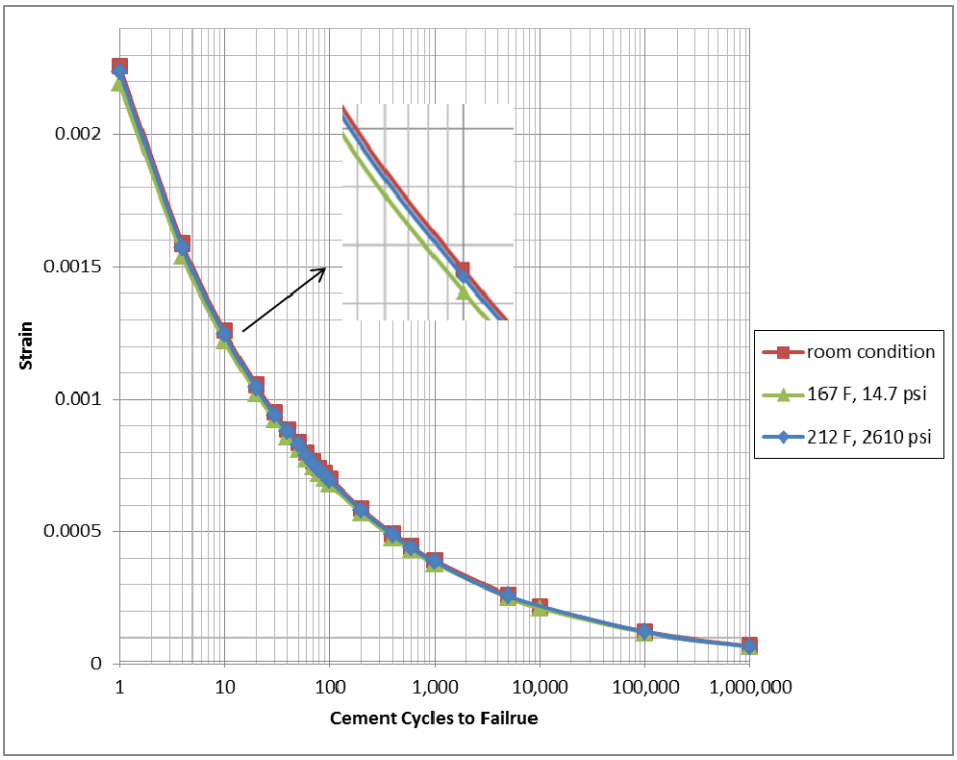

Figure 23 Cement low-cycle Strain-N semi-log plots (zero-confining pressure)

The minor difference in the curves is that with the same strain, the cement cured under room conditions has a slightly greater number of cycles than the cement cured under the other conditions.

3.4.2 Low-Cycle Fatigue under Multiaxial-Strain Ranges

The equivalent strain ε_p is calculated by using strain differences.

$$\Delta\varepsilon = \frac{\sqrt{2}}{3}\sqrt{\left[\Delta\left(\varepsilon_1 - \varepsilon_2\right)\right]^2 + \left[\Delta\left(\varepsilon_1 - \varepsilon_3\right)\right]^2 + \left[\Delta\left(\varepsilon_2 - \varepsilon_3\right)\right]^2} \qquad (3.11)$$

Under multiaxial conditions,

$$\varepsilon_1 = \frac{\Delta\sigma}{2E} + \frac{\varepsilon_p}{2} \tag{3.12}$$

$$\varepsilon_2 = \varepsilon_3 = -\frac{\mu\Delta\sigma}{2E} - \frac{1}{2}\cdot\frac{\varepsilon_p}{2} \tag{3.13}$$

Then

$$\Delta\varepsilon = \varepsilon_p + \frac{2}{3}(1+\mu)\frac{\Delta\sigma}{E} = MN_f^z + \frac{2}{3}(1+\mu)\frac{G}{E}N_f^\gamma \tag{3.14}$$

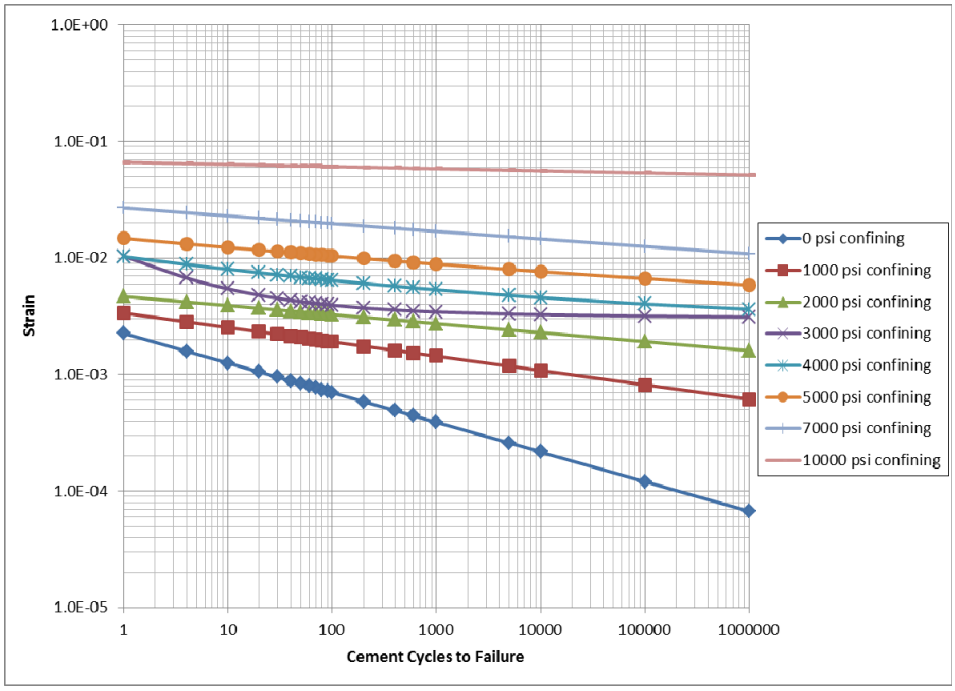

Figure 24 Cement low-cycle Strain-N log-log plots (cement under room conditions)

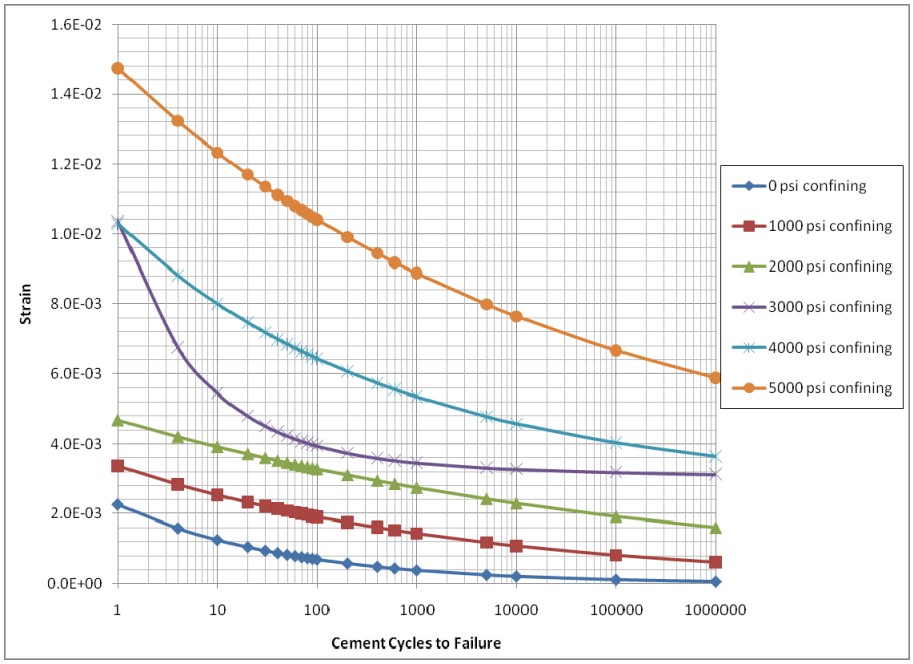

Figure 25 Cement low-cycle Strain-N semi-log plots (cement under room conditions)

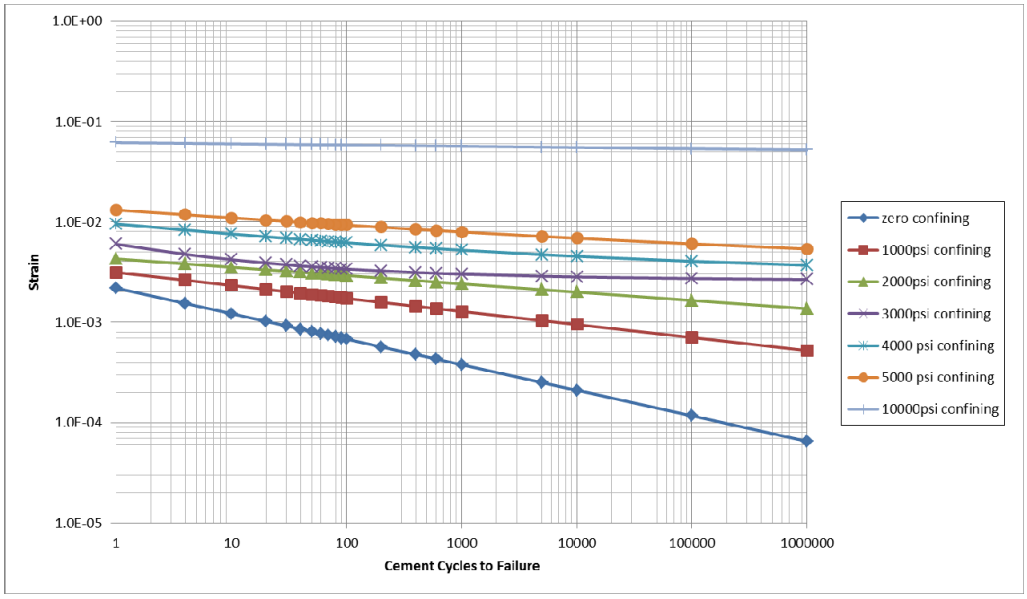

Figure 26 Cement low-cycle Strain-N log-log plots (cement under 167ºF temperature and 14.7-psi pressure)

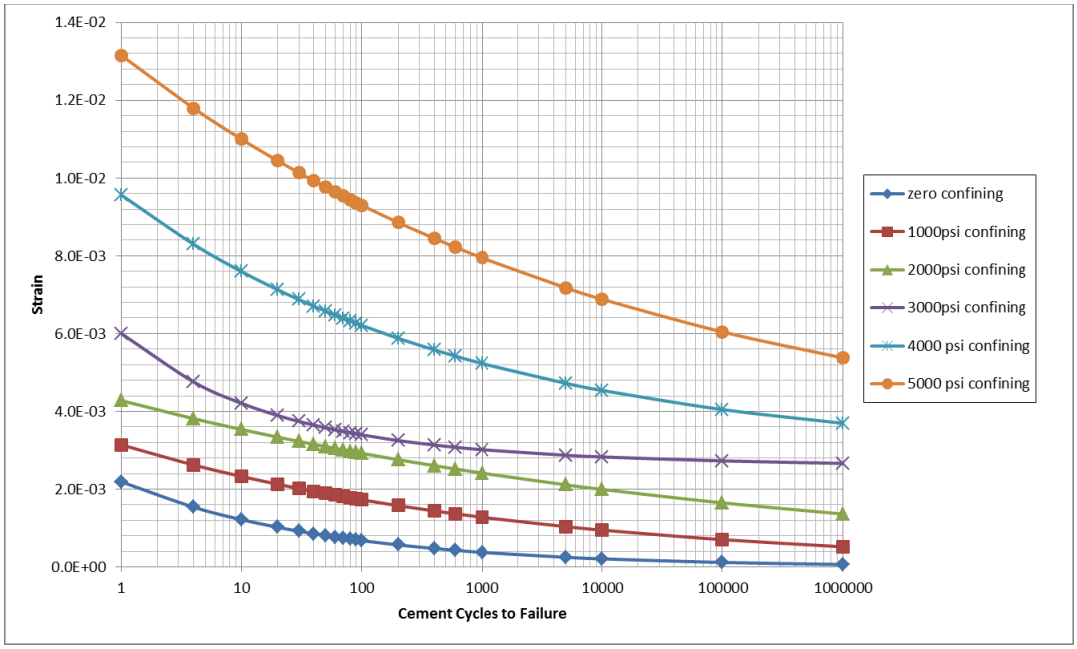

Figure 27 Cement low-cycle Strain-N semi-log plots (cement under 167ºF temperature and 14.7-psi pressure)

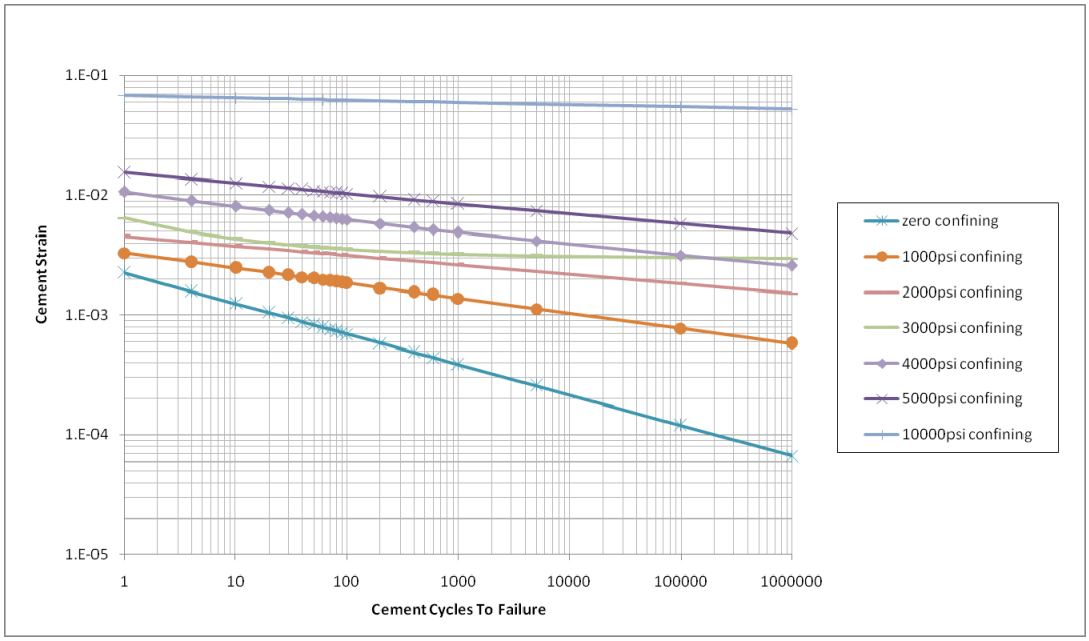

Figure 28 Cement low-cycle Strain-N log-log plots (cement under 212ºF temperature and 2,610-psi pressure)

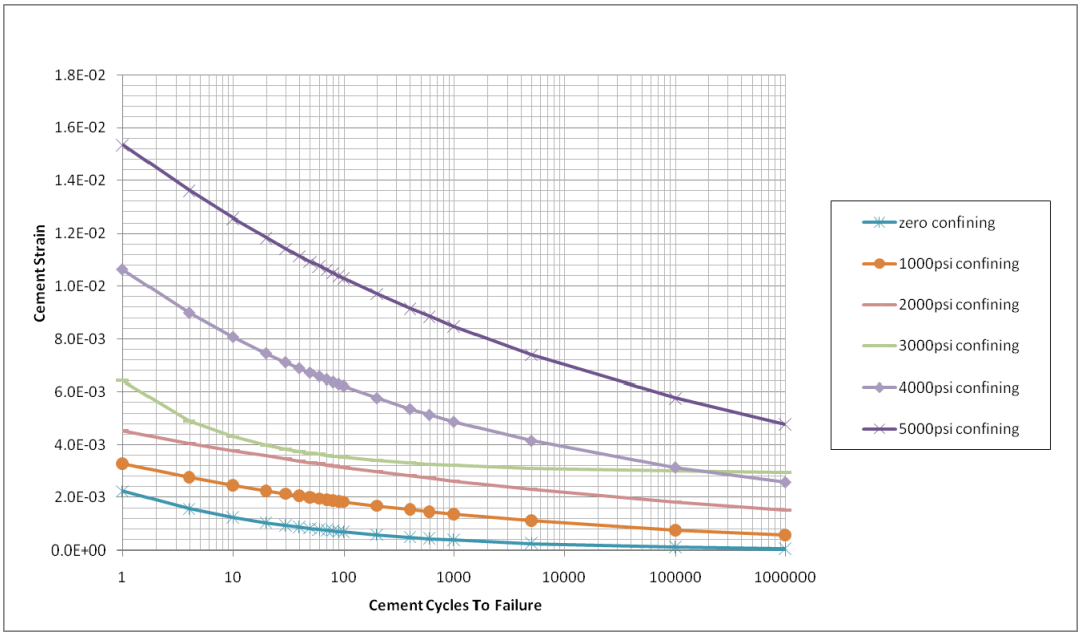

Figure 29 Cement low-cycle Strain-N semi-log plots (cement under 212ºF temperature and 2,610-psi pressure)

Figure 24 to Figure 29 show that as the confining pressure increases, at the same amount of strain, the cement's available life cycle increases. This result is beneficial for the high-pressure wellbore conditions. At the confining pressure below 3,000 psi, the cement does not show any plastic behavior, which means the plastic strain ε_p is zero. As the confining pressure increases above 3,000 psi, the cement shows significantly more plastic behavior.

3.4.3 Comparison of Cements Cured under Different Conditions

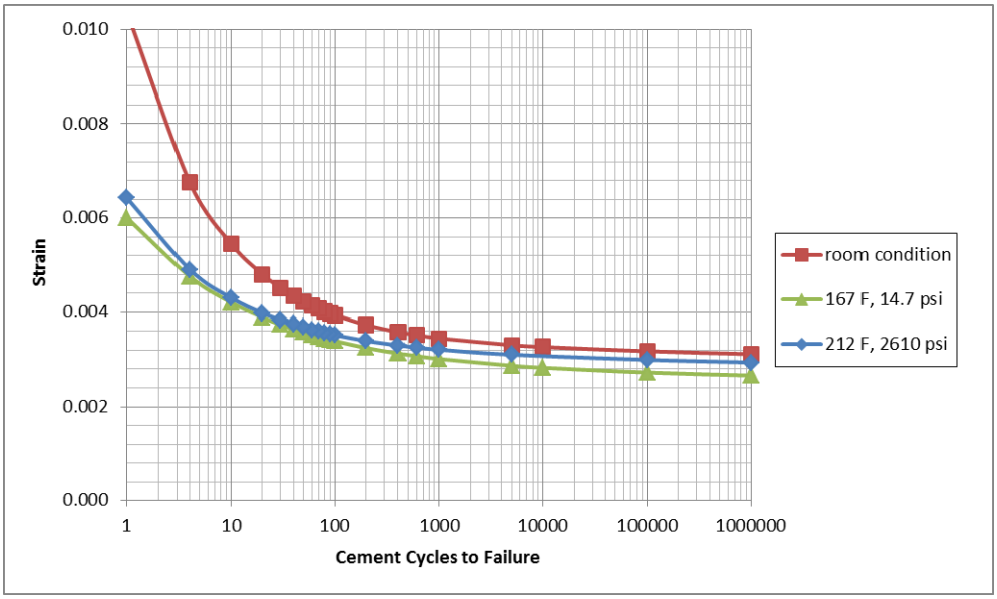

Figure 30 Cement low-cycle Strain-N semi-log plots (4,000-psi confining pressure)

From Figure 30, at the same confining pressure of 4,000 psi, the cement with the higher Poisson's ratio and lower Young's modulus shows better low-cycle fatigue behavior. The room condition-cured cement has the highest Poisson's ratio and at the same strain level, this type of cement has the highest number of available cement cycles.

3.4.4 Temperature Effects

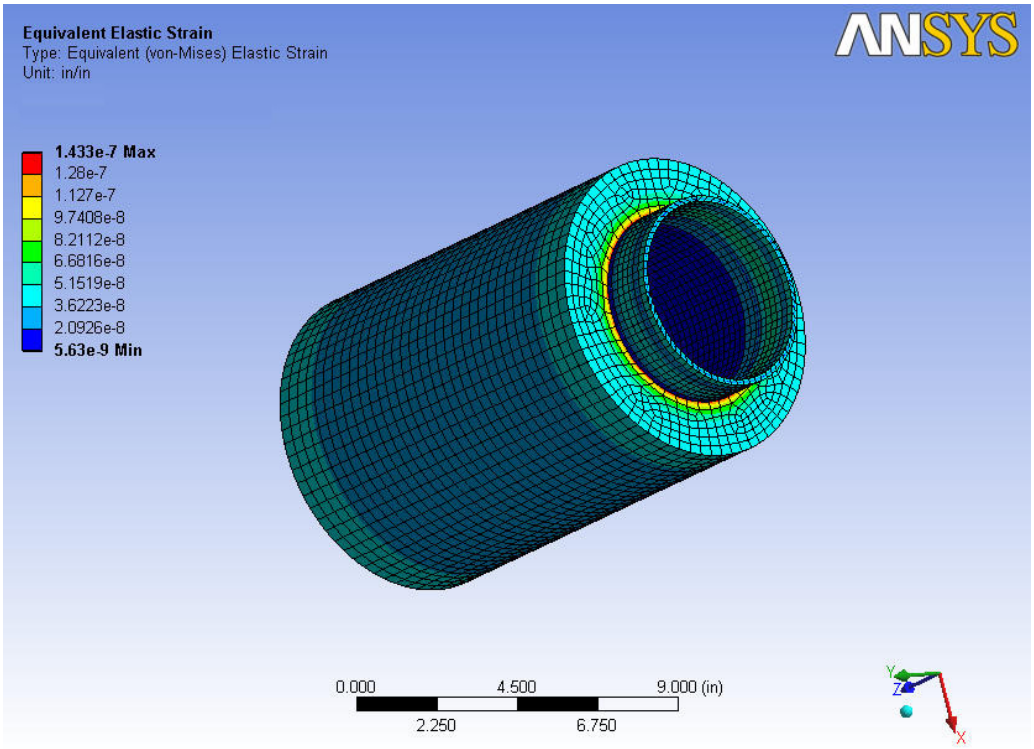

Figure 31 Elastic strain distribution at 300ºF

For metal fatigue, most of the reported effects of cyclic plasticity are a function of temperature. With an increase in temperature, the influence of strain rate on the material response is enhanced. For HPHT wells, the bottomhole temperature can reach nearly 400ºF or more. At temperatures less than 300ºF, the temperature has minor effects on the cement low-cycle fatigue. As shown in Figure 31, the maximum elastic strain developed on the cement is 1.433E-7, which is very small compared to the elastic strain with a magnitude of 1E-4 at zero confining pressure and 55,115-lbf load. The plastic strain developed by thermal stress is zero, and the temperature has minor effect on the cement low-cycle fatigue.

3.5 Field Prediction

The low-cycle cement fatigue can be applied in the field to predict cement failure probability. The following wellbore conditions are in a typical HPHT gas well in south Texas, which produces gas from a sand formation. The well depth is 16,000 ft with a pore-pressure gradient of 0.64 psi/ft. Casing used in the well completion of the 6-in wellbore was 23.2 lb/ft, 5-in. OD, Grade P110. The mechanical properties of Class G cement cured under 212ºF and 2,610 psi were used in the simulation to study the effects of cement low-cycle fatigue on the wellbore integrity. Details on the casing, cement, and formation mechanical properties can be found in the previous study by Yuan et al. (2012a).

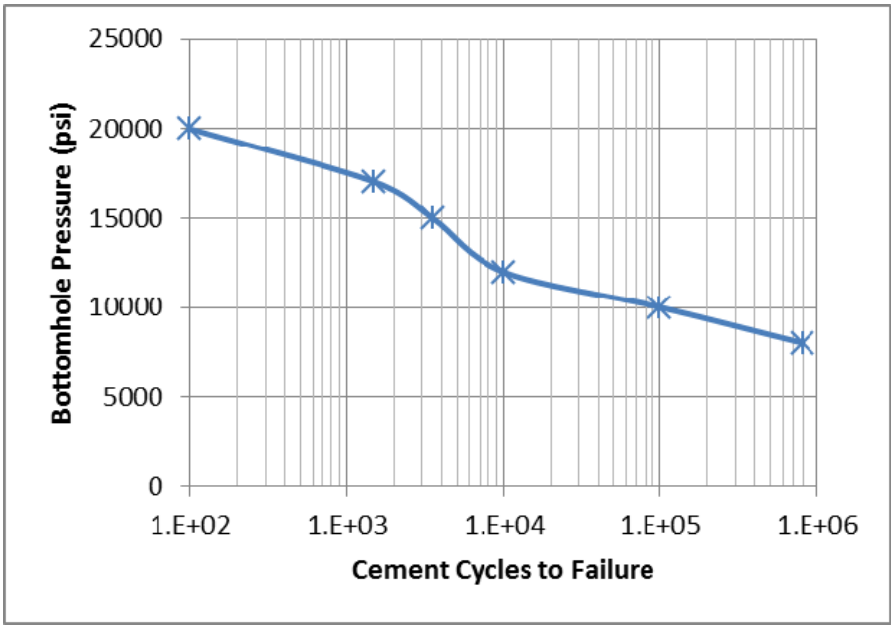

Figure 32 Cement low-cycle Strain-N semi-log plot of cement cycles to failure

With an original pore pressure of 10,200 psi, after reducing the pore pressure to 5,000 psi, the cement confining pressure was found to also be 5,000 psi. The relationship between bottomhole pressure and cement cycles-to-failure is shown in Figure 32. With the bottomhole pressure beyond 15,000 psi, the cement cycles-to-failure decreases to less than 1,000 psi. Under a bottomhole pressure greater than 20,000 psi, the cement will very likely fail.

3.6 Conclusions

1 As the confining pressure increases, the cement shows more plasticity and can survive an increased number of pressure cycles. In the high-pressure wells, the cement fatigue failure probability increases as the reservoir pore pressure decreases.

2 Below 300ºF, the temperature has a minor effect on the cement low-cycle fatigue. The elastic strain and plastic strain developed by thermal stress in cement is very small compared to the strain developed by the bottomhole pressure under the low-cycle fatigue range.

3 The cement with higher Poisson's ratio and lower Young's modulus shows better low-cycle fatigue behavior. Within the requirement of compressive strength, the cement with higher plasticity is preferred for HPHT wells and steam injection wells.

4 More investigations need to be carried out to verify cement fatigue behavior at the confining pressures above 10,000 psi and temperatures above 300ºF where the temperature may affect cement low-cycle fatigue. Below 300ºF, the temperature may affect the high-cycle cement fatigue; however, more laboratory tests needed to evaluate this behavior.

CHAPTER IV

HPHT GAS WELL CEMENTING COMPLICATIONS*

4.1 Introduction

Exploring and producing new hydrocarbon reserves is, by the day, becoming a more and more challenging task, often requiring the petroleum industry to contend with hostile downhole conditions. Although HPHT wells are drilled, stimulated, produced, and monitored in a way similar to wells with less-demanding conditions, the HPHT environment limits the range of available materials and technologies to exploit these reservoirs. The oil and gas industry has been contending with elevated temperatures and pressures for many years.

Wells that present HPHT characteristics have been drilled since the late 70s in the Gulf of Mexico and the early 80s in the North Sea. The HPHT wells can be separated into three categories based on the temperature and pressure envelopes, namely HPHT, extreme HPHT, and ultra-HPHT wells, with temperatures greater than 400ºF and pressures greater than 20,000 psi (Paula et al. 2009). According to the Health and Safety Executive British safety agency, an HPHT well is one in which the nondisturbed, bottomhole temperature exceeds 300ºF and the highest pore pressure gradient foreseen for any porous formation exceeds 0.8 psi/ft, or the required working pressure for the well-control equipment needs to exceed 10,000 psi.

As the pressure increases, more gas can be stored per cubic foot in HPHT wells, which makes them very productive. These HPHT wells are much more expensive to complete because advanced technology is required. Among the increasingly deep and remote locations operators are drilling HPHT gas wells; well depth, pressure, and temperature are ever increasing. HPHT environments result in higher drilling and completion risk and cost. The increased wellbore temperature drastically affects the stability and longevity of downhole electronics and must be seriously considered in managing overall efficiency and cost. Simultaneously, because of the high-pressure operating conditions, the partial pressures of CO_2 and H_2S exposed to wellbore tubulars has increased significantly in addition to the potential for severe corrosion and cracking of the tubulars. The corrosive rates are higher for HPHT wells and require expensive corrosion-

* Reprinted with permission from "HPHT Gas Well Cementing Complications and its Effect on Casing Collapse Resistance", by Yuan Z., Schubert J., Teodoriu C. and Gardoni P., 2012, SPE 153986, Copyright © 2012, Society of Petroleum Engineers.

resistant alloys for downhole tools, wellbore construction, and surface pressure-control equipments.

Because of the high costs associated with HPHT wells, finding ways to reduce the failure probability and increase the wellbore life are high-priority items. In the completion process, cementing complications may occur although the best efforts are being used. Determining the effect of cementing complications and identifying methods to mitigate or avoid wellbore failure is highly important. Cement mechanical properties are important input data for casing-cement system analytical analysis and FEM study. Many experimental studies have been carried out to measure cement mechanical properties under different conditions. One of the earliest laboratory tests to simulate field conditions was to test cement sheath failure (Goodwin and Crook 1992). The cement was cured at a temperature of 350ºF, with a maximum inside pressure on the casing of 10,000 psi, and an annulus pressure of 500 psi. Another model with the cements cured under higher temperature was built for testing the long-term HPHT condition on the properties of cements by Stiles (2006) in which the cement was cured at the pressure of 2,133 psi with a temperature of 645ºF. The cement was cured under the conditions of 2,610 psi and 212ºF as reported by Teodoriu et al. (2012). The experimental results were used for a casing-cement-formation system analytical analysis (Atkinson et al. 1996; Teodoriu et al. 2010). Barry et al. (2009) successfully used high-density elastic cements to solve HPHT challenges in south Texas. However, the analytical analysis can only consider symmetry conditions because the casing eccentricity, cementing voids, and channeling are difficult to evaluate under these conditions.

Casing eccentricity is usually a function of the wellbore angle, the number of casing centralizers, and the wellbore dimensions. The higher the wellbore inclination angle is usually leads to a higher value of casing eccentricity (Ferda et al. 2004). The effect of casing eccentricity on a cementing operation was investigated by Courturier et al. (1990) and Silva et al. (1996). When the casing is not centered in the wellbore, the fluid favors the path of least resistance and flows more rapidly on the wide side rather than on the narrow side. These conditions result in a distorted velocity distribution and the displaced fluids may bypass the slow moving drilling mud on the narrow side. At the conclusion of the displacement process, the annulus may contain a long strip of inefficient cement displacement of the drilling mud in a given interval, depending on the local geometry. If casing eccentricity occurs, cement channeling tends to build up simultaneously, which allows cavities to be filled with drilling mud, unset cement, or formation

fluids. To prevent cement channeling, mud, spacers, and the cement properties must be designed properly as defined by Christopher et al. (1990). A number of techniques can be used to detect and repair cement channels (Hart et al. 1990).

It is also very important to know the effect casing eccentricity and cement channeling have on wellbore integrity if the cementing problems exist. FEMs are helpful in studying cementing complications resulting from complex conditions. Using FEMs, the stress distribution in the cement and the casing under perfect conditions was well analyzed (Rodriguez et al. 2003). There is a significant difference for the von Mises stress distribution in the casing between the cements having high-thermal properties with a thermal conductivity of 2.4 $/Wm^{-1}K^{-1}$ and the cements having low-thermal properties with a thermal conductivity of 0.66 $/Wm^{-1}K^{-1}$ (Manoochehr et al. 2010). The maximum von Mises stress in wellbore casing in cemented using high-thermal property cements does not increase significantly by increases the degree of casing eccentricity. However, the maximum von Mises stress in cemented wellbore casing using the low-thermal properties cements increases by increasing the casing eccentricity. In reality, most of the cements fall into the category of low-thermal property cements. The effect of casing eccentricity, voids, cement channels, and pore pressure decrease on the collapse resistance of casing was studied by Berger et al. (2004). The presence of voids and cement channels can significantly reduce the probability of casing collapse. The casing eccentricity has a minor effect on casing collapse resistance; however, the voids sizes, location, and sensitivity analysis was not considered. A study by Nabipour et al. (2010) showed the same results; i.e., the casing eccentricity has a minor effect on casing collapse resistance.

On the other hand, the sensitivity of mechanical properties to stress distribution in casing-cement-formation systems are seldom studied, and they are important parameters when attempting to improve the cement design. In the analysis being reported here, the sensitivity of casing and cement mechanical properties, voids locations, and voids sizes and shapes are taken into account and an attempt is made to which parameter is the most important and its effect on casing collapse resistance. The effects of hole angle on casing-cement-formation systems are also hardly studied. The hole angle, cement channel angle, and casing eccentricity are the variables considered in the research.

4.2 Finite Element Methods

4.2.1 Elements

FEMs are an effective tool for structural analysis and thermal analysis. The ANSYS software was the platform used to develop codes for this study. In the thermal analysis, the PLANE77 element was used, which is a higher order version of the 2D, 4-node thermal element. The element has one degree of freedom, temperature, at each node. The eight-node elements have compatible temperature shapes and are well suited to modeling curved boundaries. The eight-node thermal element is applicable to a 2D steady-state or transient thermal analysis. After the thermal analysis was performed, the results of element temperature were loaded for structural analysis. The PLANE82 element was used for structural analysis. This element is a 2D eight-node structural solid element, which provides more accurate than PLANE42 element results for mixed (quadrilateral-triangular) automatic meshes and it can tolerate irregular shapes without a significant loss of accuracy.

The elements generated are shown in Figure 33. In the first step of the thermal analysis using the PLANE77 element, the temperature of each node is calculated and stored in a file. Then the file was loaded into the structural analysis environment using the PLANE82 element and the thermal expansion and thermal stress of the casing-cement-formation system was solved. Together with the displacement boundary and pressure boundary conditions, the stress distribution in the system was calculated (shown in Figure 34 to Figure 41).

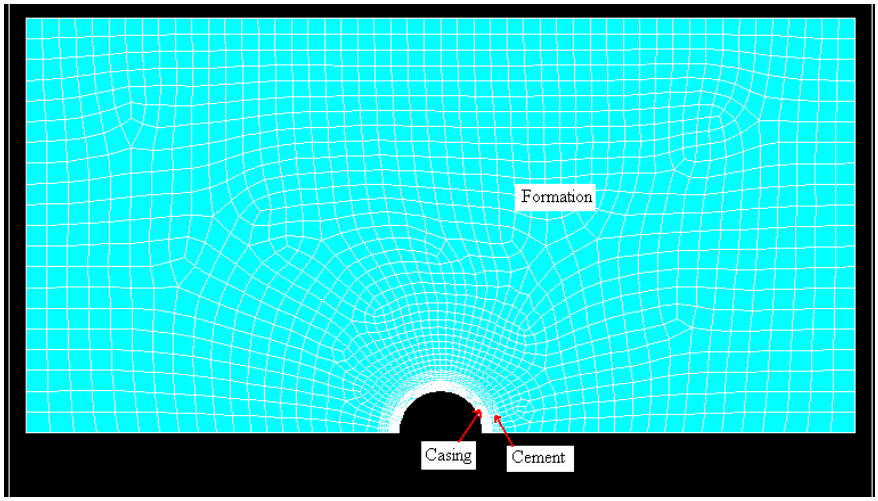

Figure 33 Casing, cement, and formation elements

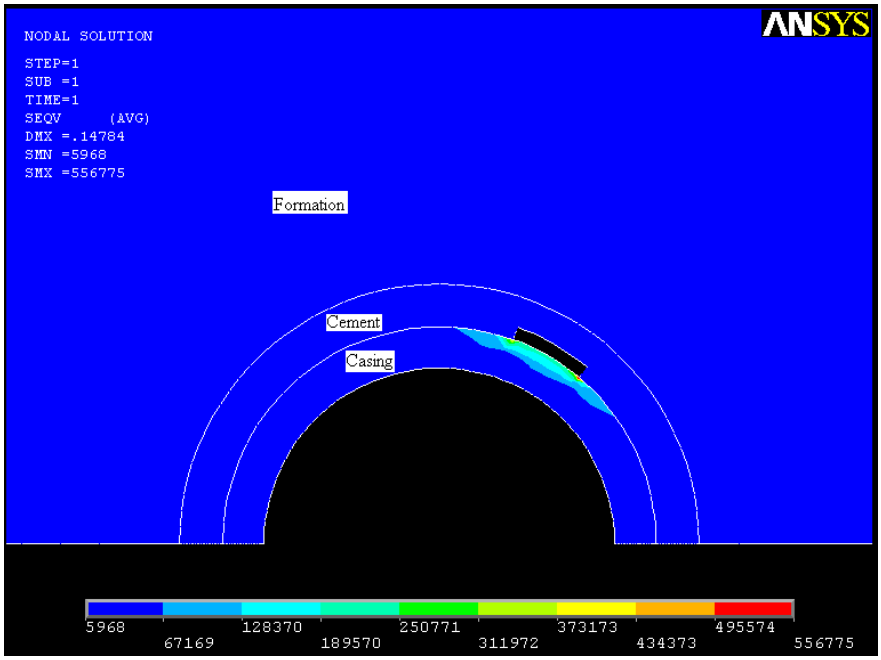

Figure 34 Casing, cement, and formation von Mises stress (voids near the casing)

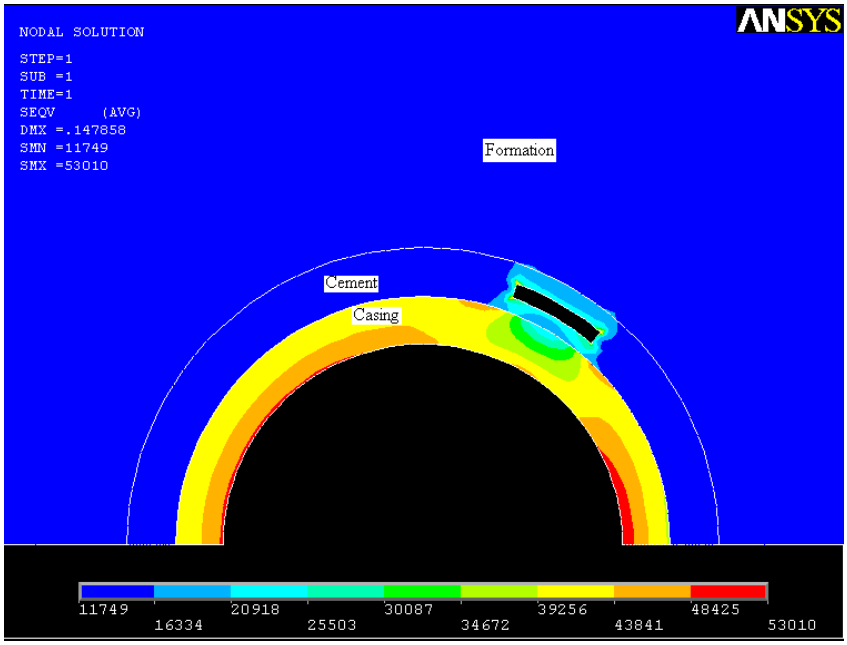

Figure 35 Casing, cement, and formation von Mises stress (voids in the center of the cement)

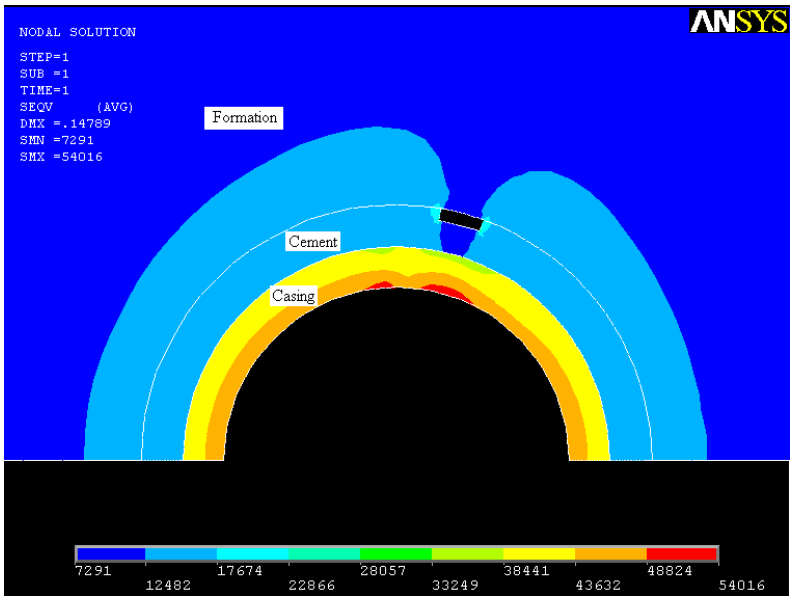

Figure 36 Casing, cement, and formation von Mises stress (voids near the formation)

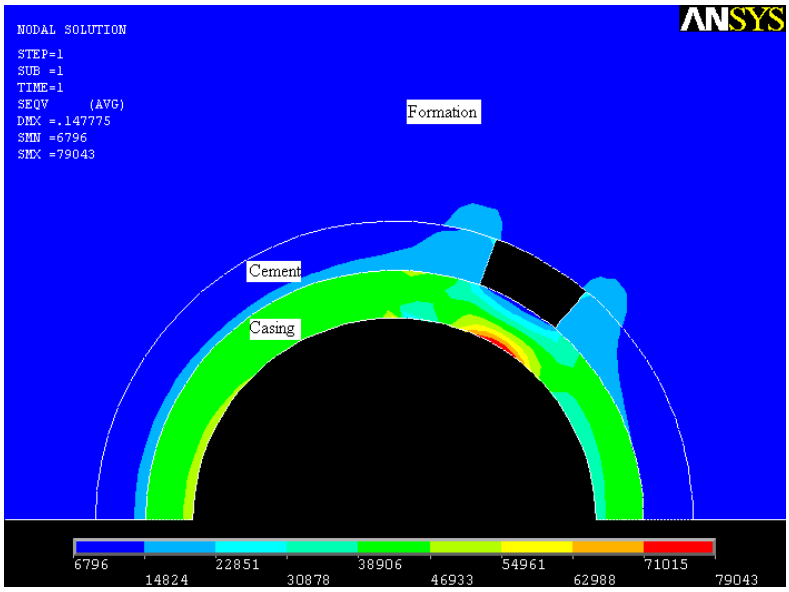

Figure 37 Casing, cement, and formation von Mises stress (cement channel)

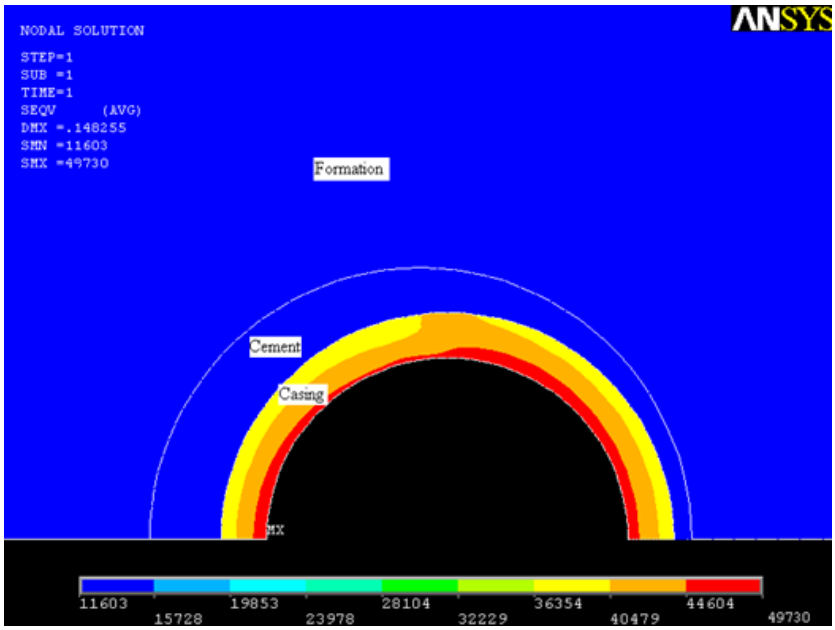

Figure 38 Casing, cement, and formation von Mises stress (0.3-in. eccentricity)

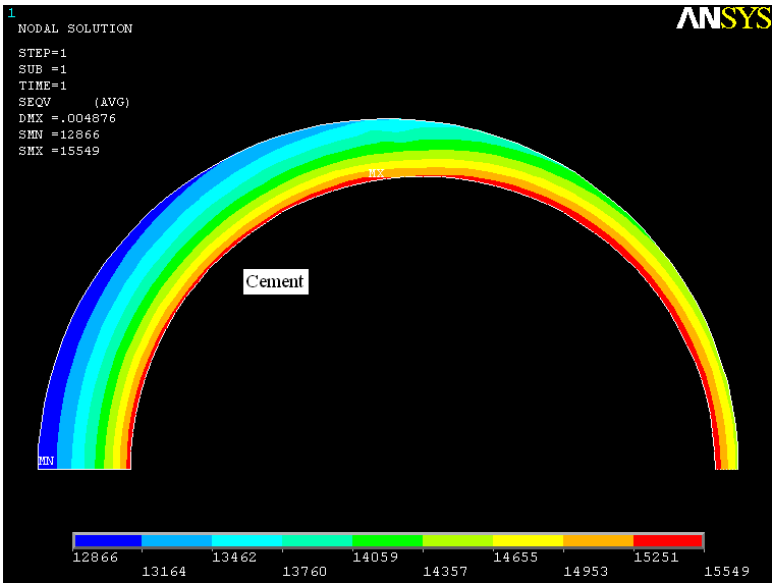

Figure 39 Cement von Mises stress (0.3-in. eccentricity)

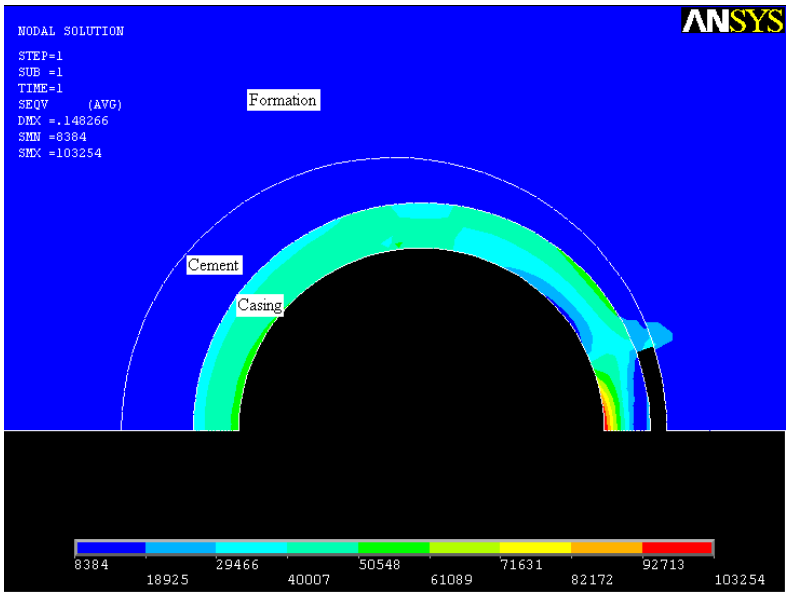

Figure 40 Casing, cement, and formation von Mises stress (0.3-in. eccentricity and channel)

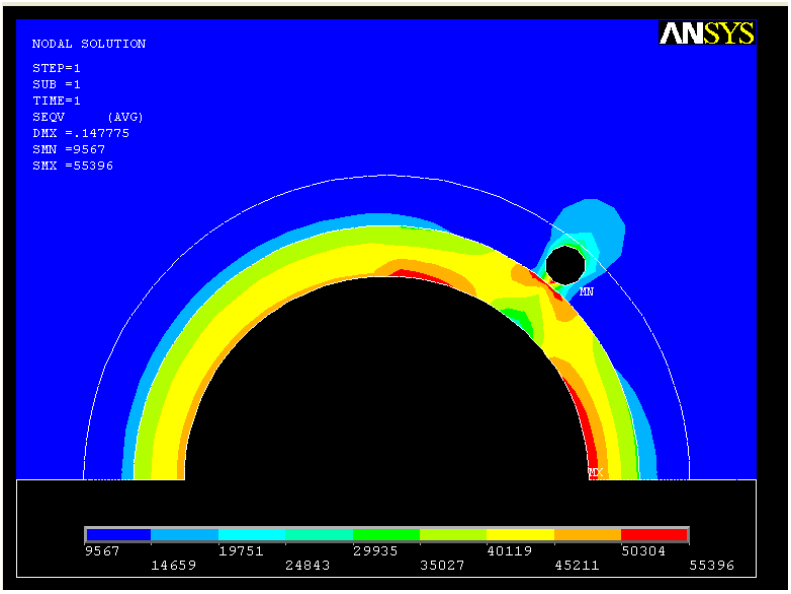

Figure 41 Casing, cement, and formation von Mises stress (circular void)

4.2.2 Model Dimensions and Boundary Conditions

The wellbore conditions used in this study are from a typical HPHT gas well in south Texas that produces from a sand formation. The boundary conditions are shown in Table 6. The well depth is 18,000 ft with a pore-pressure gradient of 0.9 psi/ft. The well completion consisted of 23.2 lb/ft, 5-in. OD, Grade P110 casing in a 6-in. borehole. In the simulation, two cement systems from Table 7 are used, an elastic cement and a brittle cement system, to study the effect of cement mechanical properties on casing collapse resistance.

Table 6 2D model dimension and boundary conditions

Casing ID. (in.)	4.044
Casing OD. (in.)	5
Hole Diameter (in.)	6
Formation Radius (in.)	20
Maximum Horizontal Stress (psi)	11,950
Minimum Horizontal Stress (psi)	11,820
Pore Pressure (psi)	11,000
Bottomhole Pressure (psi)	10,000
Reservoir Temperature (ºF)	300
Bottomhole Temperature (ºF)	260

Table 7 Material mechanical properties

	Casing	Elastic Cement	Brittle Cement	Formation
Young's Modulus (psi)	3E7	2E6	4E6	3E6
Poisson's Ratio	0.3	0.35	0.2	0.3
Specific Heat (Btu/lb.ºF)	0.11943	0.5231	0.5008	0.2385
Coefficient of Thermal Expansion (/ºF)	1.3E–5	9E–6	1e–5	1E–5
Thermal Conductivity (Btu/hr ft ºF)	8.668	0.5425	0.6149	0.5726

4.3 Sensitivity Analysis

Probabilistic sensitivities are important to improve the design toward a more reliable and better quality product, or to save money while maintaining the reliability or quality of the product. A sensitivity plot for any random output parameter in the model can be made to show the sensitivities of the random input variables on the random output random variables.

Usually, researchers use log-normal distribution to describe material mechanical properties because for log-normal distributions, the material mechanical property values are positive. However, according to the characteristics of a log-normal distribution, there is a small probability that the values for the log-normal distribution reach positive infinite values or nearly zero. In reality, the values of material mechanical properties cannot reach positive infinity or approach zero. A beta distribution can describe the material property better than log-normal distribution with the lower boundary and upper boundary limits. A beta distribution of a random variable X has four distribution parameters, namely the shape parameters *r* and *t*, the lower limit *a*, and the upper limit *b*. The probability density function of a beta distribution is shown in (4.1).

$$Bet(a,b,q,r) = \frac{(x-a)^{q-1}(b-x)^{r-1}}{B(q,r)(b-a)^{q+r+1}}, \tag{4.1}$$

with the parameters range being $a < b$, $0 < q$, $0 < r$, $a \le x \le b$

in which the beta function is given by (4.2)

$$B(q,r) = \frac{\Gamma(q)\Gamma(r)}{\Gamma(q+r)} \tag{4.2}$$

and the gamma function is given by (4.3)

$$\Gamma(k) = \int_0^\infty u^{k-1}\exp(-u)\,du \tag{4.3}$$

Inherently, Monte Carlo simulations always vary all random input variables at the same time; thus, if interactions exist, then they will always be correctly reflected in the probabilistic sensitivities. The Monte Carlo simulations method is used for the sensitivity analysis with 1,000 repetitions, which means every random input variable has 1,000 sample points as shown in the wellbore diameter distribution (Figure 42).

Table 8 Random input variables and distribution

	Distribution Type	a (Minimum value)	B (Maximum value)	q (Shape Factor)	r (Shape Factor)
Casing Inside Pressure (psi)	Beta distribution	2000	14000	2	3
Wellbore Diameter (in.)	Beta distribution	5.8	7.5	2	5
Casing Young's Modulus (psi)	Beta distribution	2.5e7	3.5e7	2	2
Casing Poisson's Ratio	Beta distribution	0.25	0.35	2	2
Cement Young's Modulus (psi)	Beta distribution	1e6	5e6	2	3
Cement Poisson's Ratio	Beta distribution	0.15	0.4	2	3
Formation Young's Modulus (psi)	Beta distribution	1e6	3e6	2	2
Formation Poisson's Ratio	Beta distribution	0.15	0.35	2	2

Usually, the cement sheath fails before the casing fails because the cement sheath cannot provide sufficient support for the casing. Thus, in the sensitivity analysis, the cement stress distribution is more important than the casing stress distribution. Also, the cement maximum von Mises stress and maximum shear stress are used as random output variables. The input random variables are shown in Table 8.

The evaluation of the probabilistic sensitivities is based on the correlation coefficients between all random input variables and a particular random output parameter. To plot the sensitivities of a certain random output parameter, the random input variables are separated into two groups: those that are significant (important) and those that are insignificant (not important) for the random output parameter. The sensitivity plots will only include the significant random input variables. The probabilistic design system will plot only the sensitivities of the random input variables that

are found to be significant; however, insignificant sensitivities are printed in the output window. In the sensitivity plot, a positive sensitivity indicates that increasing the value of the random input variable increases the value of the random output parameter for which the sensitivities are plotted. Likewise, a negative sensitivity indicates that increasing the random input variable value reduces the random output parameter value.

Figure 43 and Figure 44 show that the cement maximum von Mises stress and the cement maximum shear stress are sensitive to the cement Young's modulus and the formation Young's modulus. The casing inside pressure, wellbore diameter, casing Young's modulus, casing Poisson's ratio, cement Poisson's ratio, and formation Poisson's ratio are insignificant parameters in the sensitivity analysis. In reality, the formation Young's modulus is an uncontrollable parameter; only the cement Young's modulus can be designed and controlled. Reducing the value of the cement Young's modulus can reduce the cement maximum von Mises stress and provide a better cement sheath support for the casing. On the other hand, reducing the value of the cement Young's modulus will increase the cement maximum shear stress, which may lead to poor cement sheath support. The balance has to be weighed between the advantage and disadvantage of reducing the cement Young's Modulus. Within the limit of cement shear failure, the value of the cement Young's modulus can be designed to a minimum if economically available.

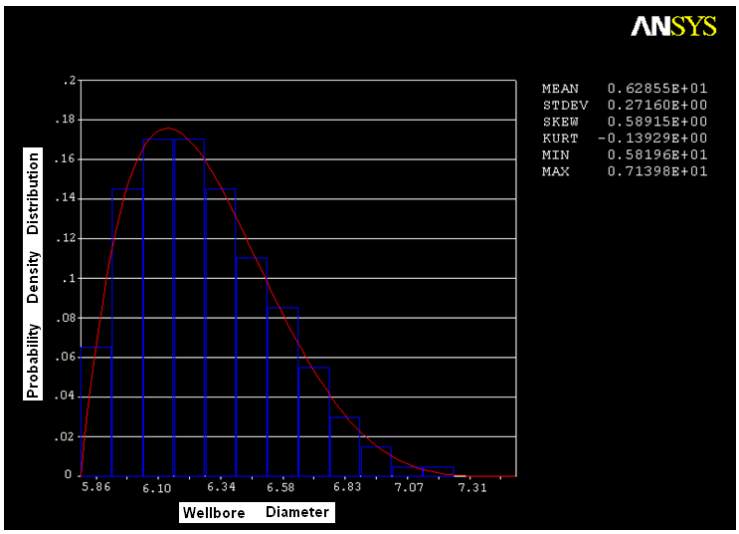

Figure 42 Wellbore diameter distribution

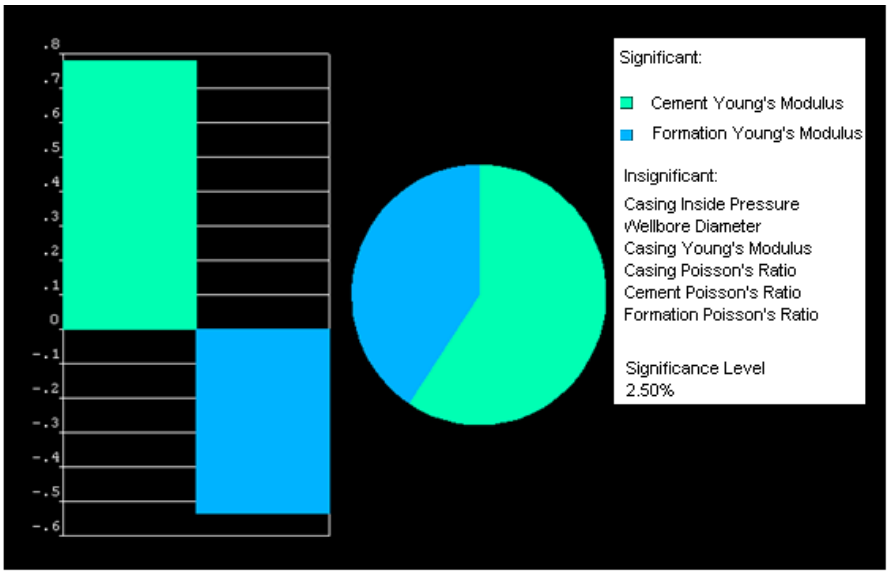

Figure 43 Cement maximum von Mises stress sensitivity analysis

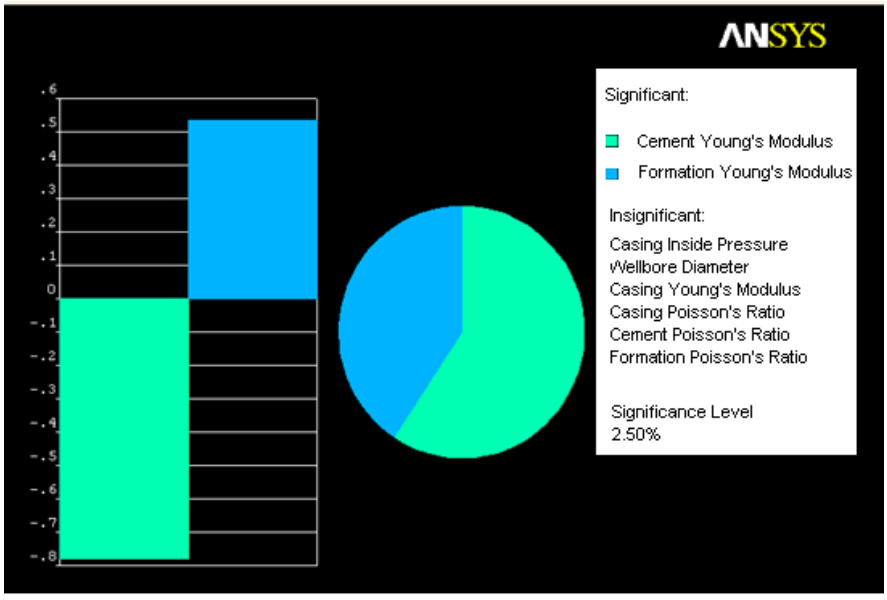

Figure 44 Cement maximum shear stress sensitivity analysis

4.4 Cementing Complications Analysis

In the simulation, seven cases were studied (Figure 34 to Figure 41). Casing centered in the borehole without any cementing complications is the perfect case. In the cementing complication analysis, casing eccentricity, void, and cement channel were considered. In the cementing void analysis, the effect of the void location on the wellbore integrity was studied. Finally, casing eccentricity and cement channel were studied together in the last case.

In the analysis, the 0.3-in. eccentricity implies that the center of the casing moves 0.3 in. toward the wellbore. From Table 10 and Figure 45, the casing eccentricity alone does not have much effect on the casing and cement. The maximum von Mises stress difference is only 0.27% for the 0.3-in. eccentricity with the casing centered in the borehole. The void location has the most effect on casing stress. If the voids are located near the casing, the maximum von Mises stress in the casing increases significantly compared to the other cases. The von Mises stress in the contact area between the casing and the voids is frequently beyond the casing yield strength. Water or drilling mud trapped in the voids has very lower compressibility and they behave like incompressible material compared to casing and cement. This condition may cause very high stress in the contact area between the voids and the casing.

Casing eccentricity and cement channel usually occur simultaneously. This condition is the second highest failure-probability scenario. If casing is not centered, the cross-sectional area fluid flow velocity is different during the cementing process. This condition may contribute to the cement channel problem in the lower clearance area. Cement channels lead to the third highest von Mises stress in the casing. The stress in this scenario is 60% greater than the stress under perfect conditions. Casing eccentricity, voids in the center of cement, and voids near the formation does not have much effect on the casing von Mises stress when compared to the perfect conditions.

There is slightly less von Mises stress developed in the casing under the condition of elastic cement. However, using the elastic cement does not improve the stress distribution in the casing significantly. The stress in the casing under the condition of elastic cement is 12% less than the stress in the casing under the condition of brittle cement.

For the stress developed in the cement, based on Table 9, Figure 45, and Figure 46, voids in the center of the cement, voids near casing, and 0.3-in. eccentricity and cement channel are the three worst case scenarios. For brittle cement, voids near the formation and cement channel also

develop very high stresses in the cement. Cement channel and cement voids near the formation increase the von Mises stress in the cement significantly compared to the perfect cement condition. It is obvious that the elastic cement has much better behavior than brittle cement. The stresses in the three worst cases are reduced by 33% to 43%. This trend is also seen in the scenario of voids near the formation and the cement channel

Table 9 Casing and cement maximum von Mises stress distribution

	Brittle Cement		Elastic Cement	
	Casing von Mises Stress (psi)	Cement von Mises Stress (psi)	Casing von Mises Stress (psi)	Cement von Mises Stress (psi)
Casing Centered in the Hole	49,598	15,418	46,246	14,658
0.3-in. Eccentricity	49,730	15,949	46, 697	14,832
Voids Near Casing	189,570	49,010	178,266	27,912
Voids in the Center of Cement	53,010	47,234	46,770	28,878
Voids near Formation	54,016	26,719	51,767	15,477
Cement Channel	79,043	30,134	62,276	17,792
0.3-in. Eccentricity and Cement Channel	103,254	45,975	91,864	30,625

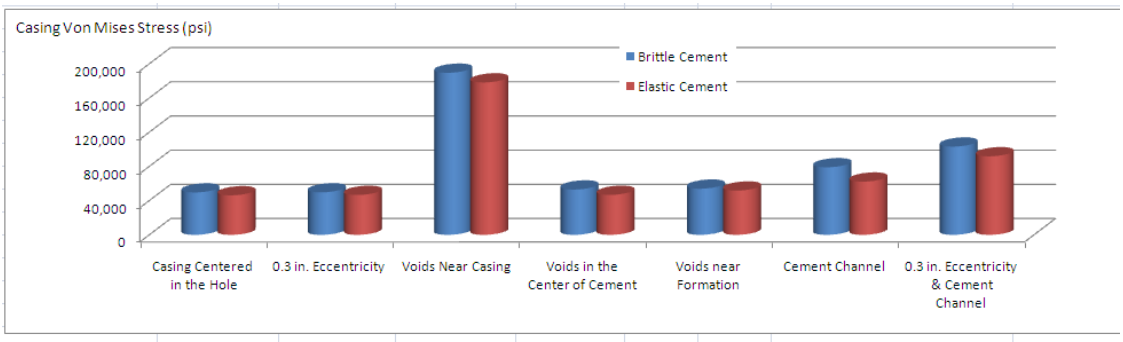

Figure 45 Casing maximum von Mises stress

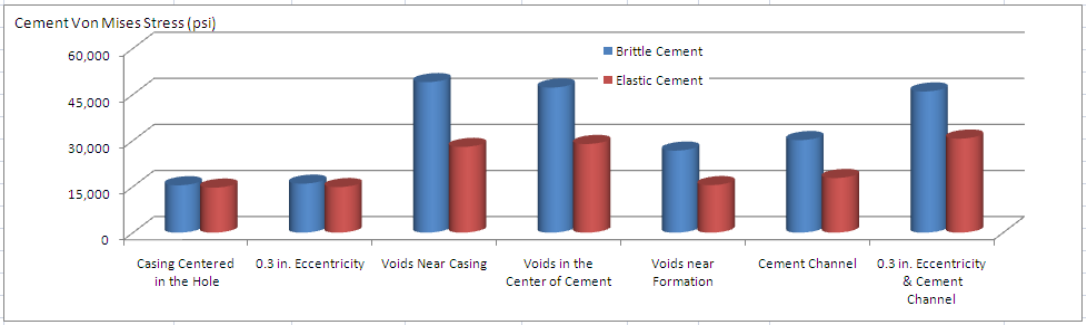

Figure 46 Cement maximum von Mises stress

4.5 Voids Shape and Size Effect

In the 2D simulation, rectangular and circular void shapes are used in the analysis. For the circular voids, the radius was increased from 0.1 in. to 0.2 in. As shown in Table 10 and Figure 47, the voids shape and size does not have much effect on the maximum von Mises stress developed in the casing.

However, from Figure 48, the maximum von Mises stress developed in the cement with 0.2-in. radius circular void is 27% greater than that in cement with a 0.1-in. radius circular void. For brittle cement, the cement with the rectangular void and the 0.2-in. radius circular void has the highest von Mises stress and is more sensitive to the void shape. For the elastic cement, the void shape has minor effects on the cement stress distribution. As the void size increases, the maximum stresses developed in the cement also increase. Irrespective of the voids location, their size, and their shape, the elastic cement shows much better behavior than the brittle cement.

Table 10 Casing and cement maximum von Mises stress distribution for different voids

	Brittle Cement		Elastic Cement	
	Casing von Mises Stress (psi)	Cement von Mises Stress (psi)	Casing von Mises Stress (psi)	Cement von Mises Stress (psi)
Casing Centered in the Borehole	49,598	15,418	46,246	14,658
Rectangular Void in the Cement Center	53,010	47,234	46,770	28,878

Table 10 Continued

	Brittle Cement		Elastic Cement	
	Casing von Mises Stress (psi)	Cement von Mises Stress (psi)	Casing von Mises Stress (psi)	Cement von Mises Stress (psi)
Circle Void in the Cement Center (0.1-in. radius)	50,559	39,592	49,314	34,542
Circle Void in the Cement Center (0.15-in radius)	53,035	44,455	51,685	39,899
Circle Void in the Cement Center (0.2-in. radius)	56,925	48,378	55,414	43,872

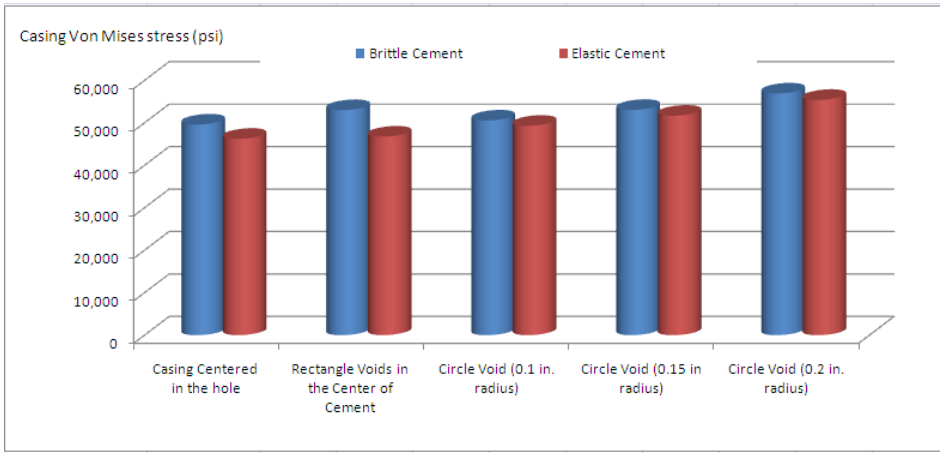

Figure 47 Casing maximum von Mises stress

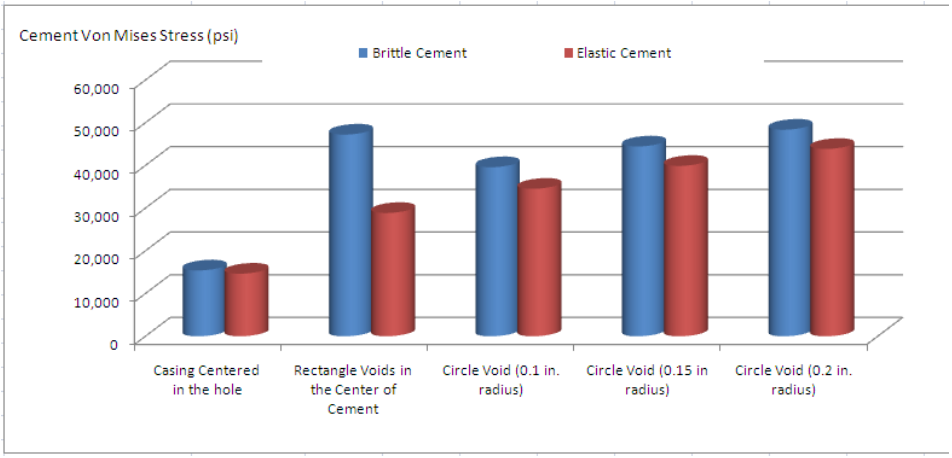

Figure 48 Cement maximum von Mises stress

4.6 Conclusions

1. The cement maximum von Mises stress and the cement maximum shear stress are sensitive to the cement Young's modulus and the formation Young's modulus. Reducing the value of the cement Young's modulus can reduce the cement maximum von Mises stress and increase the cement maximum shear stress. Within the limit of cement shear failure, the value of the cement Young's modulus can be designed to minimum if economically feasible.

2. The casing eccentricity alone does not have much effect on the stress developed in the casing and cement. The maximum von Mises stress difference is only 0.27% for the 0.3-in. eccentricity and the casing centered in the borehole.

3. For the stresses developed in the cement, voids in the center of the cement, voids near the casing, and 0.3-in. eccentricity and cement channel are the three worst-case scenarios. For the stresses developed in the casing, voids near the casing, and casing eccentricity and cement channel are the worst two cases.

4. The elastic cement behaves much better than brittle cement than the stress developed in the casing and cement. The stress in the casing under the condition of elastic cement is 12% less than stress in the casing under the condition of brittle cement. The stresses developed in the cement in the three worst cases (voids in the center of the cement, voids near the casing, and 0.3-in. eccentricity and cement channel) are reduced by 33% to 43%.

5. The voids shape and size do not have much effect on the maximum von Mises stress developed in the casing. The brittle cement is more sensitive to the void shape than the elastic cement for the stress developed in the cement.

CHAPTER V

CEMENT FAILURE PROBABILITY UNDER HPHT CONDITIONS*

5.1 Introduction

A quality cement sheath provides: (1) support for the casing; (2) zonal isolation; (3) corrosive protection for the casing. It is important to have a quality cement sheath to maintain wellbore integrity. The three types of cements (72-lbm/ft^3, 101-lbm/ft^3, and 118-lbm/ft^3) are successfully used in the Haradh field located in the southern part of the Ghawar oilfield in the eastern province of Saudi Arabia (see Figure 49).

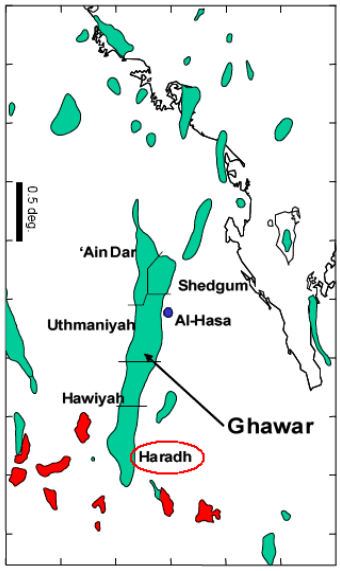

Figure 49 Location of the Haradh oilfield (Stenger et al. 2002)

The 72-lbm/ft^3 light-weight cement was used to control lost circulation and eliminate the stage collar for multistage cementing during the cement operation. The light-weight cement was

* Reprinted with permission from "Cement Failure Probability under HPHT Conditions Supported By Long Term Laboratory Studies and Field Cases", by Yuan Z., Abdullah A., Schubert J. and Teodoriu C., 2012, SPE 154746, Copyright © 2012, Society of Petroleum Engineers.

successfully used worldwide. Due to the lost circulation and formation low-fracture gradient, light-weight cement is required to reduce the hydrostatic pressure of the fluid column while pumping the cement slurry. The concept of particle packing was introduced to the petroleum industry to obtain light-weight, high-performance cements (Eric et al. 1997; Bernard et al. 2002). Because of the poor performance of multistage cements, the stage collar was thought to be the weak point in the casing string. The well service life can be increased by using high-performance, light-weight cement and eliminating the stage collar for multistage cementing (Talal et al. 1999). Later, the light-weight cement was successfully applied in the San Juan Basin of New Mexico (Ross et al. 2001). At the same time, to overcome lost circulation, an ultra-light-weight cement system with a density close to that of water was used to ensure good casing protection and zonal isolation in United Arab Emirates fields (Christian et al. 2001). Under HPHT cement-curing conditions, the cement mechanical property development is sensitive to temperature rather than pressure. At high-temperatures, it is observed that there is a general coarsening of the nanometer-scale structure of the hardened cement paste over time, with associated degradation of the properties (Jeffrey et al. 2012). In our study, the three cement systems were cured at 300ºF for a period of 1, 7, 30, 60, 90, 180, 270, and 360 days. The cement mechanical properties are shown in Table 11.

Table 11 Cement mechanical properties

Time (Days)	72 lbm/ft^3 Cement		101 lbm/ft^3 Cement		118 lbm/ft^3 Cement	
	Young's modulus (psi)	Poisson's ratio	Young's modulus (psi)	Poisson's ratio	Young's modulus (psi)	Poisson's ratio
1	4.55E+05	0.120	3.42E+05	0.124	2.33E+06	0.263
7	7.40E+05	0.167				
30	4.09E+05	0.102	6.47E+05	0.145	2.61E+06	0.213
60	7.28E+05	0.135			2.32E+06	0.219
90	1.97E+05	0.147	4.19E+05	0.126	2.45E+06	0.200
180	5.13E+05	0.454	8.70E+04	0.189	4.99E+05	0.176
270	1.05E+05	0.046	3.88E+05	0.100		
360	1.62E+05	0.068				

The 72-lbm/ft^3 cement was only applied in vertical wells until now. The 101-lbm/ft^3 cement and the 118-lbm/ft^3 cement were used in vertical and deviated wells. This paper evaluates the cement long-term mechanical property and the wellbore stability issues in deviated wells.

5.2 Cement Failure Modes

Cement failure risk was calculated based on a performance function of the type:

$$g(X) = R(X) - S(X) \tag{5.1}$$

where *R(X)* is a random function describing the resistance or strength of the component or constituent; *S(X)* is the response of the structure, also a random variable; and *X* is the vector of random variables. A negative or zero *g(x)* represents a failure event. The probability of failure, p_f, is defined as follows:

$$p_f = p\left(g(X) \le 0\right) \tag{5.2}$$

The cement's usual failure modes are compressive failure, shear failure, tensile failure, and yield failure. Cement yield failure occurs under high-confining pressure, which is the minimum horizontal stress in the particular reservoir conditions. The cement and rock compressive strength increases significantly under confining pressure. The relationship between the confining pressure and compressive strengths can be expressed as follows:

$$\sigma = \frac{2S_0 \cos\phi}{1-\sin\phi} + \frac{1+\sin\phi}{1-\sin\phi}\sigma_3 \tag{5.3}$$

The cement compressive failure, shear failure, tensile failure, and yield failure are expressed in Equations (5.4), (5.5), (5.6), and (5.8).

1. Compressive failure

$$g_1(\sigma, \sigma_s) = -\sigma + \sigma_s \tag{5.4}$$

2. Shear failure (Jaeger 1969)

$$g_2(S_0, \mu, \sigma_1, \sigma_3) = S_0 - \frac{1}{2}\sigma_1\left[\left(\nu^2+1\right)^{\frac{1}{2}} - \nu\right] + \frac{1}{2}\sigma_3\left[\left(\nu^2+1\right)^{\frac{1}{2}} + \nu\right] \tag{5.5}$$

3. Tensile failure

$$g_3\left(\sigma_{tensile},\sigma_t\right)=-\sigma_{tensile}+\sigma_t \tag{5.6}$$

4. Yield Failure

$$\sigma_{eqv}=\sqrt{\frac{\left(\sigma_1-\sigma_2\right)^2+\left(\sigma_1-\sigma_3\right)^2+\left(\sigma_2-\sigma_3\right)^2}{2}} \tag{5.7}$$

$$g_4(\sigma_y,\sigma_{eqv})=-\sigma_{eqv}+\sigma_y \tag{5.8}$$

5.3 FEM Analysis

The stress and strain developed in the casing, cement, and formations are evaluated using FEM analysis. The 3D models were built from the borehole angle of 0 to 90º. ANSYS was the platform used to develop code for the FEM analysis. The types of elements used include SHELL63, SHELL93, SOLID45, and SOLID95. SOLID45 is used for the 3D modeling of solid structures. This element is defined by eight nodes having three degrees of freedom at each node. SOLID95, a higher order version of the 3D 8-node solid element SOLID45, can tolerate irregular shapes without as much loss of accuracy. The element, defined by 20 nodes having three degrees of freedom per node, may have any spatial orientation. Both the SOLID45 and SOLID95 elements have the capabilities of plasticity, creep, stress stiffening, large deflection, and large strain. Because of the higher accuracy, more time is required for element SOLID95 to complete the solution than element SOLID45.

In the meshing process, the first step is to mesh the top surface area by SHELL63 and SHELL93 elements. The VSWEP command was then used to mesh the volumes. The formation top surface area was meshed by the SHELL63 element, and then the SOLID45 element was used for the volume sweep made from the top surface to the bottom. The SHELL93 element was used for meshing the casing and the cement top surface area, and then elements of SOLID95 were used for the volume sweep made from the top surface to the bottom. The benefit achieved by using the SHELL93 element is to keep the middle node for the SOLID95 element. For the case of using the SHELL63 to mesh area and using SOLID95 to perform the volume sweep, the meshed element is still SOLID45 because the middle node in the element cannot be kept. Finally, the meshed casing and cement elements are SOLID95, and the meshed formation elements are SOLID45.

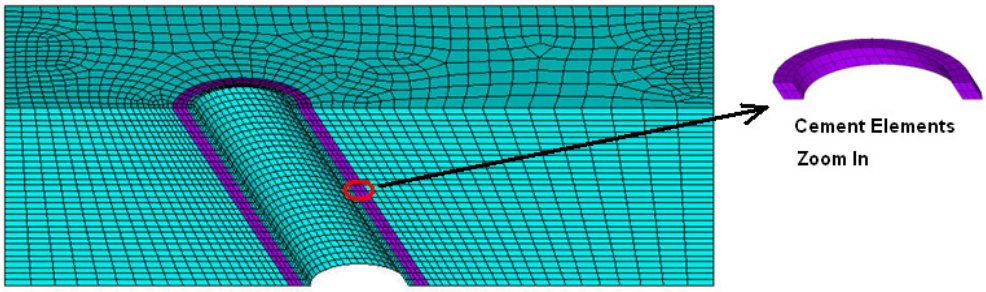

Figure 50 Casing, cement, and formation system elements

To reduce the boundary effect for different wellbore angles, the results from the middle element located in the half height are used to study the cement stress and strain (see Figure 50). In the analysis, the casing was 58.4-lbm/ft, NKHC-110 grade with a 9 5/8-in. OD, and the wellbore diameter was 12 in. The formation Young's modulus was 4E6 psi and the Poisson's ratio was 0.25. The measured depth of the wellbore was 18,117 ft with the true vertical depth of 11,562 ft, and the wellbore angle was 90º. The minimum effective horizontal stress, the maximum effective horizontal stress, and the effective vertical stress were 2,999 psi, 7,938 psi and 3,616.5 psi respectively.

5.4 Results Analysis

The cement maximum shear stress occurs at the interface between the cement and the formation. When a fracture takes place, failure occurs due to shear stress along the surface inclined at about 30º to the direction of the maximum principal pressure. The steady-state friction varies exponentially with contact pressure (William 1965). With high-confining pressure, the cement shear strength can increase exponentially. The transition from brittle to ductile failure occurs when the friction along the fracture surfaces exceeds the shear strength of the rock. For 72-lbm/ft^3 cement, Figure 51 shows that the highest shear stress occurs at a borehole angle between 40 and 50º at the time of 7 and 60 days. The shear stress is reduced from 8,000 psi at the beginning to 4,000 psi at 270 days and then remains stable at approximately 4,000 psi.

It is believed that the ultimate compressive strength of oilwell cements is nearly a linear function of effective confining pressure (John 1968). At an effective confining pressure of 15,000 psi, cement strengths are in the range of 30,000 to 50,000 psi. Figure 52 to Figure 54 show the same trend for cement maximum radial stress, maximum tensile stress, and maximum equivalent stress

as that shown in Figure 51. The cement stress at 270 days is less than the stress at the beginning and then remains constant.

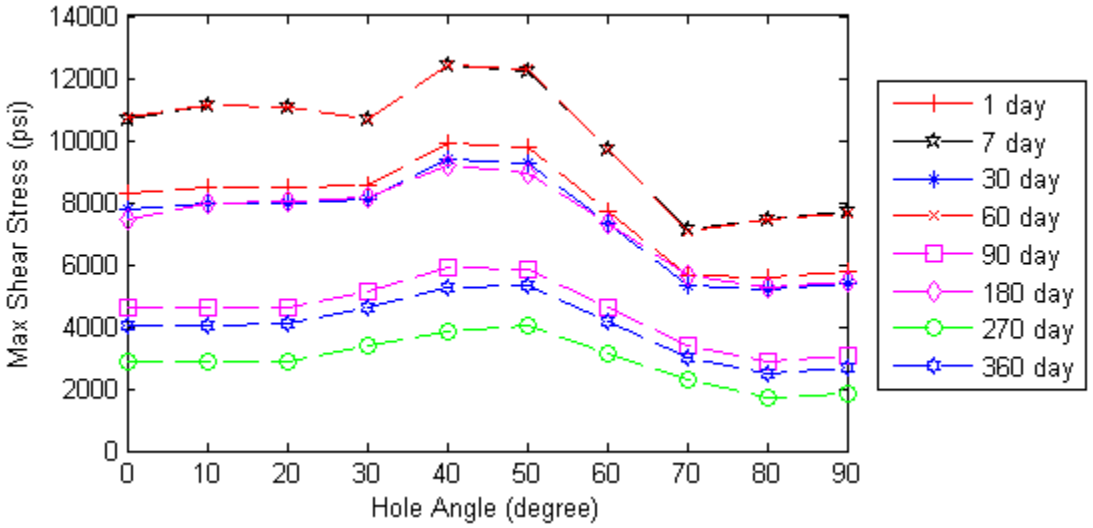

Figure 51 Cement maximum shear stress as a function of wellbore angle (pore pressure = 5,168 psi; 72-lbm/ft^3 cement)

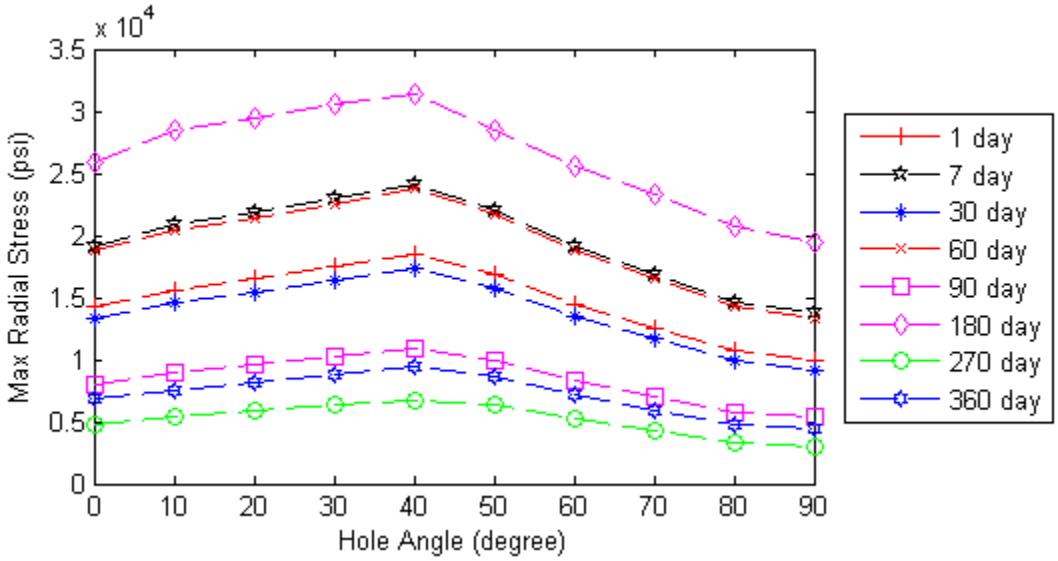

Figure 52 Cement maximum radial stress as a function of wellbore angle (pore pressure = 5,168 psi; 72-lbm/ft^3 cement)

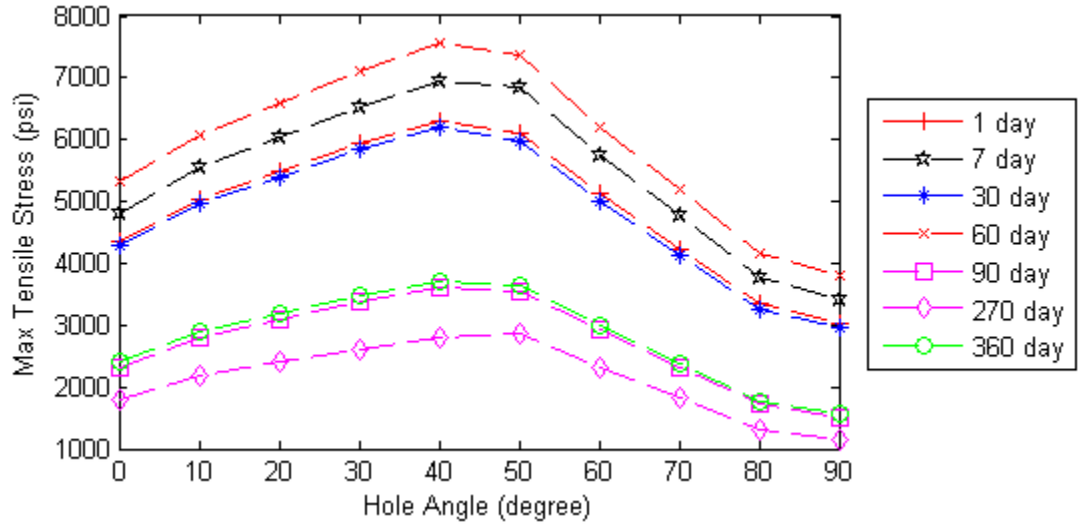

Figure 53 Cement maximum tensile stress as a function of wellbore angle (pore pressure = 5,168 psi; 72-lbm/ft^3 cement)

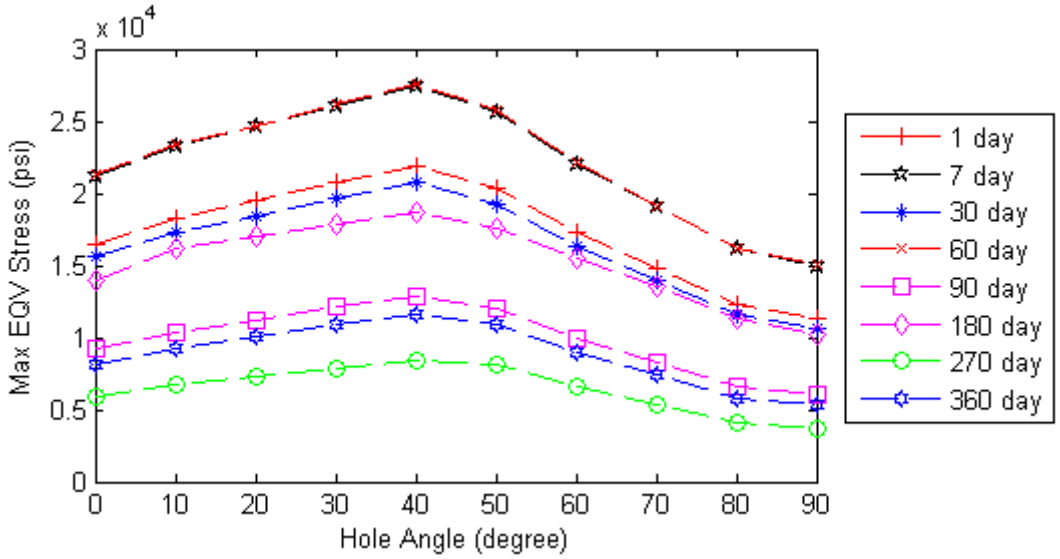

Figure 54 Cement maximum equivalent stress as a function of wellbore angle (pore pressure = 5,168 psi; 72-lbm/ft^3 cement)

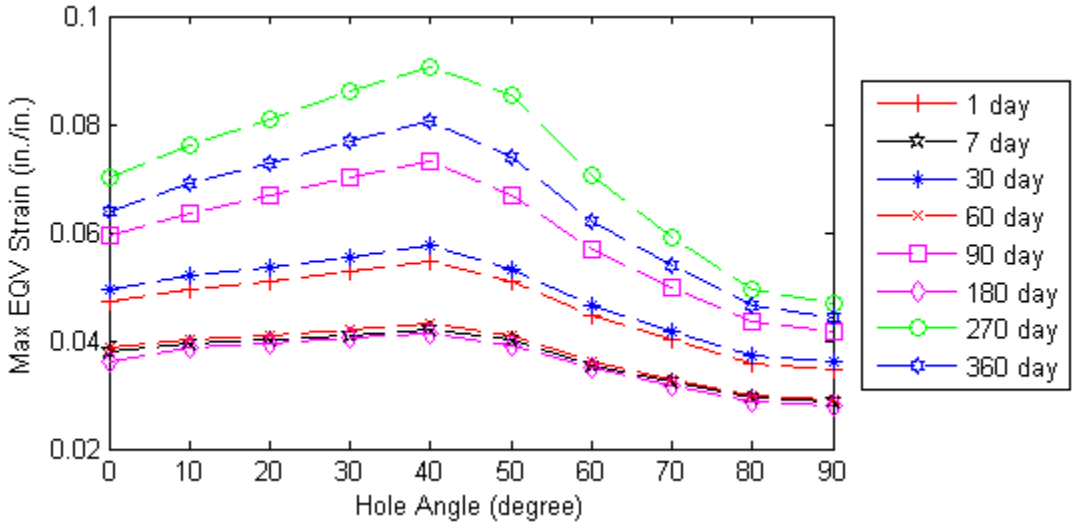

Figure 55 Cement maximum equivalent strain as a function of wellbore angle (pore pressure = 5,168 psi; 72-lbm/ft^3 cement)

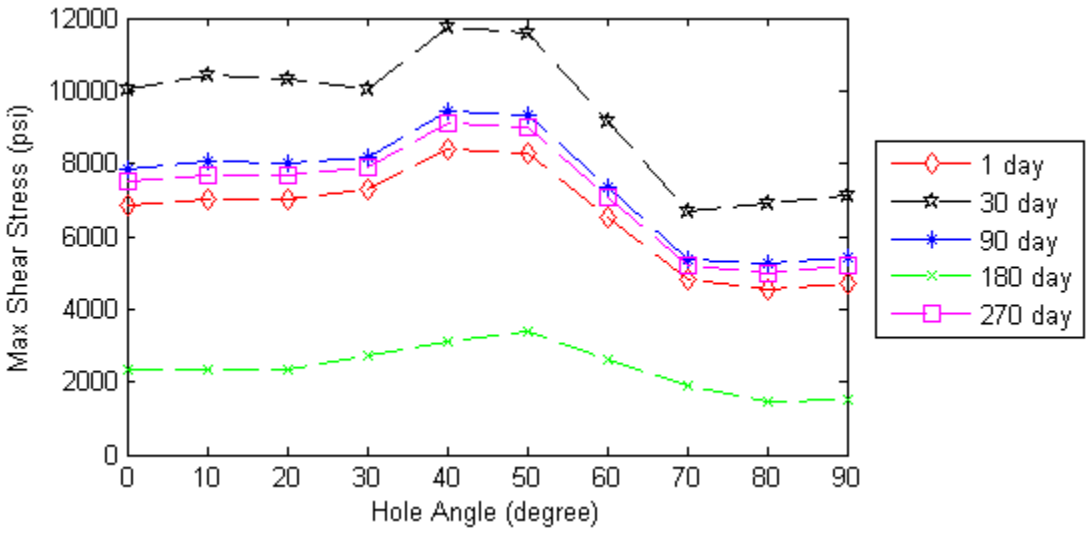

Figure 56 Cement maximum shear stress as a function of wellbore angle (pore pressure = 5,168 psi; 101-lbm/ft^3 cement)

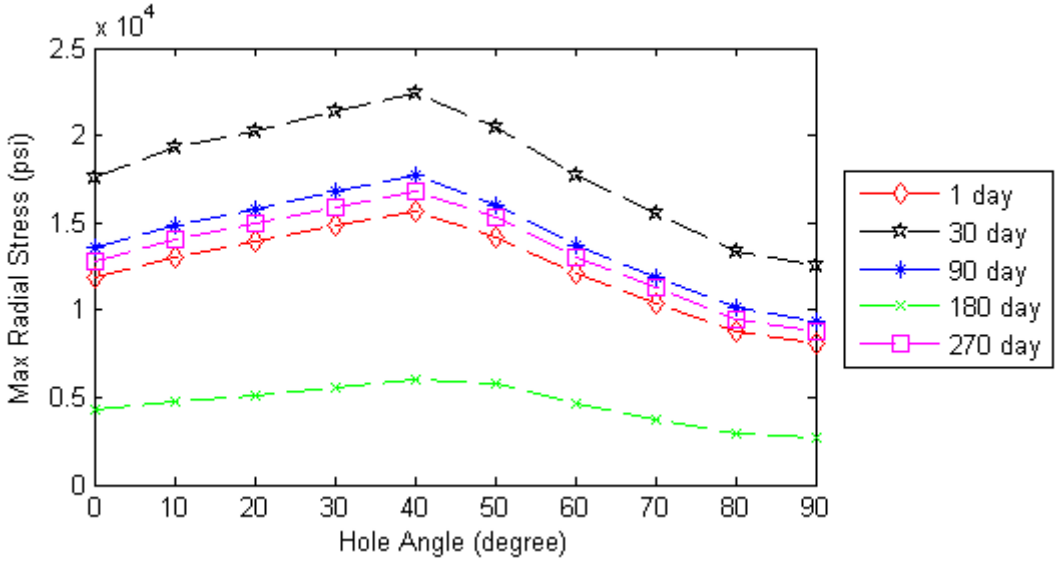

Figure 57 Cement maximum radial stress as a function of wellbore angle

(pore pressure = 5,168 psi; 101-lbm/ft^3 cement)

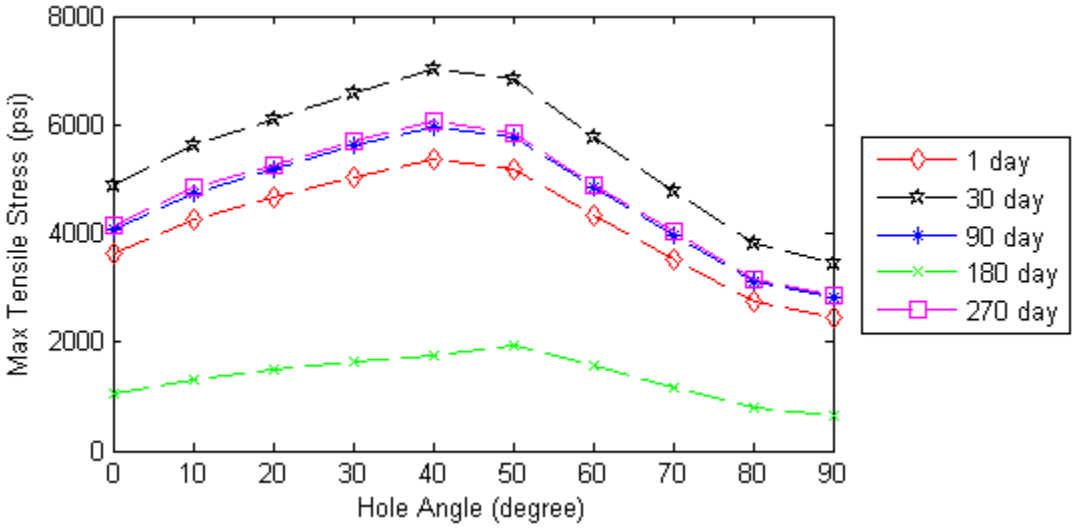

Figure 58 Cement maximum tensile stress as a function of wellbore angle

(pore pressure = 5,168 psi; 101-lbm/ft^3 cement)

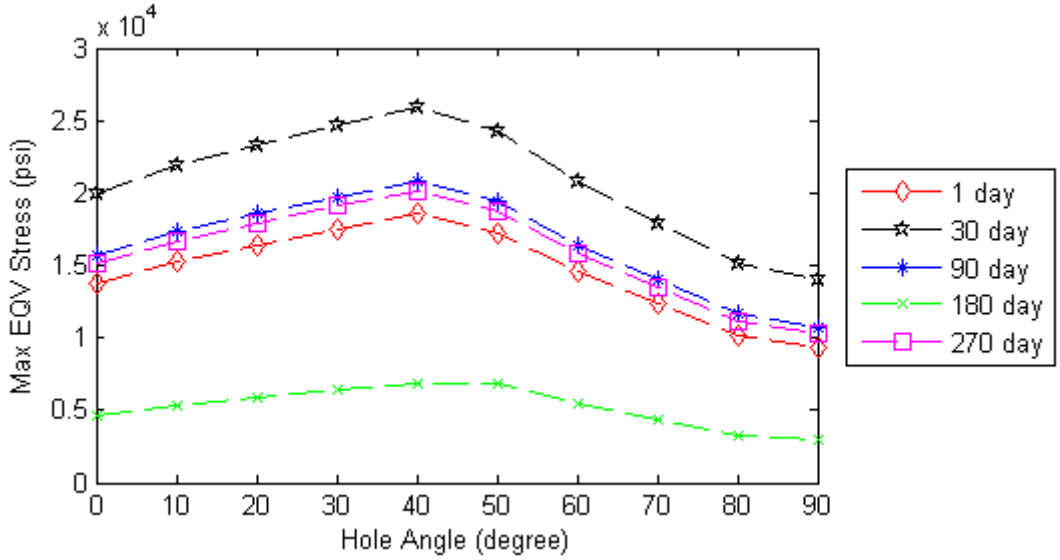

Figure 59 Cement maximum equivalent stress as a function of wellbore angle (pore pressure = 5,168 psi; 101-lbm/ft^3 cement)

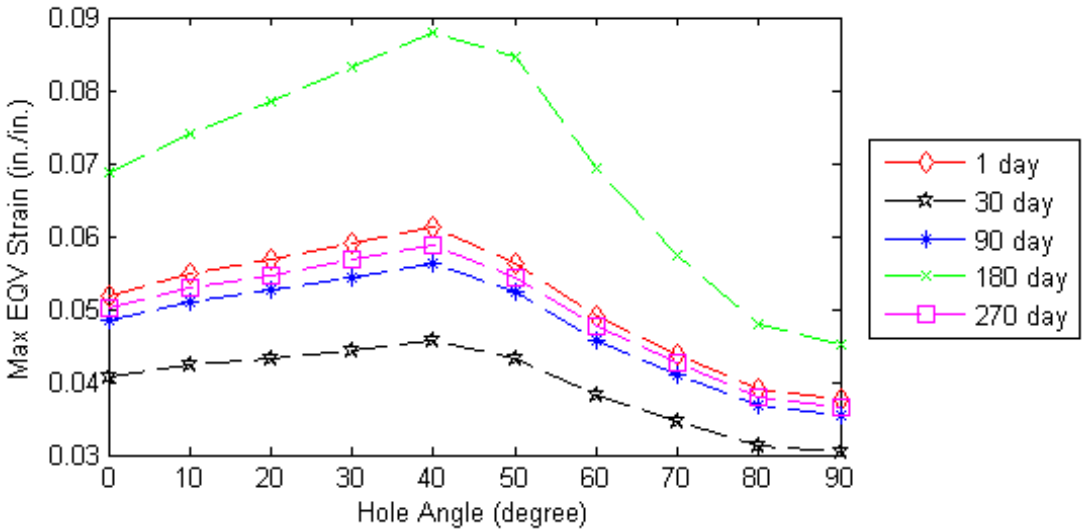

Figure 60 Cement maximum equivalent strain as a function of wellbore angle (pore pressure = 5,168 psi; 101-lbm/ft^3 cement)

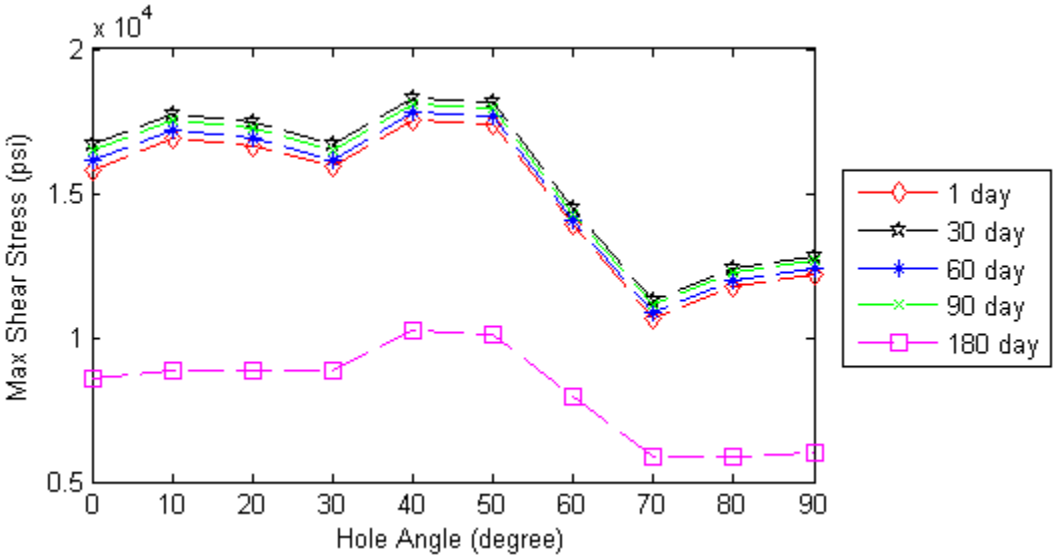

Figure 61 Cement maximum shear stress as a function of wellbore angle (pore pressure = 5,168 psi; 118-lbm/ft^3 cement)

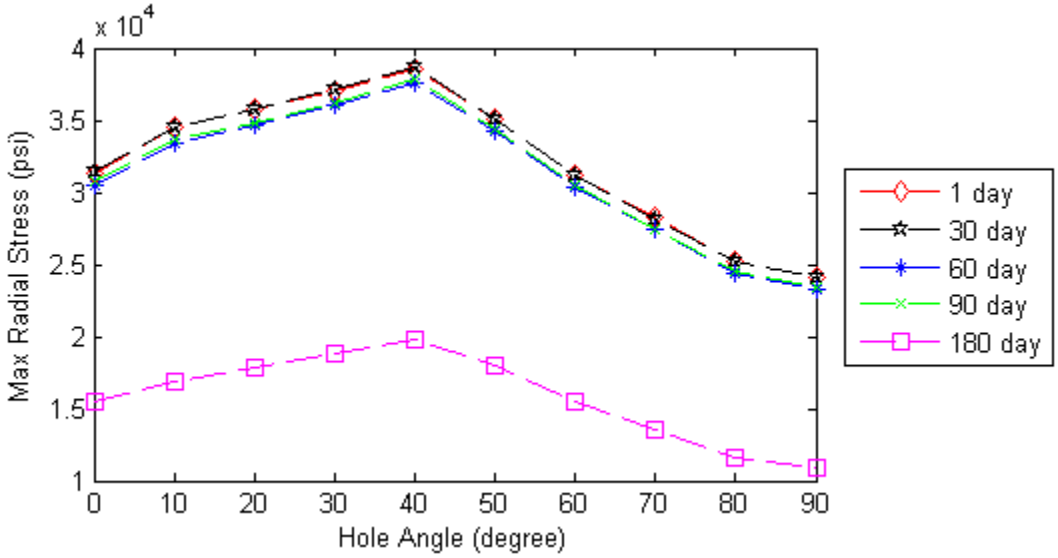

Figure 62 Cement maximum radial stress as a function of wellbore angle (pore pressure = 5,168 psi; 118-lbm/ft^3 cement)

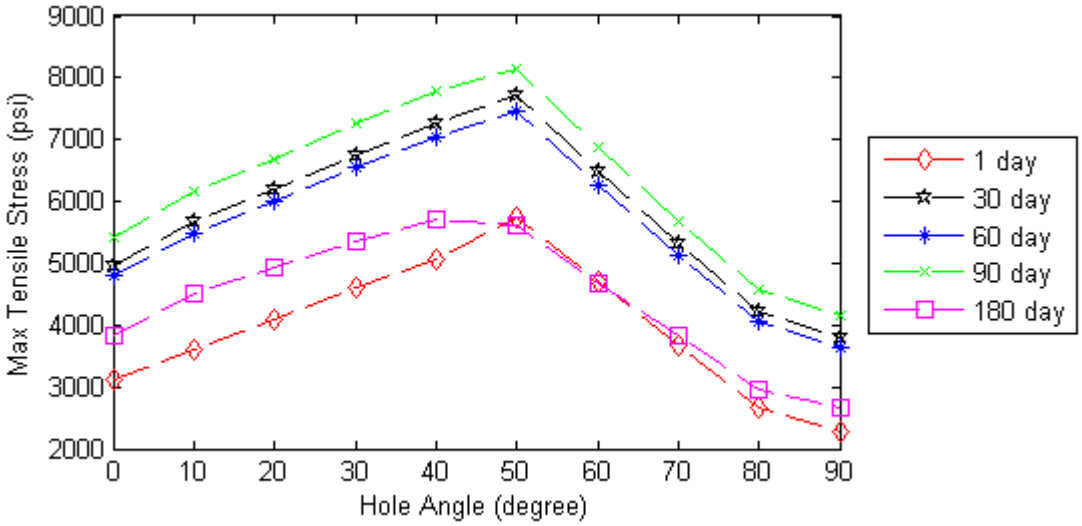

Figure 63 Cement maximum tensile stress as a function of wellbore angle (pore pressure = 5,168 psi; 118-lbm/ft^3 cement)

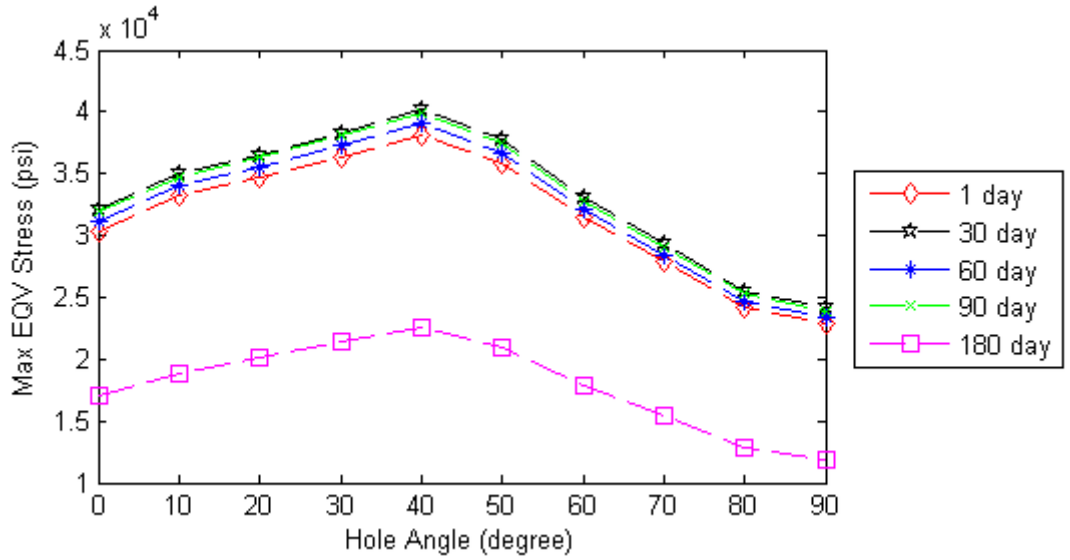

Figure 64 Cement maximum equivalent stress as a function of wellbore angle (pore pressure = 5,168 psi; 118-lbm/ft^3 cement)

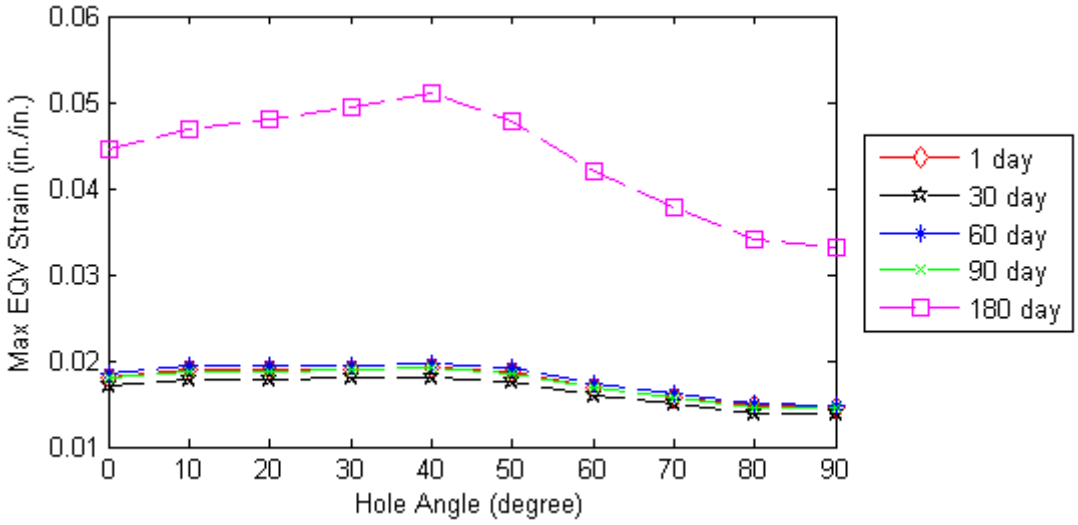

Figure 65 Cement maximum equivalent strain as a function of wellbore angle (pore pressure = 5,168; 118-lbm/ft^3 cement)

The majority of the cement deformation is permanent with only one or two percent being recoverable. Oilwell cements become very ductile, even under low-effective confining pressures. Simultaneously, the effect of high temperatures can help reduce the brittle-ductile transition pressure. Permanent shortening of transition pressure by 30% or more are attainable without rupture (John, 1968). Figure 55 shows that at 360 days, the cement strain increases from 0.062 to 0.08 at a wellbore angle of 40º and it then reduces to 0.05 at a wellbore angle of 90º. Even though the cement strain reaches 0.08, no failure occurs because the cement behaves ductile rather than brittle under high-confining pressure.

Figure 56 shows that the 101-lbm/ft^3 cement develops the highest shear stress at a wellbore angle between 40 and 50 degrees. The maximum shear stress values are almost constant with time at a certain wellbore angle. The 180-day data are quite different from the data tested at other times, so the 180-day test data cannot be used to estimate the results. For 101-lbm/ft^3 cement, Figure 57 to Figure 59 show the same trend for radial stress, tensile stress, and equivalent stress as the trend for shear stress. From Figure 60, the cement develops the maximum strain of 0.06 at a borehole angle of 40º.

Figure 61 shows that the 118-lbm/ft^3 cement develops the highest shear stress of 17,000 psi at a wellbore angle of 40º. The maximum shear stress values are also almost constant along with time at a certain wellbore angle. The 180-day data are also quite different from the data tested at other times, so the 180-day test data cannot be used to estimate the results. For 118-lbm/ft^3 cement, Figure 62 to Figure 64 show the same trend for radial stress, tensile stress, and equivalent stress as the trend for shear stress. From Figure 65, the cement develops the maximum strain of 0.019 at wellbore angle of 40º.

5.4.1 Highest Failure-Probability Envelope

For the three cement systems being evaluated, the cement highest failure-probability zones were plotted at pore pressures of 5,168 psi and 10,000 psi. The wellbore angle ranges from 0 to 90º and the time extends from 1 day to 360 days. The data between different wellbore angles and times were calculated by a cubic interpolation method to ensure data continuity. As shown in Figure 66, for the 72-lbm/ft^3 cement, the highest failure probability zone occurred at 7 and 60 days with a wellbore angle of 20 to 55º. The compressive stress highest failure-probability zone was approximately 180 days. For the 101- lbm/ft^3 cement, Figure 67 shows that the highest failure-probability zone occurred from 10 to 60 days between the wellbore angle of 25 to 55º. For the 118- lbm/ft^3 cement, Figure 68 shows that the highest failure-probability zone is at a wellbore angle of 30 to 50º from 1 day to 140 days.

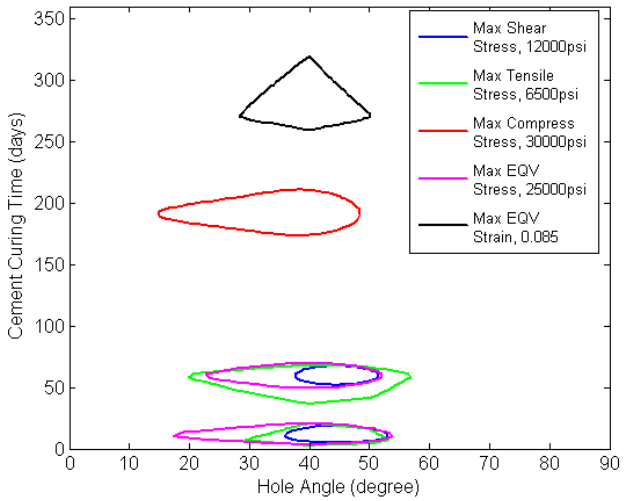

Figure 66 Cement highest failure-probability zone (pore pressure = 5,168 psi; 72-lbm/ft^3 cement)

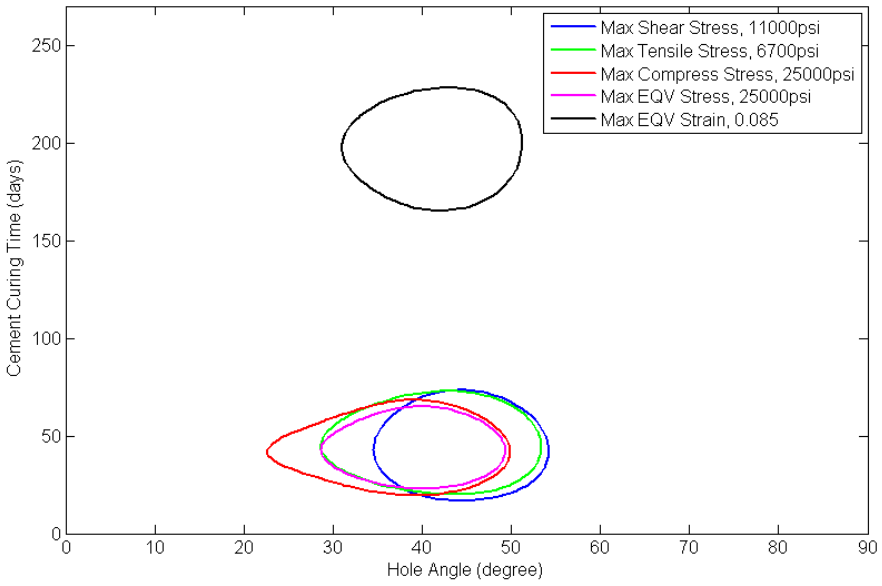

Figure 67 Cement highest failure-probability zone
(pore pressure = 5,168 psi; 101-lbm/ft^3 cement)

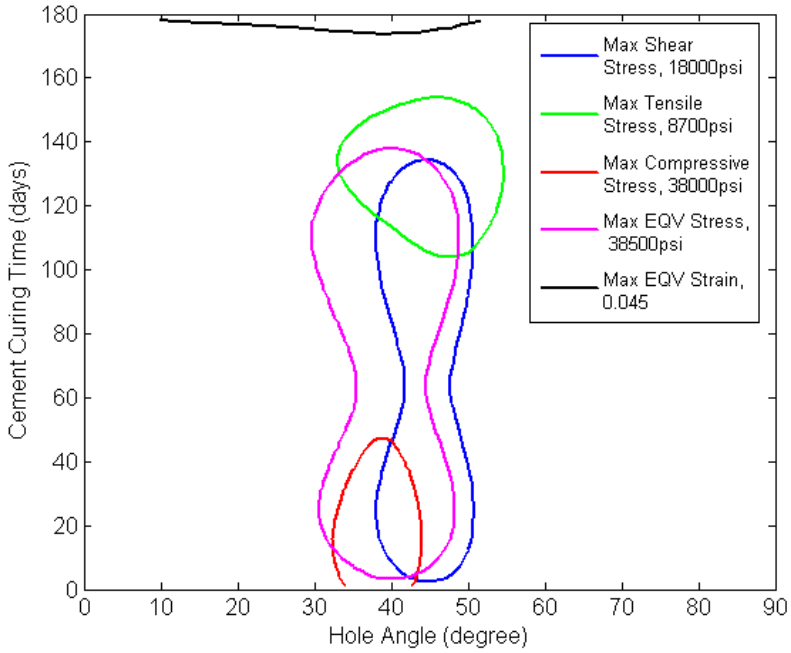

Figure 68 Cement highest failure-probability zone
(pore pressure = 5,168 psi; 118-lbm/ft^3 cement)

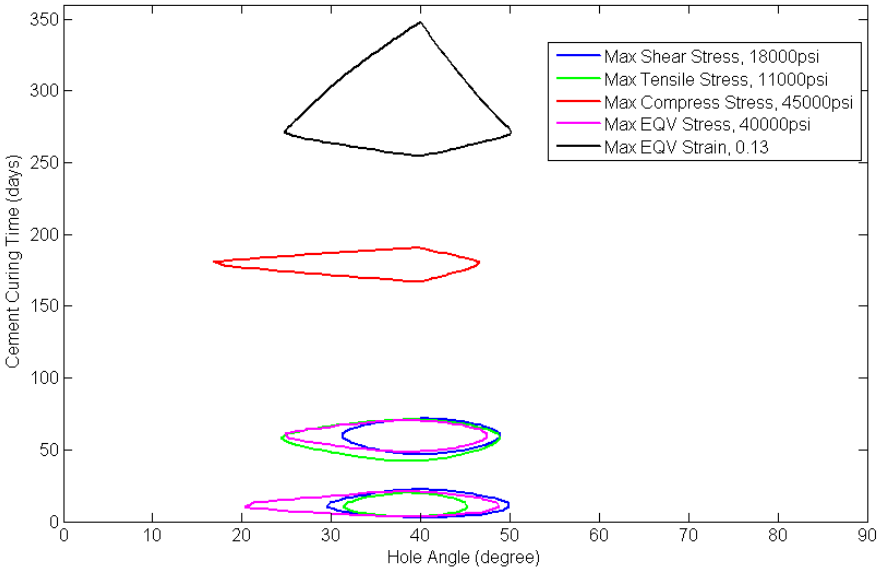

Figure 69 Cement highest failure-probability alone
(pore pressure = 10,000 psi, 72-lbm/ft^3 cement)

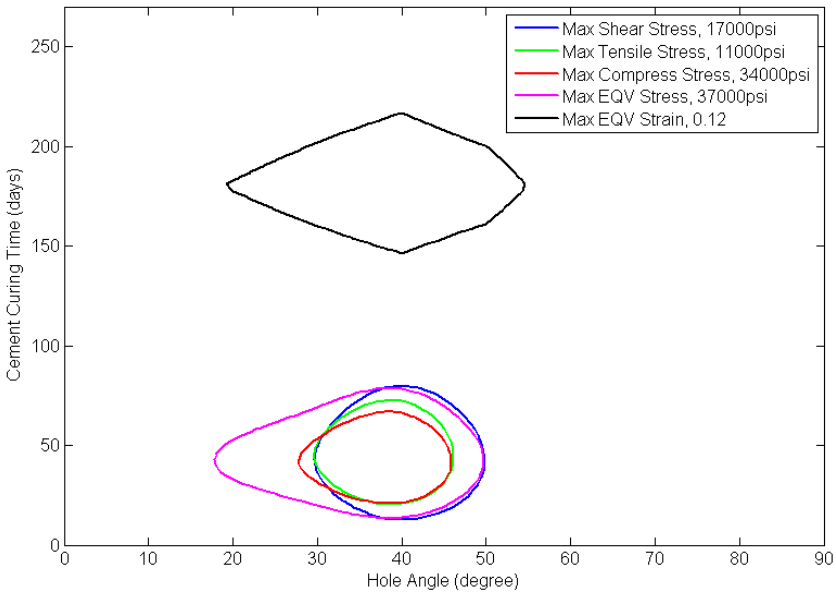

Figure 70 Cement highest failure-probability zone
(pore pressure = 10,000 psi; 101-lbm/ft^3 cement)

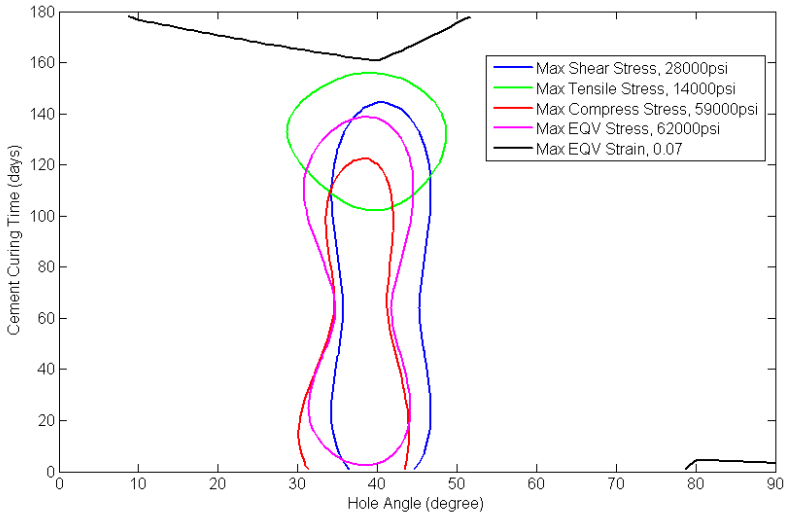

Figure 71 Cement highest failure-probability zone
(pore pressure = 10,000 psi; 118-lbm/ft^3 cement)

Figure 69, Figure 70, and Figure 71, at 10,000-psi pore pressure, show that the cement has almost the same highest failure-probability zone as it does at the lower pore pressure. The highest failure-probability envelopes can be used at any pore pressure for the same type of cement.

5.4.2 Effect of Wellbore Angle

It is clearly shown in Figure 51 to Figure 65 that for the three cement systems, as the wellbore angle increase from vertical to 40º, the cement stress and cement strain tend to increase. At a wellbore angle between 40 and 50º, the cement stress and cement strain reaches the highest value; therefore, the cement highest failure-probability angle is between 40 and 50º. As the wellbore angle continues to increase from 50 to 90º, the cement stress and strain tends to decrease.

5.4.3 Effect of Time

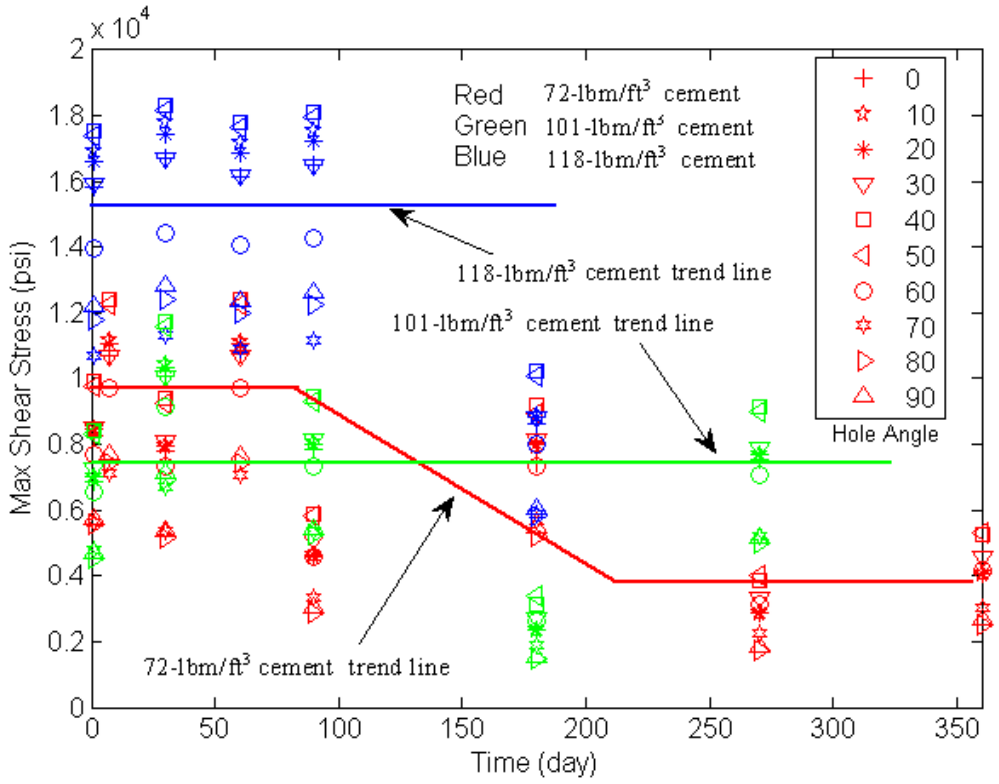

Figure 72 Cement maximum shear-stress evolution with time (pore pressure = 5,168 psi.)

From Table 12, for the 72-lbm/ft^3 cement, Young's modulus and Poisson's ratio decreases with time and then holds constant at 270 days. Neglecting the test data at 180 days, Young's modulus increases slightly with time and Poisson's ratio decreases slightly with time for the 101-lbm/ft^3 cement and the 118-lbm/ft^3 cement. The cement mechanical properties change can be explained by the stress change. It is clearly shown in Figure 72 that for the three cements, the shear-stress trend line and time are different; i.e., the 118-lbm/ft^3 cement and 101-lbm/ft^3 cement have a constant straight-line trend. However, the 72-lbm/ft^3 cement develops high-shear stress at the beginning and then decreases to a constant value after 270 days. The 72-lbm/ft^3 cement shows improvement with time.

5.5 Conclusions

(1) Low-density cements are successfully applied in low-fracture-gradient formations to control lost circulation.

(2) In the long term, 72-lbm/ft^3 cements show improvement in the stress reduction with time. The 72-lbm/ft^3 cement failure probability decreases with time because the cement shear stress, tensile stress, and compressive stress all decrease with time. The 101-lbm/ft^3 cement and 118-lbm/ft^3 cement does not clearly show improvement in the stress reduction with time.

(3) The highest failure-probability zone is between a wellbore angle of 40 to 50º. To cement operations, focus should be on this range of wellbore angles.

(4) Under high-pressure conditions, the cement becomes more ductile and flexible. More than 10% cement strain is developed in the 72-lbm/ft^3 cement under the 10,000-psi pore pressure.

(5) Additional laboratory tests should be carried out to investigate the cement failure under high-confining pressure because the cement behavior under high-confining pressure is quite different from the zero-confining pressure.

CHAPTER VI

CASING BUCKLING FAILURE CHARACTERISTICS IN RESERVOIR COMPACTION

6.1 Introduction

Withdrawal of oil and gas in an overpressured reservoir usually results in a large fluid-pressure drop. Meanwhile, the overburden load originally carried by the pore fluid shifts to the porous skeleton, causing an increase in effective stress. During the depletion of an overpressured reservoir, sediment around the wellbore deforms mainly in the vertical direction. The high-stiffness of steel causes the overburden load to be concentrated on the casing, resulting in a large increase of axial casing stress and strain. In the study of reservoir compaction, the casing buckling failure is considered on a large scale (Chia and Bradley 1989; Ahmed et al., 2003; Shen 2010) and does not show the casing-deformation failure process in detail.

For casing design, Euler buckling is considered when the casing is installed and the cement is still in a fluid state. Under these conditions, the axial load at any point between the surface and the bottom of the string is the summation of all the loads acting below this point. Pipe buckling occurs when the total effective axial force exceeds the average of the radial and tangential forces (Rahman and Chilingar 1995). The buckling behavior of drillpipe and coiled tubing was extensively studied with regard to the behavior of sinusoidal buckling and helical buckling from vertical wells to horizontal wells (Dawson and Paslay 1984; Chen et al. 1990; Wu and Hans, 1995). The pipe was modeled using 3D linear beam elements (PIPE31) with pipe sectional properties (ABAQUS Technology Brief 2009). The interaction between the coiled tubing and the wellbore casing was modeled using 3D tube-in-tube interface (ITT31) elements.

In the field of thermal well-casing buckling, the casing was studied by the ABAQUS platform using 3D beam elements capable of simulating large deformations. The outer radial boundary over the unsupported interval was conservatively assumed to be very stiff, providing rigid radial support for the casing if it deformed sufficiently to contact the wellbore wall. The interaction between the casing and the rigid wellbore was modeled using pipe-in-pipe contact elements (Xie and Liu 2008). The 3D model was built by the ANSYS platform to examine the buckling strength of the production casing in geothermal wells (Lilja 2009). The contact element type used in the 3D model is CONTA174 and the target element type is TARGE170. In the buckling

analysis of the well, a 20-MPa sideward pressure is defined at a small area. The sideward pressure is modeled to simulate the buckling strength if fluid is trapped outside the production casing and its thermal expansion causes sideward pressure, which acts on the casing.

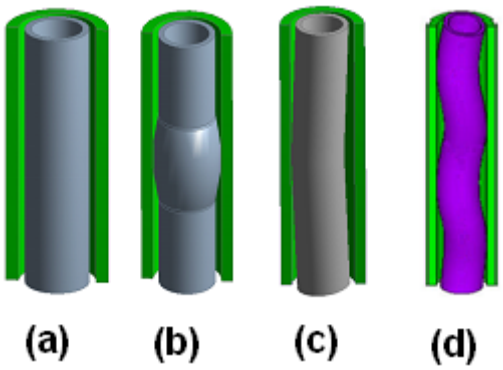

(a) Initial configuration (b) Local Plastic Deformation (c) Euler Buckling (d) Helical or Sinusoidal Buckling

Figure 73 Casing buckling-failure modes

The three types of casing deformation modes are shown in Figure 73. For short unsupported lengths of casing, only localized plastic deformation would be expected while in longer unsupported lengths of casing, Euler buckling would occur. Helical buckling, which occurs in long unsupported casing lengths, has a small probability of occurring even in a bad cement job. This study focuses on localized plastic deformation and Euler buckling and shows the casing buckling deformation behavior in much more detail.

6.2 Methods

6.2.1 Geomechanical Model

During the depletion of a reservoir, the pore pressure decreases with time, and the additional vertical stress induced by reservoir compaction can be calculated by Equation (6.1).

$$\Delta S_v = \alpha \Delta P_b \frac{1-2\nu}{1-\nu} \frac{\ln\left(h/R_b\right)}{\ln\left(R_d/R_b\right)} \tag{6.1}$$

where the Biot-Willis coefficient α is expressed as

$$\alpha = 1 - \frac{C_r}{C_{bc}} \tag{6.2}$$

The formation vertical strain can be calculated by

$$\delta = \frac{S_v + \Delta S_v}{E} \tag{6.3}$$

The casing is assumed to have the same vertical displacement as the formation; therefore, the strain calculated from Equation (6.3) can be applied to the casing.

6.2.2 FEM Analysis Methods

FEM analysis methods can more accurately predict casing buckling because the analysis can simulate the casing buckling process and provide much more detail information about the casing deformation. The ANSYS software is the platform used to develop codes to carry out the casing-buckling analysis.

6.2.2.1 Nonlinear Casing-Buckling Analysis

Nonlinear casing-buckling analysis employs nonlinear, large-deflection, static analysis to predict the buckling loads. These casing-buckling loads gradually increase the applied load until a load level is found whereby the structure becomes unstable (suddenly, a very small increase in the load will cause very large deflections). The true nonlinear nature of this analysis permits the modeling of geometric imperfections, load perturbations, material nonlinearities, and gaps. For this type of analysis, small off-axis loads are necessary to initiate the desired buckling mode.

6.2.2.2 Elements

A discrete annular gap that exists between the casing outside diameter and the adjacent cement or formation generates a void region.

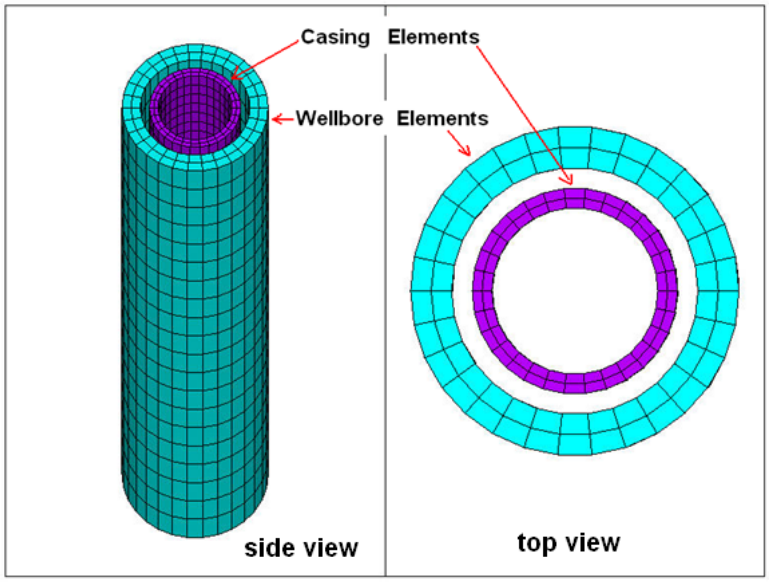

Figure 74 Casing and wellbore elements

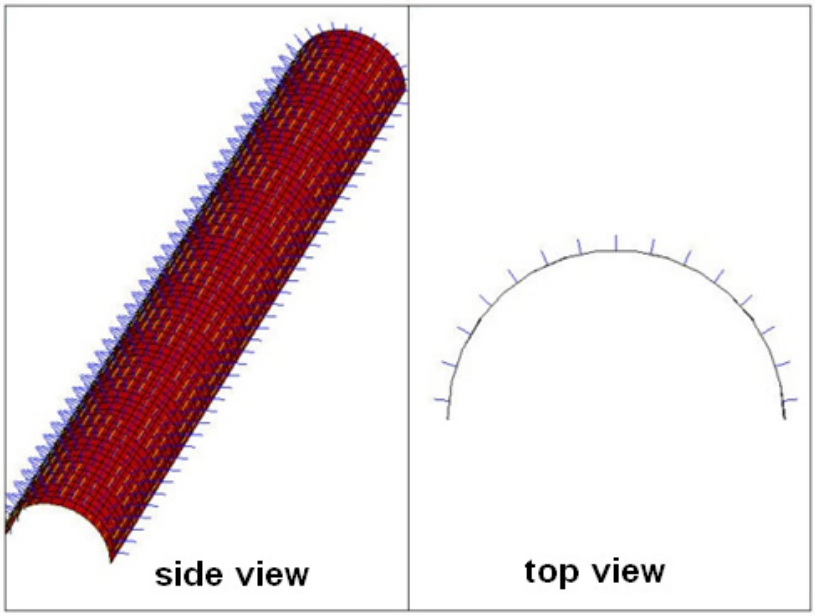

Figure 75 Contact elements

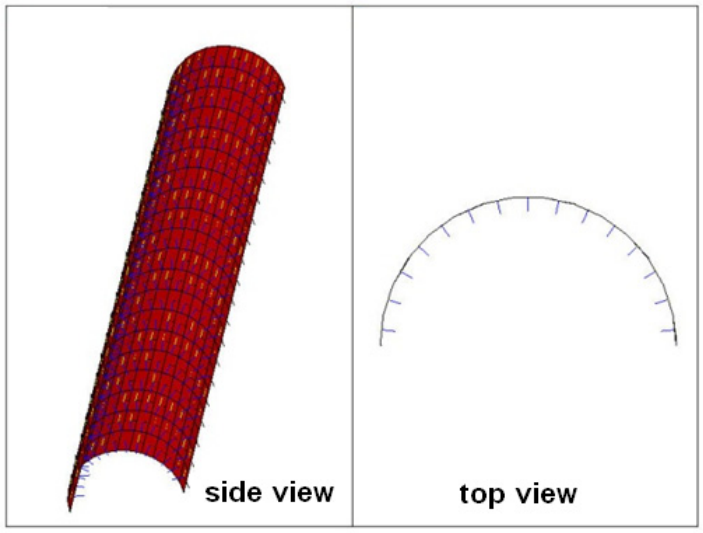

Figure 76 Target elements

As shown in Figure 74, for the casing, the length of the radial direction was divided by two elements; the circle length was divided by 40 elements. The casing and formation are meshed with the SOLID45 element. The casing top surface and formation top surface are meshed with SHELL63, and then the VSWEEP command was used to generate the casing and formation element with an element size of 1 in. in the vertical direction. As shown in Figure 75, the CONTA174 element was used for the contact face that is the outside casing face. From Figure 76, the TARGE170 element was used for the target face, which is the inside face of the wellbore or the cement.

6.2.2.3 Boundary Conditions

Grade P110, 5-in. casing was used with the 6-in. borehole diameter. The bottom face of the casing and the formation were fixed, and the formation inside face was also fixed. The contact between the casing and the wellbore was set for zero penetration so that the casing cannot penetrate the formation. A vertical displacement of 10 in. was applied at the top of the casing for casing nonlinear buckling analysis. The top face of the casing had 0.01-in. displacement applied in the x direction to initiate casing buckling. In the nonlinear solution, 40 substeps were used.

6.3 Results

6.3.1 The Shape of Casing Deformation

The process of casing deformation in reservoir compaction was studied. In the analysis of the shape of the casing deformation, casing radial displacement at different load substeps was read. The maximum casing radial displacement is 0.5 in. because the casing is 5-in. OD and the wellbore diameter is 6 in.; thus, with this displacement, the casing is in contact with the wellbore.

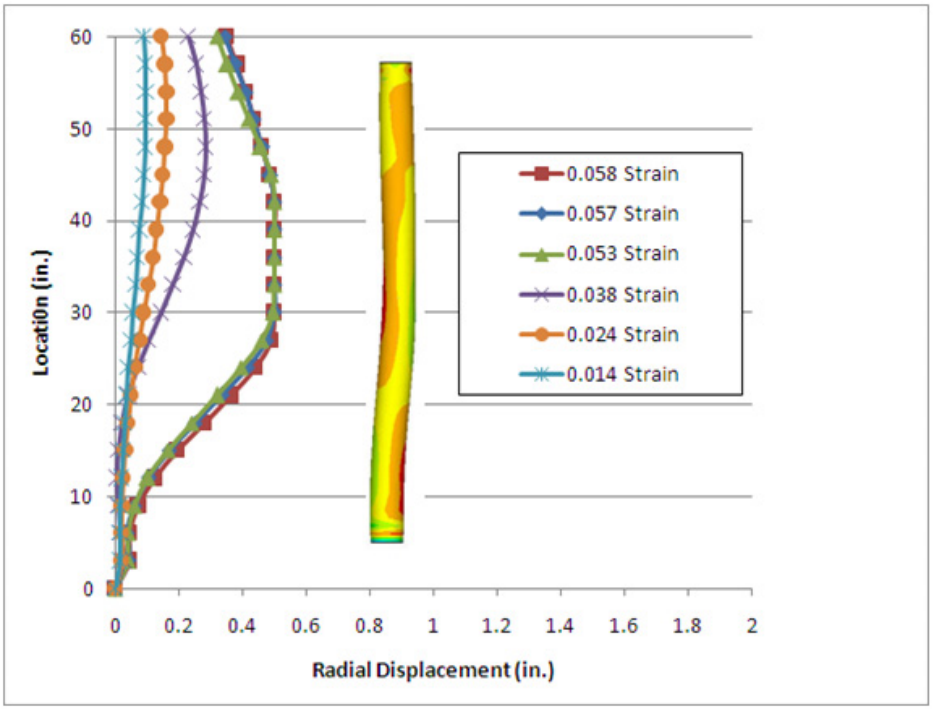

Figure 77 Casing deformation shape

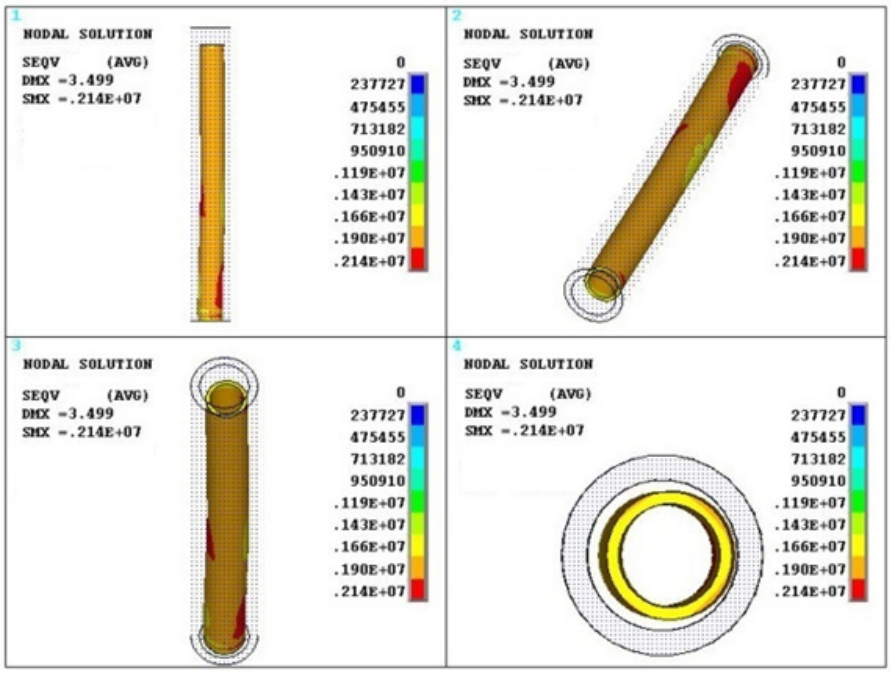

Figure 78 Casing deformation shape with a 0.058 strain

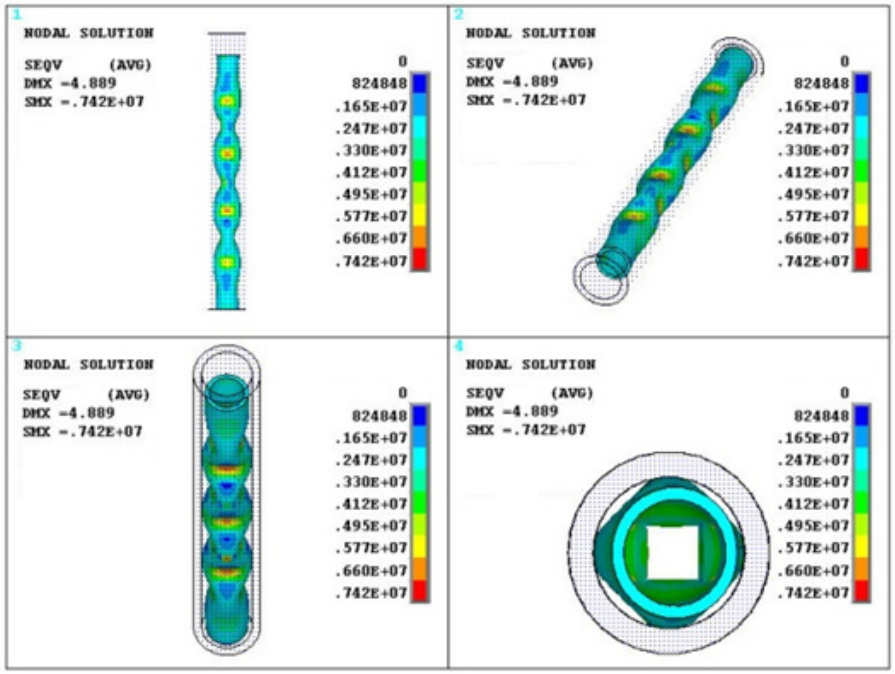

Figure 79 Casing deformation shape with a 0.067 strain

From Figure 77, as the casing strain increases from 0.014 to 0.058, the maximum radial displacement moves from the top to the lower portion of the casing. After the casing strain exceeds the casing buckling strain of 0.044, the casing with a height from 30 in. to 45 in. is in contact with the formation, which is the casing local plastic deformation. The casing deformation shape at the strain of 0.058 is shown in Figure 78. As the casing strain continues to increase to 0.067, the casing fails completely as shown in the shape of Figure 79.

6.3.2 Casing Buckling with Different Unsupported Casing Lengths

Buckling is initiated immediately after the casing yields. Localized plastic deformation and Euler buckling are evaluated in this study. The Euler buckling equation is expressed in Equation (6.4).

$$F = \frac{\pi^2 EI}{(KL)^2} \tag{6.4}$$

Rearranging Equation (6.4), the casing strain at Euler buckling can be calculated by Equation (6.5).

$$\delta = \frac{F}{AE} = \frac{\pi^2 \left(OD^2 + ID^2\right)}{16(KL)^2} \tag{6.5}$$

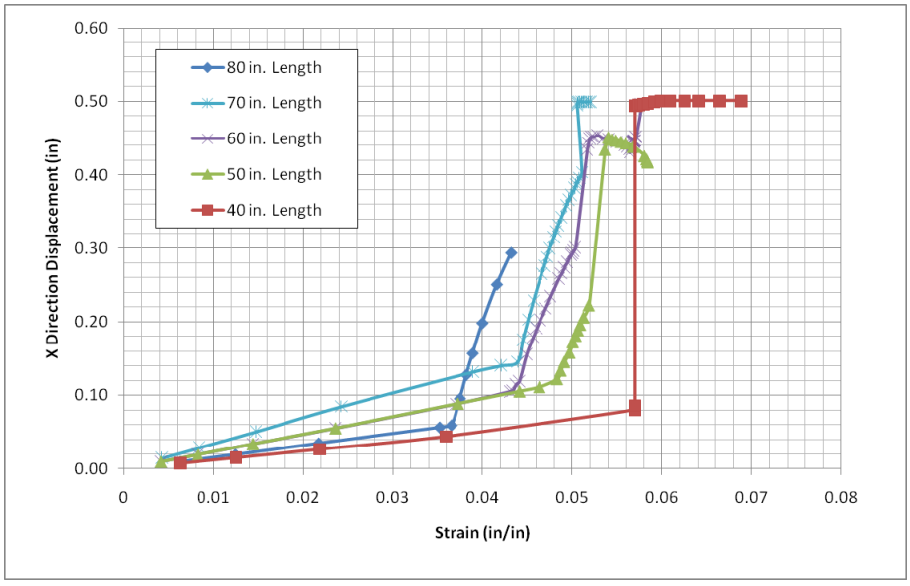

Figure 80 Casing x-direction displacement for different unsupported casing lengths

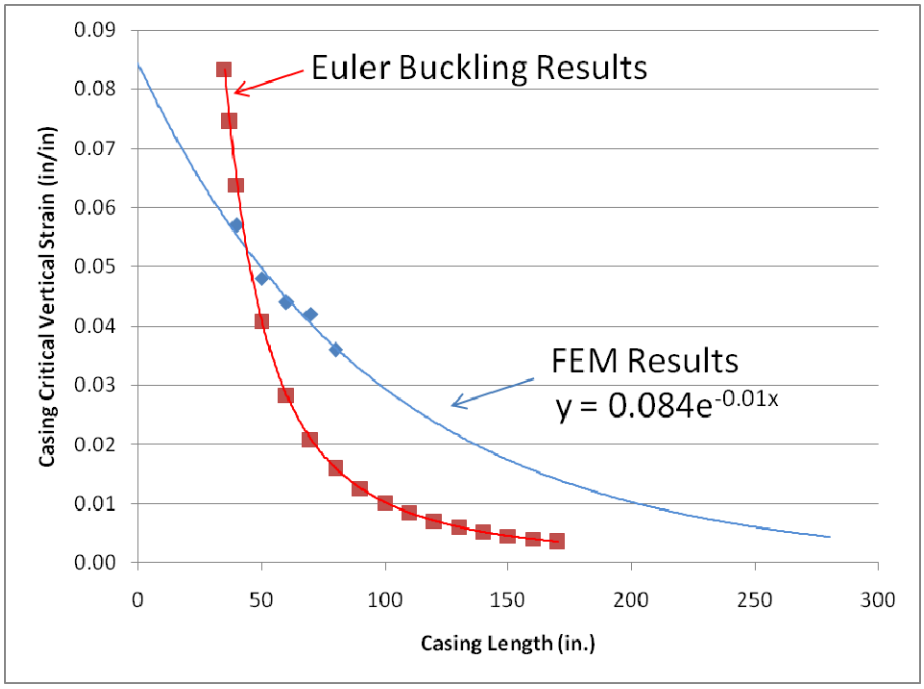

Figure 81 Casing critical strain as a function of unsupported casing length

Figure 80 shows the relationship between the casing top point x-direction displacement and the casing strain. When the x-direction displacement is 0.5 in., the casing is in contact with the wellbore. It is clearly seen that the casing buckles when there is sharp increase in the x-direction displacement. As shown in Figure 81, the critical casing strain calculated by Euler equation is higher than the results obtained by FEM analysis methods when the casing length is less than 40 in. The critical casing strain calculated by Euler equation is lower than the results obtained by FEM analysis when the casing length is greater than 40 in. The new equation proposed by the FEM results is expressed in Equation (6.6).

$$\delta = 0.084 \exp(-0.01L) \tag{6.6}$$

The casing critical-buckling strain is too high to be realistic for the short casing length, so Equation (6.6) proposed by the FEM results can more accurately predict the casing critical strain.

6.3.3 Casing Buckling with Different Borehole Diameters

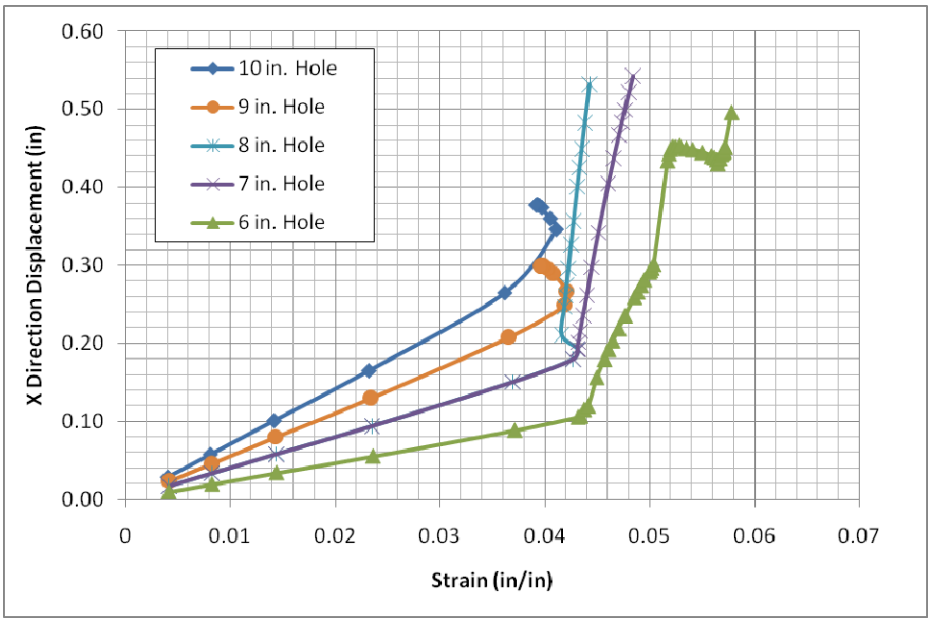

Figure 82 Casing critical strain vs. an unsupported borehole diameter (60-in. casing length)

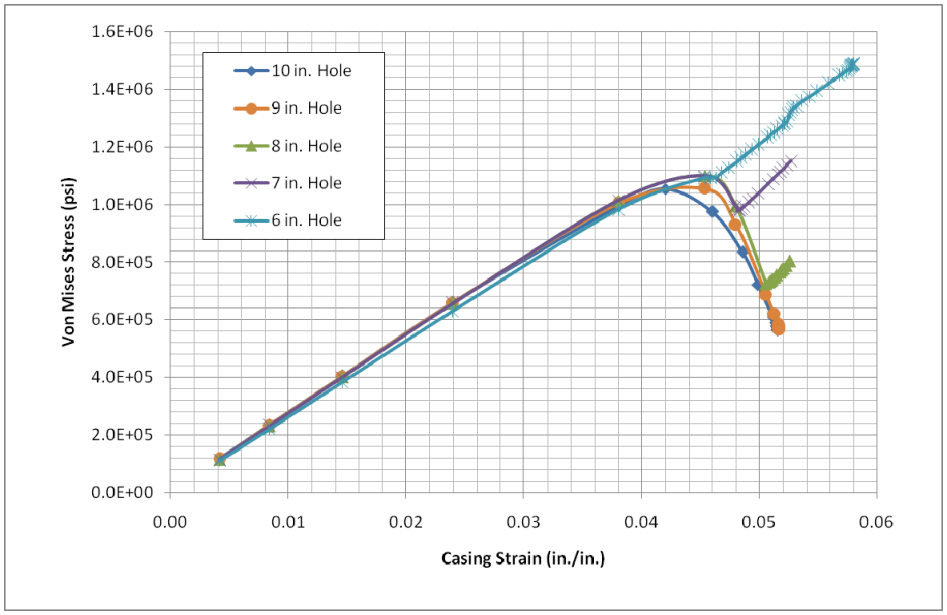

Figure 83 Casing critical strain vs. unsupported borehole diameter

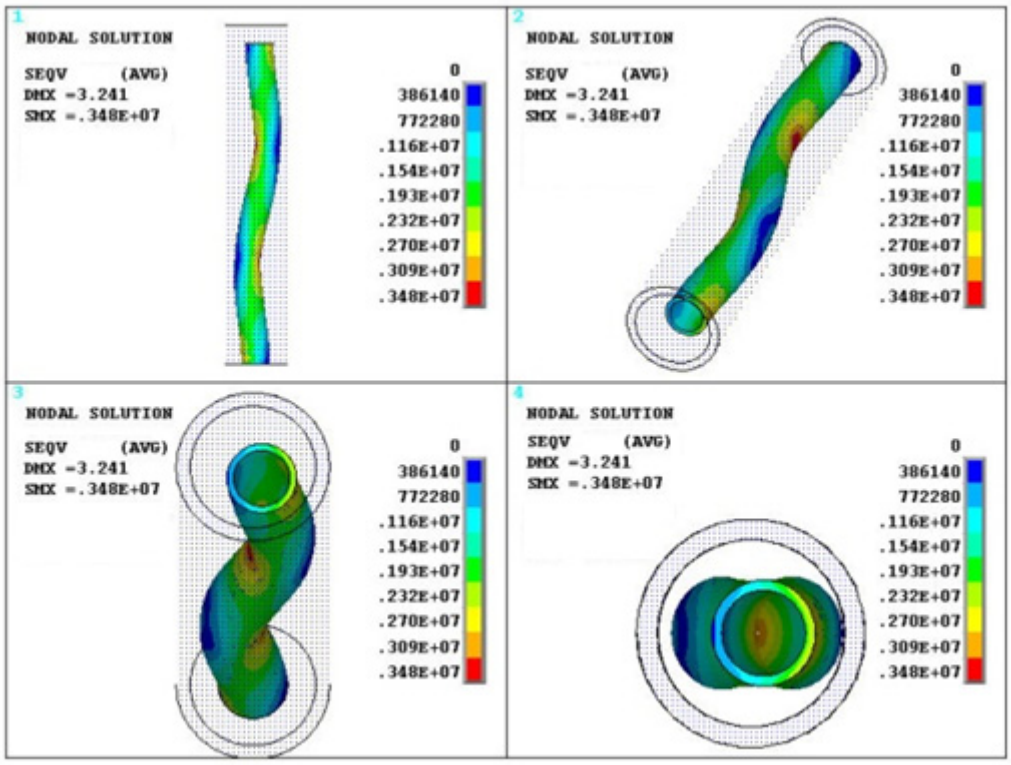

Figure 84 Casing deformation shape in a 9-in. diameter borehole

From Figure 82 and Figure 83, the casing buckles when there is a sharp increase in the x-direction displacement and a sharp decrease in the casing von Mises stress. The casing critical-buckling strain is shown more clearly in Figure 82 than it is in Figure 83. For different borehole diameters, at a casing length of 60 in., as the borehole diameter increases from 6 in. to 10 in., the casing critical-buckling strain decreases from 0.042 to 0.0405. Figure 83 shows the casing von Mises stress decreases sharply when the casing buckles and increases after the casing is in contact with the formation. For a 9- in. borehole diameter, the shape of the casing buckling is shown in Figure 84.

6.3.4 Casing Buckling with Different Casing-Wall Thickness

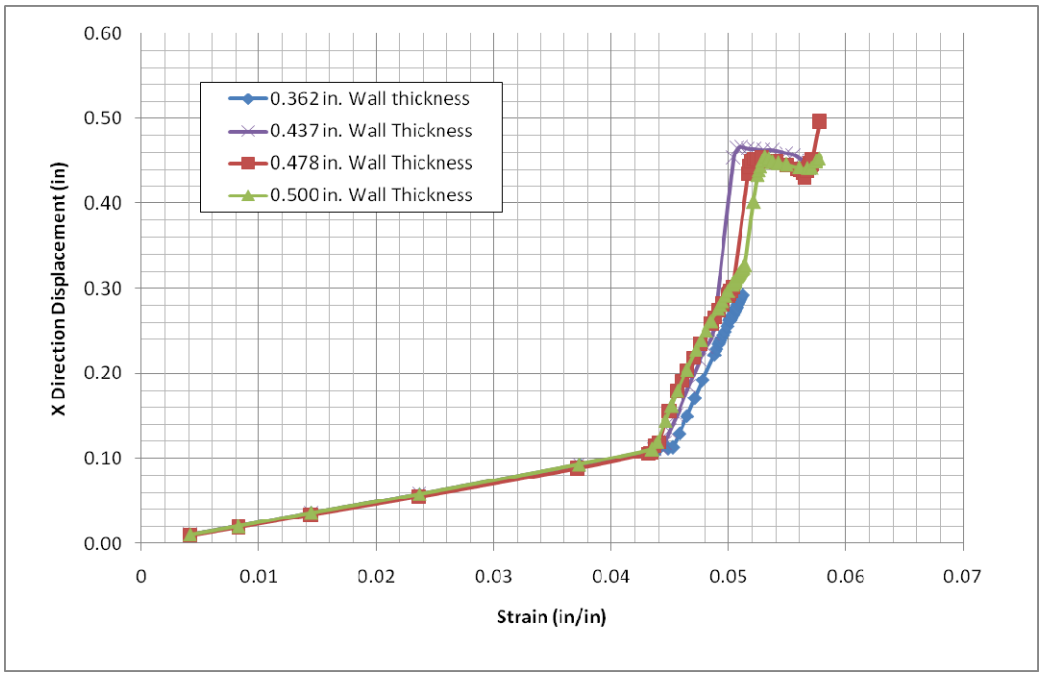

Figure 85 Casing x-direction displacement vs. casing strain

Figure 85 shows that the casing buckles under the strain of 0.044 when there is a sharp increase in the x-direction displacement. For different wall thicknesses, the casing critical-buckling strain is almost the same. If the casing has the same vertical strain as the formation, using thicker wall casing to prevent casing buckling failure does not work better than the conventional casing.

6.4 Conclusions

(1) The shape of casing deformation in reservoir compaction was studied. Euler buckling, local plastic deformation and complete buckling failure are experienced in the process of casing buckling.

(2) The new equation proposed by FEM results can more accurately predict casing critical-buckling strain than can the Euler's method. The critical buckling strain decreases as the unsupported casing length increases.

(3) As the borehole diameter increases, for the same unsupported casing length, the critical buckling strain decreases a small amount. For unsupported casing, enlarging the borehole has a minor effect on the casing buckling critical strain.

(4) For different casing wall thicknesses, the critical buckling strain is almost the same. If the casing has the same vertical strain as the formation, using a thicker wall casing to prevent casing buckling failure does not function any better than the conventional casing.

CHAPTER VII

CASING FAILURE CHARACTERISTICS UNDER HPHT CONDITIONS IN A SOUTH TEXAS FIELD

7.1 Introduction

In a south Texas oil and gas field at the present time, 18 wells have been drilled and completed where sand formations in the reservoir are producing gas and some oil. The reservoir is a shale-sand sequence with an average porosity of 10 to 18% and a low permeability under 0.001 md. For these reasons, the reservoir is considered to be a tight reservoir. Petrographic analysis reveals that the formation material consists of a mixture of shale, shaly siltstone, calcareous shaly siltstone, and small amounts (<10 to 20%) of calcareous, shaly, very fine-grained sandstone. Core analysis showed that sandstones are very fine to fine grained. The mean grain size of the sandstones ranges from 0.07 mm (lower very fine sand) to 0.22 mm (upper fine sand). The average grain size for all of the samples is 0.11 mm (lower fine sand).

The sand formations are over pressured. The vertical stress gradient is 1.05 psi/ft., the pore pressure ranges from 0.85 to 0.93 psi/ft, and is approximately 0.93 psi/ft in the zone of interest. The fracture gradient for the sandstones ranges from 0.91 to 0.95 psi/ft and is approximately 0.95 psi/ft in the zone of interest. The fracture gradient for shale is 0.97 to 0.98 psi/ft and is up to 1.00 psi/ft. This condition leads to a very narrow operational window (pore pressure-fracturing pressure). Casing damage was experienced in 11 out of the 18 wells that have been drilled in the area; i.e., nearly 61% of total wells were damaged during their production life. For the failure problems, 61% had casing collapse, 8% had casing parting, and 31% were fill/sand production problems. At the same time, most of the failure locations were in shale zones, which accounts for 62% of the failure. Only 38% failure occurred in the perforation zones

7.2 Formation Shear Failure

Formation movement caused by pore-pressure reduction leads to casing collapse as the movement increases external stress onto nearby casing. In a production well, reduction in pore pressure induces changes in formation stresses, causing the formation to fail. Shear failure is the likely mode of failure where rock formation slips on a failure plane. In tight gas formations, formation shear failure can be a positive effect to the production rate because shear failure creates fractures on the failure plane. However, in south Texas where casing collapse is a

problem, predicting the maximum amount of production before failure occurs should be a priority.

An analytical geomechanical model was used to compute the change in the magnitudes of formation stress as a result of production drawdown and production depletion pressures. With this model, maximum pore pressure reduction can be predicted before formation failure. This model was applied to vertical wells giving initial formation stresses and production profile to determine changes in vertical stress and horizontal stress. Using the results, we can calculate the level of pore pressure that can cause a wellbore to collapse.

7.2.1 Analytical Model

The assumption of this model is: (1) The reservoir is a cylindrical disk in which the reservoir depth is very deep compared to its thickness; (2) reservoir boundaries do not provide a driving mechanism and are not depleting rocks; (3) reservoir and boundary rocks have the same mechanical properties and are homogeneous and isotropic; (3) the model is a linear poroelastic model; (4) the wellbore radial stress is equal to only the pore pressure.

The equations shown below are used to compute the changes in horizontal stress and vertical stress.

$$\Delta S_v = \alpha \Delta P_{d,b} \frac{1-2\nu}{1-\nu} \frac{\ln\left(h/R_b\right)}{\ln\left(R_d/R_b\right)} \tag{7.1}$$

$$\Delta S_h = \alpha \Delta P_{d,b} \frac{1-2\nu}{1-\nu} - \frac{\Delta S_v}{2} \tag{7.2}$$

In a vertical well, there are three total principal stresses acting along the wellbore. The radial stress (S_r) acts horizontally on the surface of the wellbore along the longitudinal direction. The tangential stress (S_θ) or hoop stress acts in the tangential direction around the wellbore, and the axial stress (S_z) acts in the vertical direction on the wellbore. From the assumption, the radial stress is assumed to be the pore pressure around the wellbore while the axial stress is the overburden stress at the reservoir depth. The tangential stress, which is related to the formation horizontal stress, can be expressed as

$$S_\theta = 2S_h - P_w \tag{7.3}$$

Knowing all three total principal stresses allows us to calculate the shear stress of the formation. The shear stress is then compared to the maximum shear-stress data received from triaxial testing

in a laboratory. This condition allows us to predict the production profile so that formation shear stress does not exceed its maximum, which will cause rock to slip and move onto the casing.

7.2.2 Boundary Conditions

Most of data were known to compute maximum shear stress accurately, except for the pressure profile data. In the study, the reservoir input data and pressure profile data are assumed as shown in Table 12 and Table 13.

Table 12 Reservoir input data

Reservoir Radius	1,000 ft	Biot's Constant	0.77
Reservoir Thickness	80 ft	S_{v0}	11,830 psi
Wellbore Radius	4 in.	S_{h0}	11,900 psi
Poisson's Ratio	0.22	P_{f0}	11,800 ft

Table 13 Production profile input

Time (month)	Drawdown Radius (ft)	Drawdown Pressure (psi)	Depletion Pressure (psi)	Time (month)	Drawdown Radius (ft)	Drawdown Pressure (psi)	Depletion Pressure (psi)
0.01	120	-4,000	-100	12	12,000	-4,000	-3,000
0.02	600	-4,000	-200	18	12,000	-4,000	-4,000
0.03	1,200	-4,000	-300	24	12,000	-4,000	-5,000
0.25	2,400	-4,000	-700	30	12,000	-4,000	-6,000
1	6,000	-4,000	-1000	42	12,000	-4,000	-7,000
6	9,600	-4,000	-2,000	64	12,000	-4,000	-7,800

7.2.3 Formation Shear-Failure Results

This section presents the input data and results from the reservoirs in south Texas. Figure 86 shows the shear stress at the wellbore plotted against maximum shear stress for different rocks type.

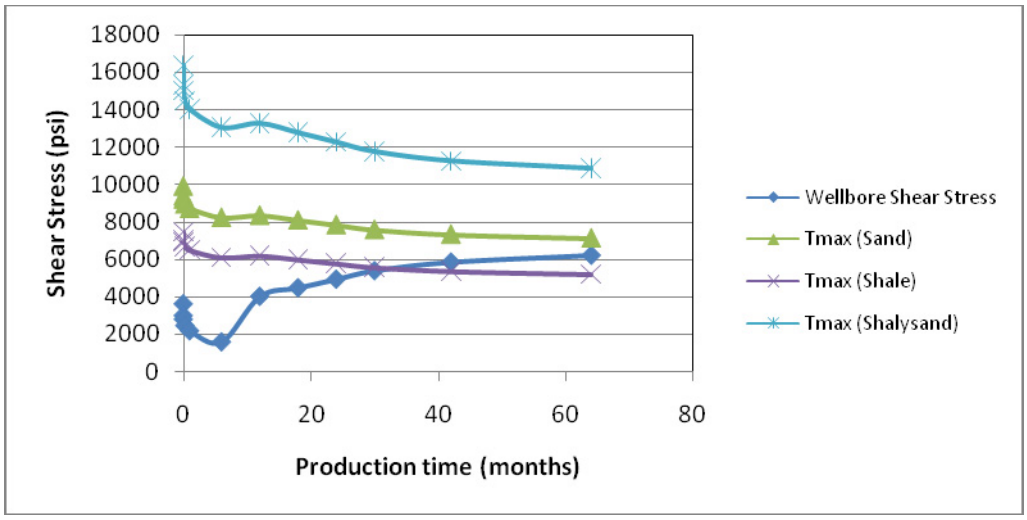

Figure 86 Wellbore shear stress as a function of time

Figure 86 shows that shale around the wellbore will start to collapse at shear stress levels of approximately 5,500 psi in 32 months after the start of production. This figure explains why casing collapse is likely to occur in shale sections more than in reservoir sandstone. Figure 87 shows maximum allowable pore pressure around the casing, which appears to be approximately 2,000 psi. If the pore pressure around the wellbore drops to below 2000 psi, wellbore collapse is likely to occur because of formation failure.

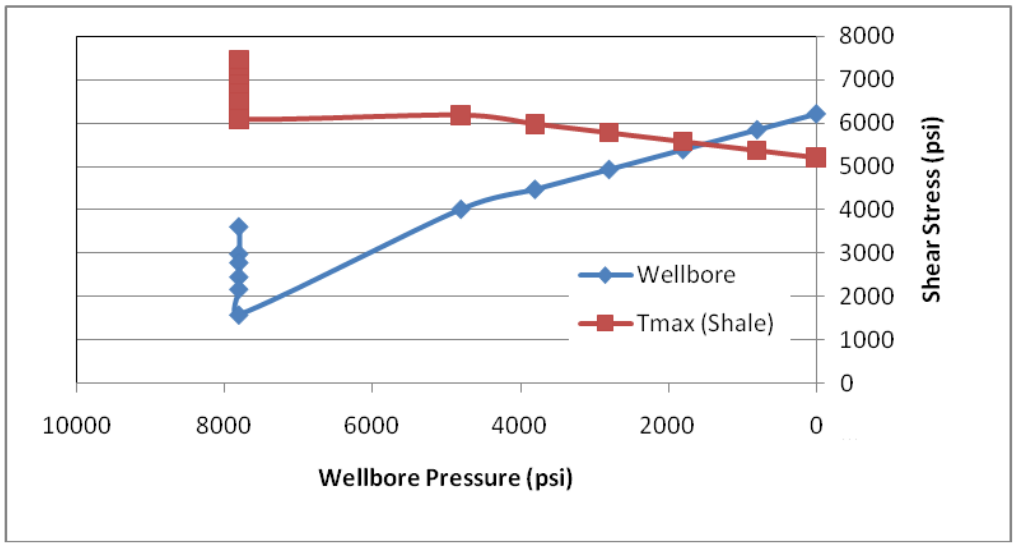

Figure 87 Wellbore shear stress as a function of bottomhole pressure

7.3 Fault and Fracture Activation by Pore-Pressure Reduction

Streit et al. (1999); Streit et al. (2001); Streit et al. (2002) studied the fluid pressured required to activate fault slip. For different fault types, the effective vertical stress is expressed as follows:

Strike-slip fault $\sigma_v^{'} = \sigma_2^{'} = \frac{\sigma_1^{'} + \sigma_3^{'}}{2}$

Reverse fault $\sigma_v^{'} = \sigma_3^{'}$

Normal fault $\sigma_v^{'} = \sigma_1^{'}$

For normal fault

$$\lambda_v = \frac{\sigma_v^{'}}{\sigma_v} = \frac{\sigma_v - P_f}{\sigma_v} = 1 - \frac{P_f}{\sigma_v} = \frac{-2C + (S_v - S_h)(1 - \mu \tan\theta)\sin 2\theta}{S_v 2\mu} + \frac{(S_v - S_h)}{S_v} \quad (7.4)$$

$$\frac{P_f}{S_v} = 1 - \frac{-2C + (S_v - S_h)(1 - \mu \tan\theta)\sin 2\theta}{S_v 2\mu} - \frac{(S_v - S_h)}{S_v} \quad (7.5)$$

$$P_f = P_{f0} - \Delta P_f \quad (7.6)$$

Substituting Equation (7.6) into Equation (7.5),

$$S_h = \frac{-2C + 2\mu\left(P_{f0} - \Delta P_f\right) + S_v \sin 2\theta - S_v \mu \sin 2\theta \tan\theta}{2\mu + \sin 2\theta - \mu \sin 2\theta \tan\theta} \tag{7.7}$$

$$b = \frac{\Delta S_h}{\Delta P_f} \tag{7.8}$$

$$S_h = S_{h0} - \Delta S_h = S_{h0} - b\Delta P_f \tag{7.9}$$

Substituting Equation (7.8) and Equation (7.9) into Equation (7.7),

$$\Delta P_f = \frac{-2C + 2\mu P_{f0} - \mu S_{h0} - S_{h0} \sin 2\theta}{2\mu - b\mu - b \sin 2\theta - b\mu \cos 2\theta} + \frac{-\mu S_{h0} \cos 2\theta + S_v \sin 2\theta - \mu S_v 2\left(\sin\theta\right)^2}{2\mu - b\mu - b \sin 2\theta - b\mu \cos 2\theta}$$

The fluid pressure required for faulting activation is given by

$$P_f = P_{f0} - \frac{-2C + 2\mu P_{f0} - \mu S_{h0} - S_{h0} \sin 2\theta}{2\mu - b\mu - b \sin 2\theta - b\mu \cos 2\theta} - \frac{-\mu S_{h0} \cos 2\theta + S_v \sin 2\theta - \mu S_v 2\left(\sin\theta\right)^2}{2\mu - b\mu - b \sin 2\theta - b\mu \cos 2\theta}$$

For a reverse fault,

$$P_f = P_{f0} - \frac{-2C + 2\mu P_{f0} - S_v 2\mu - S_v(1 - \mu \tan\theta)\sin 2\theta}{2\mu + b(\sin 2\theta - \mu + \mu \cos 2\theta)} - \frac{S_{h0}(\sin 2\theta - \mu + \mu \cos 2\theta)}{2\mu + b(\sin 2\theta - \mu + \mu \cos 2\theta)}$$

For a strike-slip fault,

$$P_f = P_{f0} - \frac{-2C + 2\mu P_{f0} - S_v 2\mu - S_v(\sin 2\theta + \mu \cos 2\theta)}{2\mu + b(\sin 2\theta + \mu \cos 2\theta)} - \frac{S_{h0}(\sin 2\theta + \mu \cos 2\theta)}{2\mu + b(\sin 2\theta + \mu \cos 2\theta)}$$

Calculating fluid-pressure levels that are predicted to induce faulting are conducted for the wells in south Texas. The overburden stress is 13,000 psi, while the minimum horizontal stress is 12,495 psi.

The change in pore fluid pressure (ΔP_f) and the associated change in minimum horizontal stress (ΔS_h) are given as a gradient b. Therefore, the pore-pressure/-stress coupling gradient is,

b = (12495-10700)/(11829-9500)=0.77

For sand, according to the triaxial test, the internal frictional angle is 32.09º. It is assumed that there is no cohesion strength for the fault.

Three fault types are used to calculate the fluid-pressure levels required for induced faulting. From Figure 88, it is clearly shown that the fault slip type cannot be a reverse fault or strike-slip fault. If it is one of these two fault types, the initial pore pressure is less than the fluid pressure required for faulting. The fault has already slipped before production. A normal fault is the most likely occurring fault slip type. At a fault angle of 30º, the normal fault has the highest failure probability.

For sand, at the internal frictional angle of 32.09º, $\mu = 0.63$, the minimum pore pressure of 7,500 psi, and the faults are not going to slip. As the internal coefficient decreases from 0.63 to 0.51, the fault failure probability increases significantly (see Figure 89). With the internal coefficient of 0.51, the fault angle is between 16 and 46º (shown in red dash line) and the pressure required for activating faulting is between 10,000 and 8,000 psi. If the fault angle is decreasing into the red dashed line zone, the reservoir pressure can be depleted to 8,000 psi without activating the fault.

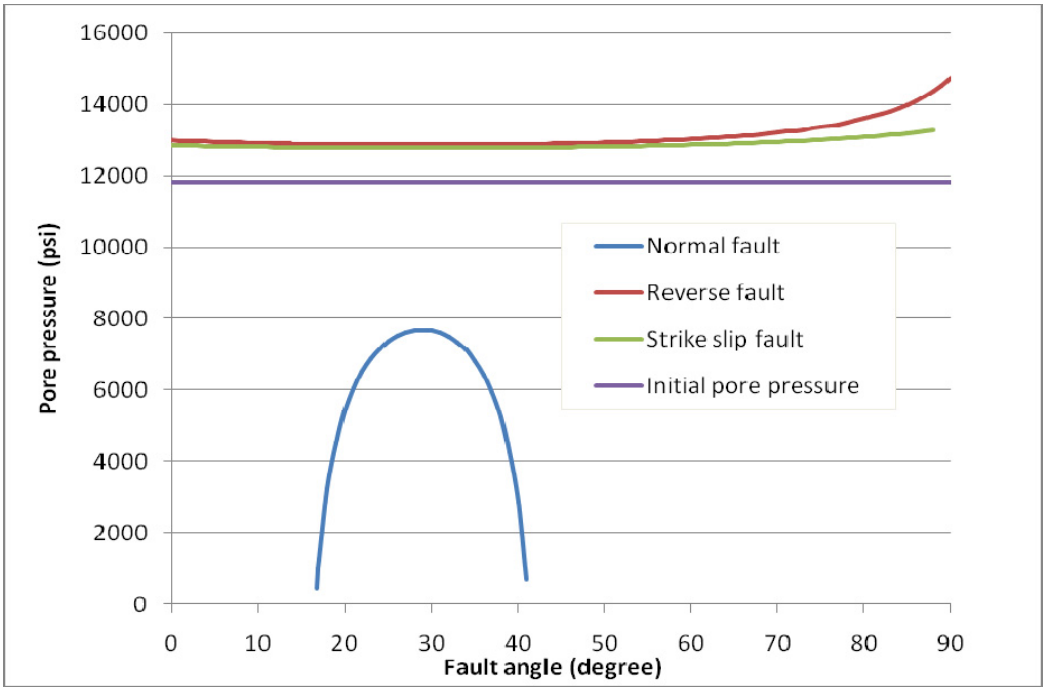

Figure 88 Fluid pressure required for fault activation

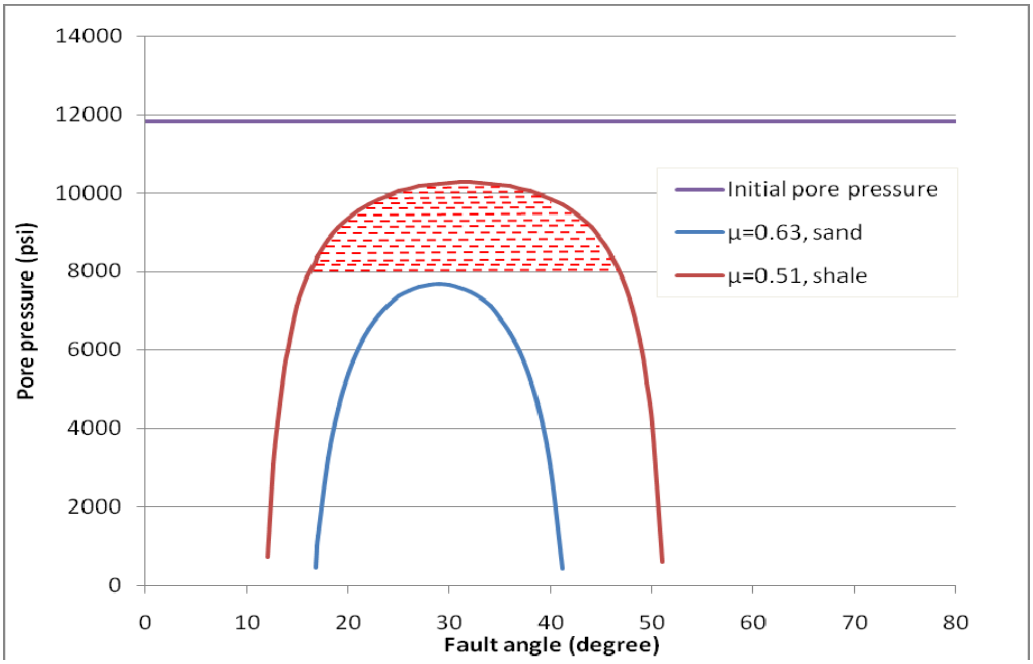

Figure 89 Fluid pressure required for activating faulting (normal fault)

7.4 Casing Perforation Section Collapse Analysis

From the statistical data, the perforation section of casing has the second highest failure probability. It is important to know the failure characteristics of this section. It is believed that in the perforation section of the casing, the cement fails first or the cement job is bad. Then, the perforated casing section is exposed to the reservoir pressure, and the inappropriate drawdown pressure causes the perforation section to collapse.

The casing perforation section was studied by FEM analysis. The von Mises failure criteria were used as the casing failure criteria. In the study, a 16-in. section of 5-in. OD, 23.2-lb/ft., P110 casing was used. The shot density/ft was 6, 4, and 3 with a perforation diameter from 0.3 in. to 0.7in. The distribution of the perforation holes is shown in Figure 90.

At a pressure of .070 psi, Figure 91 shows the von Mises stress distribution of 6 shots/ft casing section. The perforation diameter is 0.4 in. The maximum von Mises stress located around the perforation holes causes the stress intensity. At this pressure, the maximum von Mises stress

reaches 110,811 psi, which is beyond the nominal yield strength of 110,000 psi for P110 casing; therefore, the casing failed.

Table 14 shows the casing-collapse pressure. With the 0.3-in. diameter perforation and phase angle of 90^0, the casing has the highest collapse pressure of 9,285 psi. However, compared to the intact casing, the collapse pressure is 19,000 psi, and the collapse pressure of the perforation section is reduced significantly. With the 0.7-in. diameter perforation and phase angle of 120^0, the casing has the lowest collapse pressure of 7,990 psi.

It is recommended that for a 60º phase angle and 6-shots/ft density, a 0.3-in. diameter perforation is a better option than the other perforation designs. Though, the 90º phase angle, 4 shots/ft, 0.3-in. perforation has the highest collapse pressure of 9,285psi however, in commercial production, the 60º phase angle, 6 shots/ft, 0.3-in. perforation was a better choice. Irrespective of the perforation size and phase angle, the casing collapse pressure was reduced significantly compared to the intact casing. The bottomhole pressure should be maintained at a specific level to prevent casing collapse. For the wells, the 60º phase angle, 6 shots/ft, 0.3-in. perforation diameter, the pressure difference between the casing outside pressure and bottomhole pressure should be less than 9,280 psi, which means the maximum drawdown should not exceed 78.5%.

Table 14 Casing collapse pressure

Perforation, In.	Collapse Pressure, psi (60º Phase Angle, 6 shots/ft)	Collapse Pressure, psi (90º Phase Angle, 4 shots/ft)	Collapse Pressure, psi (120º Phase Angle, 3 shots/ft)
0.3	9,280	9,285	9,260
0.4	9,070	8,910	9,080
0.5	8,800	8,710	8,470
0.6	8,700	8,650	8,535
0.7	8,460	8,610	7,990

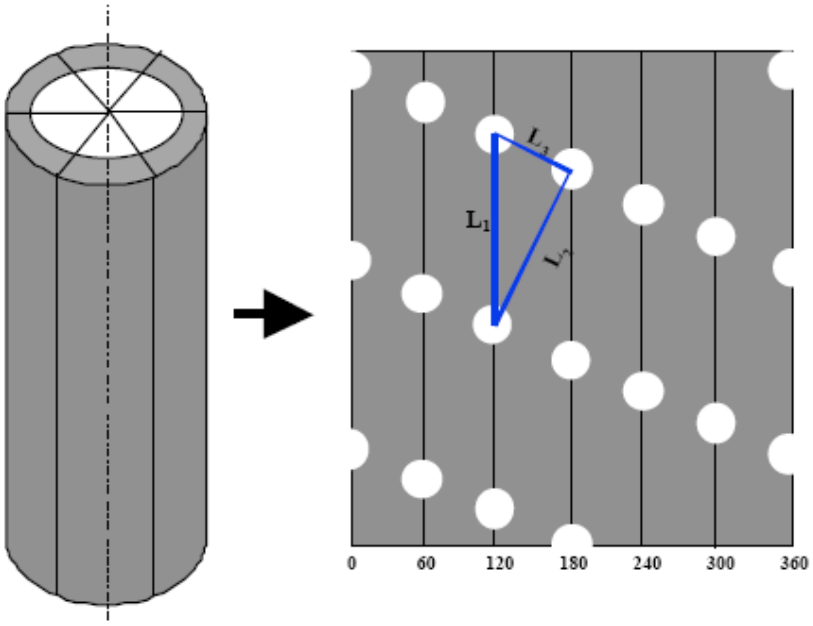

Figure 90 Perforation density of 6 shots/ft (60º phase angle) (Venkitaraman et al. 2000)

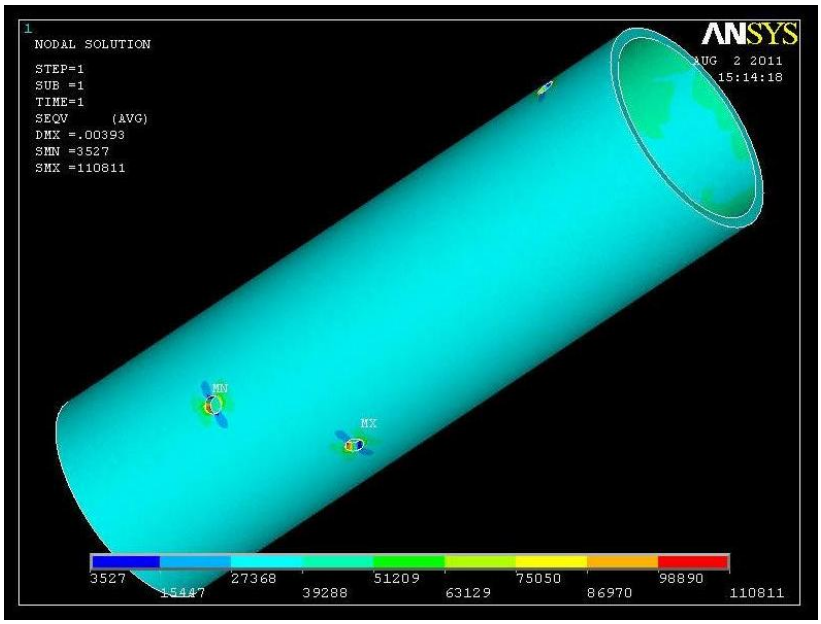

Figure 91 von Mises stress for 6 shots/ft and 60º phase angle

7.5 Well Operability Limits

With the production increases and reservoir pressure decreases, wellbore failure is always a possibility. . Production began without incident and resulted in drawdown and a decrease in pore pressure. This condition eventually led to rock failure in the region near the casing perforations and production of spalled rock material resulted through the perforations. Fine-sand production may have been preceded by production of fractured/collapsed cement. As the rock production continued, the void spaces behind the casing generated by production of cement and rock material increased. The rate of formation failure continued to increase as horizontal confining stresses decreased in response to more and more cavitations of the formation behind the casing.

Deformation and collapse of completion tubulars are affected by well drawdown, depletion, and rock geomechanical properties. Results from these relationships were used to develop a well operability limit (WOL). The WOL quantitatively defines the well integrity technical limit, and establishes the boundary between safe well production operations (green area) and collapse of completion tubulars under compaction loads, resulting from drawdown and depletion (area I, II, III, and IV). The failure types considered are formation failure, casing collapse, fault activation, and casing tension failure. In the WOL plots, areas I, II, III, IV represent 1, 2, 3, and 4 failure types occurring in that zone. Failure types at different drawdown and depletion pressure are shown in Table 16.

In area I, one phenomenon may occur such as formation failure or fault activation; however, if the operation in this zone is of short duration, the failure problems maybe not occur. In other areas, the number of failure type increases from two to four in area II, III, and IV. Operations in the area of II, III, and IV most likely causes failure problems.

Total vertical stress variation is calculated by the Equation (7.10) and Equation (7.11).

$$\Delta S_v = \alpha \Delta P_b \frac{1-2\nu}{1-\nu} \frac{\ln\left(h/R_b\right)}{\ln\left(R_d/R_b\right)} \tag{7.10}$$

where ΔS_v is the change of the total vertical stress, α is the Biot-Willis coefficient, ΔP_b is the drawdown defined as the pore pressure at the wellbore wall minus the pore pressure at the edge of the drawdown area, v is Poisson's ratio, h is the reservoir thickness, R_d is the radius of the drawdown area, and R_b is the wellbore radius.

$$\alpha = 1 - \frac{C_r}{C_{bc}} \tag{7.11}$$

where C_r is the volumetric solid-grain compressibility and C_{bc} is the volumetric bulk-volume compressibility at a constant pore pressure.

The compressive strength of rock is calculated as follows:

$$\sigma = \frac{2c\cos(\phi) + P_p(1+\sin(\phi))}{1-\sin(\phi)} \tag{7.12}$$

where c = cohesion strength in psi; φ= internal frictional angle in º; P_p = pore pressure in psi.

In this study, it is assumed that when the reservoir compacts, the casing developed the same strain as the formation. If the strain of the casing is higher than 0.2%, the casing fails. Based on the test data, α was considered to be 0.82, 0.9, and 0.95, respectively for sand, shaly sand, and shale.

At different original pore pressures, the stress at the formation with 0.2% strain was different. The relationship between the stress at 0.2% strain and the pore pressure is assumed to be linear, which w is shown in Figure 92, Figure 93, and Figure 94.

According to the triaxial test data, at the depth of 13,000 ft, the WOL was plotted for the wells according to Table 15. For three different formation properties, sand, shaly sand, and shale, there are three different WOLs, which are shown in Figure 95, Figure 96, and Figure 97. Shale has the lowest WOL, and at a 30% depletion, the well reaches the failure zone. Shaly sand has the highest WOL, and the well reaches the failure zone at the 90% depletion level. For sand, the WOL is between that of shaly sand and shale. In zone I, a single failure phenomenon occurs. If the operation takes place in this zone, the operation time should be as short as possible.

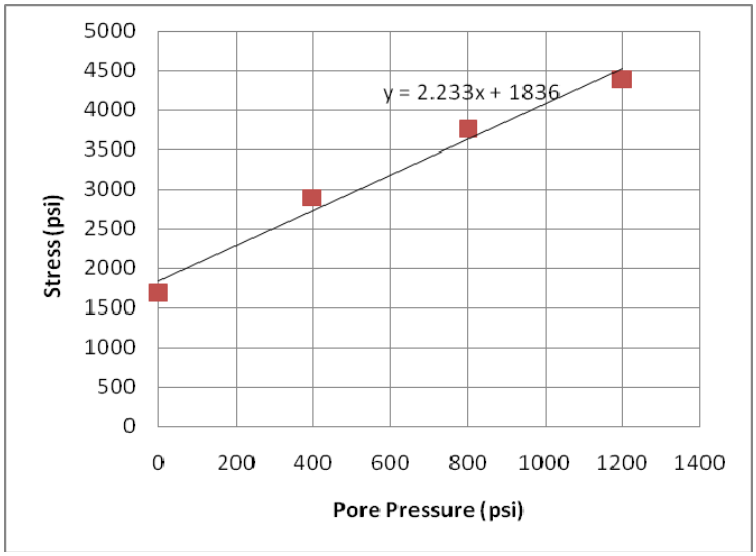

Figure 92 Formation critical stress and pore pressure (shaly sand)

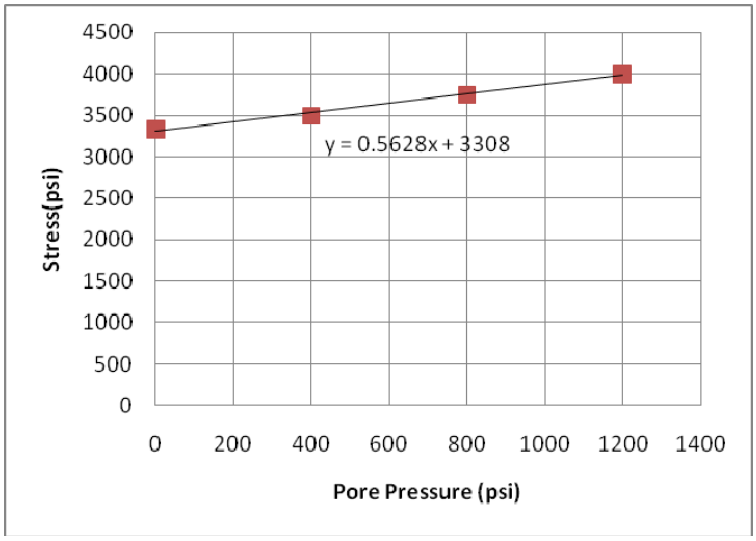

Figure 93 Formation critical stress and pore pressure (sand)

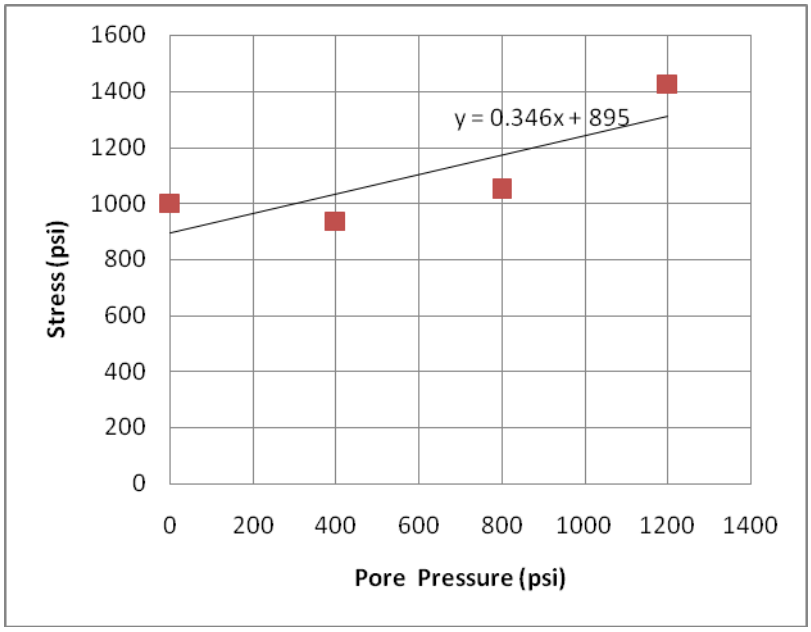

Figure 94 Formation critical stress and pore pressure (shale)

Table 15 Failure types at different drawdown and depletion pressures

	Drawdown% (Zero Depletion)		**Depletion% (Zero Drawdown)**		
	Casing Collapse	Formation Failure	Fault Activation	Formation Failure	Casing Tension Failure
Shale	78.5	73.5	28	64.8	59.87
Sand	78.5	88.2	49.3	73.7	70
Shaly Sand	78.5	91.9	89.1	87.1	>100

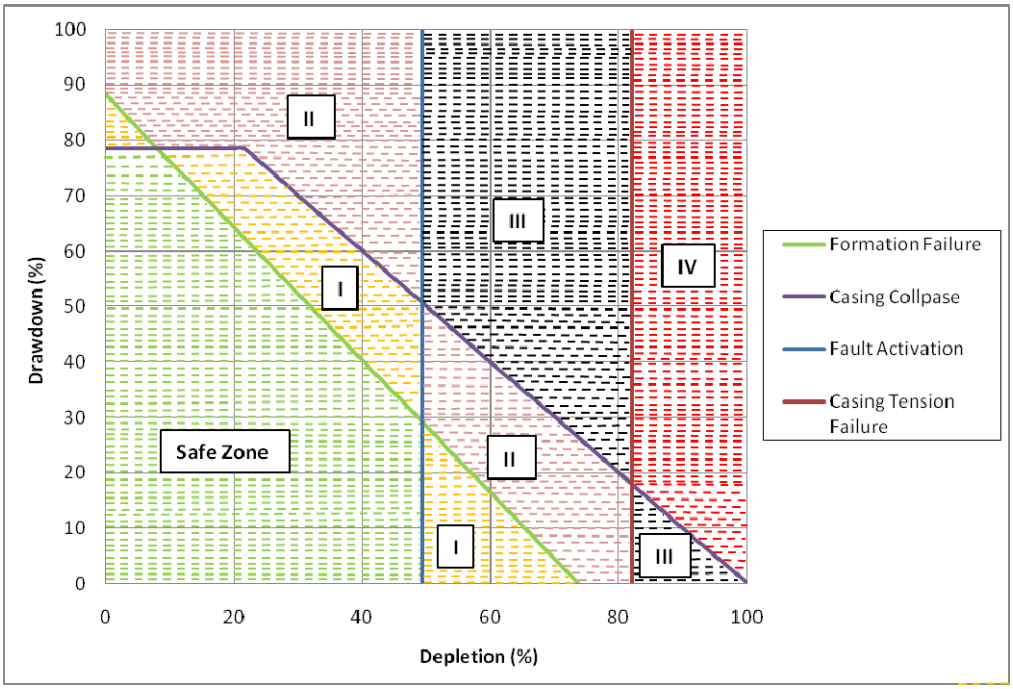

Figure 95 Sand formation workability operational limits

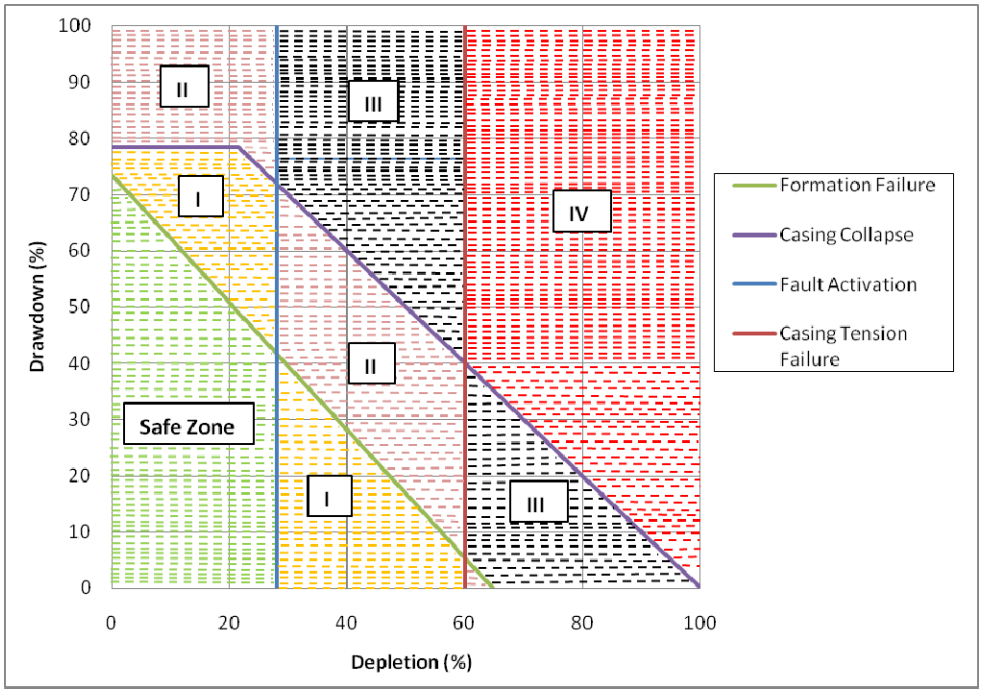

Figure 96 Shale formation workability operational limits

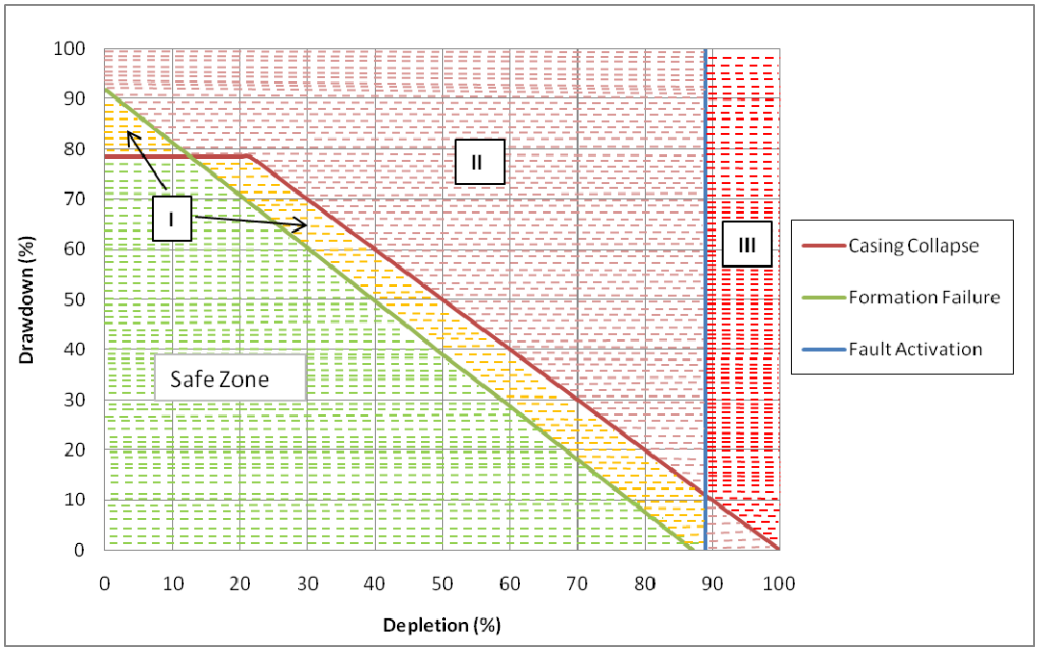

Figure 97 Shaly sand formation workability operational limits

7.6 Economic Analysis

In this analysis, a typical production forecast for the wells was used to estimate the production rate and production time. This forecast was built based on the offset wells in the block and the following considerations were taken into account:

(1) Initial production rates are expected to be 3 MMcf/D and 300 BOPD. (2) A work-over job is considered to be performed at month 12 to increase the production rate by incorporating new production zones (upper section sands). (3) The ultimate gross recovery of gas and oil is estimated to be 1.46 Bcf, and 111M BOD, respectively in 84 months (production life). (4) The forecast assumes a collapse failure at 36 months and a new pay zone will be opened after the failure. (5) The condensate yield for these wells is anticipated to be 76 bbl/MMcf as an average.

Figure 98 shows a production rate forecast under the old design in which it was safe to produce within 28 months (green line I). This safe time matches our statistical analysis, which reveals that most of the wells fail within 36 months after the spud time.

Regarding drilling improvement and new completion design, the well could produce for 42 months (50% extra life) (yellow line II) and the well may produce for 84 months (final production life) (red line III).

At the green line, the reservoir depletion is 67.8%, cumulative gas production is 1.1 Bcf, and cumulative oil production is 89,868 bbl. The reservoir depletion is 77.7%, cumulative gas production is 1.26 Bcf, and cumulative oil production is 99,855 bbl at the yellow line. At the red line, the reservoir depletion is almost 90%, final cumulative gas production is 1.46 Bcf, and final cumulative oil production is 111,190 bbl. Table 16 shows the final cumulative production at the different time lines. Extra production time varies from 14 months to 56 months. Extra cumulative gas production went from 160 to 360 MMcf, and additional cumulative oil production varies from 9,987 to 21,322 bbl.

Economical evaluations were carried out to verify the differences between the theoretical case described previously (84 months) and two hypothetical cases, the first assuming 28 months (statistical analysis) and other with 50% additional production time (42 months). Furthermore, this case considers extra costs due the recommendations incorporated in the well design. This evaluation was carried out to verify the changes in economical indexes like net present value (NPV) and internal rate of return (IRR). Table 17 shows NPV at the before tax (BTX) of 10%,

15%, and 20%, NPV, and IRR. The NPV increased 30% from the 28-month case to the 42-month case. Overall, the new design is applicable and additional profits can be achieved.

Table 16 Extra production time and cumulative production

	Old Design	**New Design**		**Extra Production Time**	**Extra Cum. Production**
	Green line I	**Yellow line II**	**Red Line III**		
Time	28	42	84	14 to 56 months	----------
Net Cum. Gas	1.10 Bcf	1.26 Mcf	1.46 Bcf	----------	0.16 to 0.36 Bcf gas
Net Cum. Oil	89,868 bbl	99,855 bbl	111,190 bbl	----------	9,987 to 21,322 bbl oil

Table 17 NPV Value

Scenarios	NPV Value			IRR
	BTX 10%	BTX 15%	BTX 20%	
Theoretical Case	3,307	2,725	2,228	53
28 Months, Collapse	1,701	1,368	1,069	43
42 Months, Collapse	2,316	1,884	1,503	48

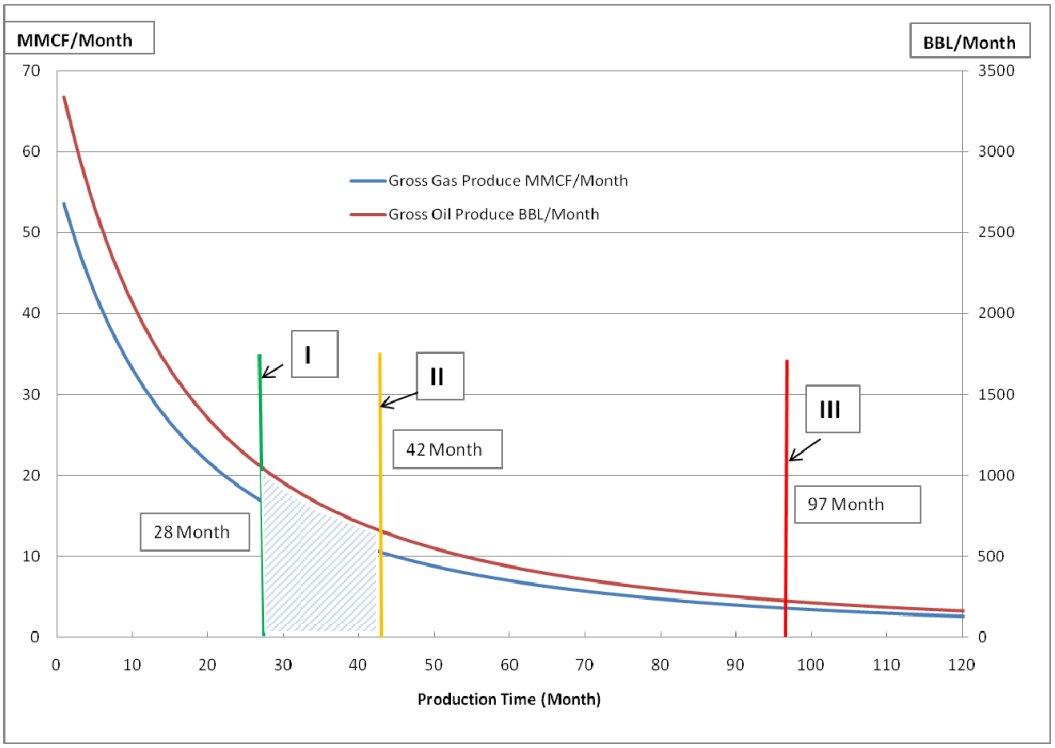

Figure 98 Gross production rate prediction

7.7 Conclusions

(1) A shale formation around the wellbore will begin to collapse at a shear stress of approximately 5,500 psi in 32 months after the start of production. Minimum allowable pore pressure around the casing is on the order of 2,000 psi. If pore pressure around the wellbore decreases below 2,000 psi, casing collapse is likely to occur because of formation failure.

(2) Normal fault is the most likely occurring fault slip type. At the fault angle of 30º, the normal fault has the highest failure probability. For a sand formation, at the internal friction angle of 32.09º, the pore pressure decreases below 7,680 psi and the faults begin to slip. For a shale formation, as the internal coefficient decreases to 0.51, the fault failure probability increases significantly. At the fault angle between 16 and 46º, the pore pressure is between 8,000 to 10,000 psi, and the faults begin to slip.

(3) Comparing to the intact casing, the collapse pressure of the perforation section is reduced significantly. It is recommended that the 60º phase angle, 6 shots/ft, and 0.3-in. perforation hole diameter is the best option. The bottomhole pressure should be maintained at some level to prevent casing collapse. Without cement, the casing collapse pressure is 9,280 psi. Under good cement conditions, the cement can hold some stress.

(4) Shale has the lowest WOL. The maximum drawdown is 65%, and at the depletion of 28.3%, the well reaches the failure zone. Shaly sand has the highest WOL. The maximum drawdown is 89.1%, and the well reaches the failure zone at a depletion of 90%. For sand, the WOL is between that of shaly sand and shale.

(5) Under the new design, the service life of the wells will most likely increase significantly. The extra well service life is 14 months to 69 months. Extra cumulative gas production is from 160 to 360 MMcf, and extra cumulative oil production is from 9,987 to 21,322 bbl. The new design is applicable and additional revenue can be obtained.

CHAPTER VIII

CONCLUSIONS AND DISCUSSIONS

8.1 Conclusions

(1) The class G cement experimental tests provide an excellent package of data that can be used when mechanical studies on cement, like FEM analysis, are required. It had been observed by our study that under low-temperature conditions, the mechanical properties of cement became independent of time so that these values (stabilized values) can be easily used for integrity calculations.

(2) At temperatures below 300ºF, the temperature has minor effects on the cement low-cycle fatigue. The elastic strain and plastic strain developed by thermal stress in cement is very small compared to the strain developed by the bottomhole pressure under the low-cycle fatigue range. The cement with higher Poisson's ratio and lower Young's modulus shows better low-cycle fatigue behavior compared with lower Poisson's ratio and higher Young's modulus cement. Within the requirements of compressive strength, the cement with higher plasticity is preferred for HPHT wells and steam-injection wells.

(3) The cement maximum von Mises stress and the cement maximum shear stress are sensitive to the cement's Young's modulus and the formation's Young's modulus. The casing eccentricity alone does not have much effect on the casing and cement. The maximum von Mises stress difference is only 0.27% for the 0.3-in. eccentricity when the casing is centered in the borehole. For the stresses developed in the cement, voids in the center of the cement, voids near the casing, and 0.3-in. eccentricity and cement channel are the three worst cases in regard to the cementing complications.

(4) In the long term, 72-lbm/ft^3 cements show improvement in the stress reduction with time. The 72 lbm/ft^3-cement failure probability decreases with time because the cement shear stress, tensile stress, and compressive stress all decrease with time. The 101-lbm/ft^3 cement and 118-lbm/ft^3 cement do not clearly show improvement with time. The highest failure probability zone is between a borehole angle of 40 and 50º.

(5) The new equation proposed by the FEM results can better predict casing critical buckling strain than can the Euler's method. The critical buckling strain decreases as the unsupported

casing length increases. For different casing wall thickness, the critical buckling strain is almost identical.

(6) Normal fault is the most likely fault slip type in south Texas wells. At a 30º fault angle, the normal fault has the highest failure probability. Shale has the lowest WOL and a maximum drawdown of 65%. At 28.3% depletion, the wells reach failure zone. Under the new design, the service life of the wells will likely increase significantly. The increased well service life is between 14 and 69 months.

.

8.2 Discussions

(1) Cement plastic and creep behavior needs to be further studied because under high-confining pressure, the cement behaves similar to a plastic. The relationship between the confining pressure and the cement plastic behavior is not well understood.

(2) For the results by our study to be applied in geothermal wells in the low-cycle cement fatigue experimental study, additional tests need to be performed between 300 and 600ºF.

(3) For 72-lbm/ft^3, 101-lbm/ft^3, and 118-lbm/ft^3 cement, additional tests need to be carried out. In the present study, only one sample was tested under the same condition. In the future, three samples should be tested under the same condition would be a better option.

(4) In the FEM analysis method, the fluid flow from the reservoir into the wellbore and the reservoir properties also need to be considered in the simulation. In this situation, the casing, cement behavior, and the reservoir simulation would be studied in the same model.

(5) The shear strength of the interface between the casing and the cements, the cement types, and the formation under high-confining pressure need to be studied. Some tests had been carried out for the shear strength of the interface between the casing and the cement and the cement and the formation under zero confining pressure. There is a significant difference between the interface behavior under zero confining pressure and high-confining pressure.

REFERENCES

Abaqus Technology Brief. 2009. Helical Buckling of Coiled Tubing in Directional Oil Wellbores. March.

Ahmed S.A., Meng F., Noble J. and Guo Q. 2003. Modeling of Reservoir Compaction and Casing Integrity Evaluation Using Reservoir Simulation. SPE 81072 presented at the SPE Latin American and Caribbean Petroleum Engineering Conference, 27-30 April, Port-of-Spain, Trinidad and Tobago.

Alliche A. and Francois D. 1986. Fatigue Behavior of Hardened Cement Paste. Cement Concrete Res. 16, 199-206.

Antrim J.D. 1968. The Mechanism of Fatigue in Cement Paste and Plain Concrete. Highway Research Record. 210, 95.

Atkinson C., and Eftaxiopoulos D. 1996. A Plane Model for The Stress Field around an Inclined, Cased and Cemented Wellbore. International Journal for Numerical and Analytical Methods in Geomechanics. 20, 549-569.

Barry W., David B., Lennox L. and Bill H. 2009. The Application of High-Density Elastic Cements To Solve HP/HT Challenges in South Texas: The Success Story. SPE 122762 presented at the SPE Annual Technical Conference and Exhibition, 4-7 October, New Orleans, Louisiana.

Berger A., Flecknestein W. and Eustes A. 2004. Effect of Eccentricity, Voids, Cement Channels, and Pore Pressure Decline on Collapse Resistance of Casing. Paper SPE 90045 presented at the SPE Annual Technical Conference and Exhibition, 26-29 September, Houston, Texas.

Bernard P., Keith L., Elton B., Rick S. and Aidar Z., et al. 2002. Support Requirements and Innovative Solutions for a Remote Location with Difficult Cementing Challenges. Paper IADC/SPE 74501 presented at the IADC/SPE Drilling Conference, Dallas, Texas, 26-28 February.

Chen Y., Lin Y. and Cheatham J. 1990.Tubing and Casing Buckling in Horizontal Wells. J. Petrol. Technol. 42, 140-141.

Chia Y.P. and Bradley D.A. 1989. Evaluation of Reservoir Compaction and Its Effects on Casing Behavior. SPE Prod. Eng. 5, 167-172.

Christian H., Hassan E., Husam H., Hasni A., and Mohsen A. 2001. Innovative Solution for Cementing Across Very Low Fracture Gradient Formations. Paper IADC/SPE 72286 presented at the IADC/SPE Middle East Drilling Technology, Bahrain, 22-24 October.

Christopher L., Ryan D. and Marcus G. 1990. Cement Channeling: How To Predict and Prevent. SPE Drilling Engineering, 5, 201-208.

Couturler M., Guillot D., Hendriks H. and Callet F. 1990. Design Rules and Associated Spacer Properties for Optimal Mud Removal in Eccentric Annuli. Paper SPE 21594 presented at the CIM/SPE International Technical Meeting, 10-13 June, Calgary, Alberta, Canada.

Daniel P. N., Ben H. T., Hamid K., and Dwight T. D. 2001. Probabilistic Risk Analysis of a Cemented Hip Implant. J. Math. Modeling Scientific Computing. 13, 98–108.

Dawson R. and Paslay P.R. 1984. Drillpipe Buckling in Inclined Wells. J. Petrol. Technol. 36, 1734-1738.

Eric M. and Bipin J. 1997. Using Concrete Technology to Improve the Performance of Lightweight Cements. Paper SPE/IADC 39276 presented at the SPE/IADC Middle East Drilling Technology Conference, Bahrain, 23-25 November.

Ferda A., Shedid A. and Hamed A. 2004. Simulation Investigation of Casing Eccentricity Estimation for Different Inclination Angles and Tensile Forces Using Finite Element Method. Paper SPE 91811 presented at the SPE International Petroleum Conference in Mexico, 7-9 November, Puebla Pue., Mexico.

Goodwin K.J., and Crook R.J., 1992. Cement Sheath Stress Failure. SPE Drilling Engineering. 7, 291-296.

Hart P.E. and Wilson L.C. 1990. Improved Channel Repairs with Small-Phased Circumferential Perforating Guns. Paper SPE 20424 presented at the SPE Annual Technical Conference and Exhibition, 23-26 September, New Orleans, Louisiana.

Jaeger J.C. and Cook N.G.W. 1969. Fundamentals of Rock Mechanics. First Edition. London.

Jeffrey T., Simon J., Ortega J. and Simone M., et al. 2012. Fundamental Investigation of the Chemical and Mechanical Properties of High-Temperature-Cured Oilwell Cements. Paper OTC 23688 presented at the Offshore Technology Conference, Houston, Texas, 30 April-3 May.

Jiang W. and Martin E. K. 2008. Casing Failure in Cyclic Steam Injection Wells. IADC/SPE 114231 presented at IADC/SPE Asia Pacific Drilling Technology Conference and Exhibition, 25-27 August, Jakarta, Indonesia.

Joao C.R., Ademar P., Luiz P. and Ilson P. 1997. Stress Analysis of Casing String Submitted to Cyclic Steam Injection. SPE 38978 presented at Fifth Latin American and Caribbean Petroleum Engineering Conference and Exhibition, 30 August-3 September, Rio de Janeiro, Brazil.

John H. 1965. Strength of Oil Well Cements at Downhole Pressure Temperature Conditions. J. Petrol. Technol. 5, 341-347.

Joshi Y., Dhang N. and Pandey B. 2004. Probability Analysis of Fatigue of Paving Concrete. J. Inst. Eng. 85(11), 163-168.

Laidler A., Taoutaou S., Johnson C.R. and Quisel N. 2007. A Risk Analysis Approach Using Stress Analysis Models to Design for Cement Sheath Integrity in a Multilateral Well. Paper

IPTC 11059 presented at International Petroleum Technology Conference, 4-6 December, Dubai, U.A.E.

Le S., Baumgarte C., Thiercelin M. and Vidick B. 2000. New Cement Systems for Durable Zonal Isolation. Paper IADC/SPE 59132 presented at the IADC/SPE Drilling Conference, 23-25 February, New Orleans, Louisiana

Lilja M. 2009. Nonlinear Finite Element of a Geothermal Well. Master of Science Thesis, University of Iceland.

Manoochehr S., Min J., Yang J., Ahmed R. and Bahman T. 2010. Effect of Casing Eccentricity on Casing Stability Analysis in Wellbores Drilled in Gas Hydrate Bearing Sediments. Paper SPE 131236 presented at the SPE EUROPEC/EAGE Annual Conference and Exhibition, 14-17 June, Barcelona, Spain.

Manson S. 1966. Thermal Stress and Low Cycle Fatigue. New York.

Morris W., Marcelo C., Robles J. and Gustavo B. 2003. Design of High Toughness Cement for Effective Long Lasting Well Isolations. Paper SPE 81001 presented at the SPE Latin American and Caribbean Petroleum Engineering Conference, 27-30 April, Port-of-Spain, Trinidad and Tobago

Murdock J.W. 1965. A Critical Review of Research on Fatigue of Plain Concrete. University of Illinois Engineering Experiment Station, Bulletin 475, February.

Nabipour A.and Joodi B. 2010. Finite Element Simulation of Downhole Stresses in Deep Gas Wells Cements. SPE Paper 132156 presented at the SPE Deep Gas Conference and Exhibition, 24-26 January, Manama, Bahrain.

Nikolaus P., Charles W. and Jie T. 2007. Fatigue Failure in the Cement Mantle of a Simplified Acetabular Replacement Model. Int. J. Fatigue. 29, 1245-1252.

Paula R., Ribeiro P. and Santos O. 2009. HPHT Drilling—New Frontiers for Well Safety. Paper SPE 119909 presented at the SPE/IADC Drilling Conference and Exhibition, 17-19 March, Amsterdam, the Netherlands.

Philippacopoulos A.J., and Berndt M.L. 2001. Mechanical Property Issues for Geothermal Well Cements. Geoth. Res. T. 25, 119-224.

Rahman S.S. and Chilingar G.V. 1995. Casing Design Theory and Practice. New York.

Reddy B., Santra A., David M., Gray D., Chad B. and Rick D. 2005. Cement Mechanical-Property Measurements under Wellbore Conditions. Paper SPE 95921 presented at the SPE Annual Technical Conference and Exhibition, 9-12 October, Dallas, Texas

Rodriguez W.J., Fleckenstein W.W., and Eustes A.W. 2003. Simulation of Collapse loads on Cemented Casing Using Finite Element Analysis. Paper SPE 84566 presented at the SPE Annual Technical Conference and Exhibition, 5-8 October, Denver, Colorado.

Ross R., Kent S. and Ted R. 2001. A New Approach to and Old Problem-Lightweight Liquid Concrete Paper SPE 67193 presented at the SPE Production and Operation Symposium, 24-27 March, Oklahoma City, Oklahoma.

Shen X. 2010. Subsidence Prediction and Casing Integrity with Respect to Pore-Pressure Depletion with 3-D Finite Element Method. SPE 138338 presented at SPE Latin American & Caribbean Petroleum Engineering Conference, 1-3 December, Lima, Peru.

Silva M., Martins A., Barbosa B. and Garcia H. 1996. Designing Fluid Velocity Profiles for Optimal Primary Cementing. Paper SPE 36136 presented at the SPE Latin America/Caribbean Petroleum Engineering Conference, 23-26 April, Port-of-Spain, Trinidad.

Stenger B., Ameen M., AI-Qahtani S. and Pham T.R. 2002. Pore Pressure Control of Fracture Reactivation in the Ghawar Field, Saudi Arabia. Paper SPE 77642 presented at the SPE Annual Technical Conference and Exhibition, 29 September-2 October, San Antonio, Texas.

Stiles D. 2006. Effects of Long-term Exposure to Ultrahigh Temperature on the Mechanical Parameters of Cement. Paper IADC/SPE 98896 presented at the IADC/SPE Drilling Conference, 21-23 February, Miami, Florida

Streit J.E. 1999. Conditions for Earthquake Surface Rupture Along The San Andreas Fault System. Journal of Geophysical Research. 104, 17929-17939.

Streit J. E. and Hillis R.R. 2002. Estimating Fluid Pressures That Can Induce Reservoir Failure During Hydrocarbon Depletion. Paper SPE 78226 presented at the SPE/ISRM Rock Mechanics Conference, 20-23 October, Irving, Texas.

Streit J. E. and Stephen F. C. 2001. Fluid Pressures at Hypocenters of Moderate to Large Earthquakes. Journal of Geophysical Research. 106, 2235-2243.

Talal M., Abdullah S. and Mansour S. 1999. Increasing Well Life Cycle by Eliminating The Multistage Cementer and Utilizing a Light Weight High Performance Slurry. Paper SPE 53283 presented at the SPE Middle East Oil Show, 20-23 February, Bahrain.

Teodoriu C., Ugwu I. and Schubert J. 2010. Estimation of Casing-Cement-Formation Interaction Using a New Analytical Model. Paper SPE 131335 presented at the SPE EUROPEC/EAGE Annual Conference and Exhibition, 14-17 June, Barcelona, Spain.

Teodoriu C., Ulmanu V. and Badicioiu M. 2008. Casing Fatigue Life Prediction using Local Stress Concept: Theoretical and Experimental Results. SPE 110785 presented at SPE Western Regional and Pacific Section AAPG Joint Meeting, 31 March-2 April 2, Bakersfield, California.

Teodoriu C., Yuan Z., Schubert J. and Amani M. 2012. Experimental Measurements of Mechanical Parameters of Class G Cement. Paper SPE 153007 presented at the SPE/EAGE European Unconventional Resources Conferences and Exhibition, 20-22 March, Vienna, Austria.

Thiercelin M., Bernard D., Baret J. and Rodriquez W. 1997. Cement Design Based on Cement Mechanical Response. Paper SPE 52890 presented at the SPE Annual Technical Conference and Exhibition, 5-8 October, San Antonio, Texas

Venkitaraman A., Behrmann L., and Noordermeer A. 2000. Perforating Requirements for Sand Prevention. Paper SPE 58788 presented at the SPE International Symposium on Formation Damage Control, 23-24 February, Lafayette, Louisiana.

Wehling P. 2008. Wellbore Cement Integrity Testing. M.S. Thesis, Technical University of Clausthal

William M. 1965. Shear Failure of Rock under Compression. J. Petrol. Technol. 5, 167-176.

Wu J. and Hans J. 1995. Coiled Tubing Buckling Implication in Drilling and Completing Horizontal Wells. SPE Drill Completion. 10, 16-21.

Xie J. and Liu Y. 2008. Analysis of Casing Deformation in Thermal Walls. Abaqus User's Conference.

Yuan Z., Schubert J., Teodoriu C., and Gardoni P. 2012a. HPHT Gas Well Cementing Complications and its Effect on Casing Collapse Resistance. SPE 153986 presented at SPE Oil and Gas India Conference and Exhibition, 28-30 March, Mumbai, India.

Yuan Z., Abudullah A., Schubert J. and Teodoriu C. 2012b. Cement Failure Probability under HPHT Conditions Supported By Long Term Laboratory Studies and Field Cases. Paper SPE 154746 presented at the SPE Annual Technical Conference and Exhibition, 8 - 10 October, San Antonio, Texas.

APPENDIX

DERIVATION OF FLUID PRESSURE FOR FAULTING ACTIVATION

The formation stress state is shown in figure 99 and figure 100 and can be expressed in equation A.1.

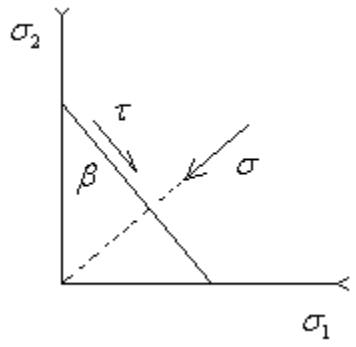

Figure 99 Formation stress state

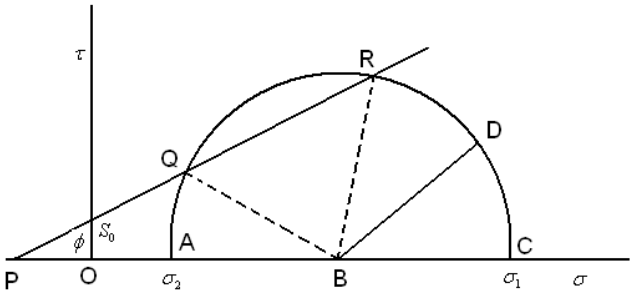

Figure 100 Formation Mohr-Columb failure envelope

$$|\tau| = S_0 + \mu\sigma \tag{A.1}$$

$$\sigma = \frac{1}{2}(\sigma_1 + \sigma_2) + \frac{1}{2}(\sigma_1 - \sigma_2)\cos(2\beta) \tag{A.2}$$

$$\tau = -\frac{1}{2}(\sigma_1 - \sigma_2)\sin(2\beta) \tag{A.3}$$

$$\sigma_m = \frac{1}{2}(\sigma_1 + \sigma_2) \tag{A.4}$$

$$\tau_m = \frac{1}{2}(\sigma_1 - \sigma_2) \tag{A.5}$$

$$\mu = \tan\phi \tag{A.6}$$

Substitute (A.5) into equation (A.3)

$$\tau = -\tau_m \sin(2\beta) \tag{A.7}$$

Substitute A.4 into equation (A.2)

$$\sigma = \sigma_m + \tau_m \cos(2\beta) \tag{A.8}$$

Substitute Equation (A.5), (A.6), (A.7), (A.8), into equation (A.1),

$$\tau_m\left(\sin(2\beta) - \tan\phi\cos(2\beta)\right) = S_0 + \sigma_m \tan\phi \tag{A.9}$$

(A.9) rewritten as

$$(\sigma_1 - \sigma_2)\left(\sin(2\beta) - \frac{\sin\phi}{\cos\phi}\cos(2\beta)\right) = 2S_0 + (\sigma_1 - \sigma_2)\frac{\sin\phi}{\cos\phi}$$

Reorganize

$$\sigma_1\left(\sin(2\beta) - \frac{\sin\phi}{\cos\phi}\cos(2\beta) - \frac{\sin\phi}{\cos\phi}\right) - \sigma_2\left(\sin(2\beta) - \frac{\sin\phi}{\cos\phi}\cos(2\beta) + \frac{\sin\phi}{\cos\phi}\right) = 2S_0$$

$$\begin{aligned} L.H.S. &= \sigma_1\frac{1}{\cos\phi}\left(\sin(2\beta)\cos\phi - \sin\phi\cos(2\beta) - \sin\phi\right) - \sigma_2\frac{1}{\cos\phi}\left(\sin(2\beta)\cos\phi - \sin\phi\cos(2\beta) + \sin\phi\right) \\ &= \sigma_1\frac{2}{\cos\phi}\left(\sin\beta\cos\beta\cos\phi - \cos^2\beta\sin\phi\right) - \sigma_2\frac{2}{\cos\phi}\left(\sin\beta\cos\beta\cos\phi - \cos^2\beta\sin\phi + \sin\phi\right) \\ &= \sigma_1(1 - \mu\cot\beta)\sin(2\beta) - \sigma_2(1 - \mu\cot\beta)\sin(2\beta) + 2\mu\sigma_2 \\ &= (\sigma_1 - \sigma_2)(1 - \mu\cot\beta)\sin(2\beta) + 2\mu\sigma_2 \end{aligned}$$

Finally,

$$\sigma_1 - \sigma_2 = \frac{2S_0 + 2\mu\sigma_2}{(1 - \mu\cot\beta)\sin(2\beta)} \tag{A.10}$$

In three dimension,

$$\sigma_1 - \sigma_3 = \frac{2C + 2\mu\sigma_3}{(1 - \mu\cot\beta)\sin(2\beta)}$$

According to figure 101, Θ=90-β

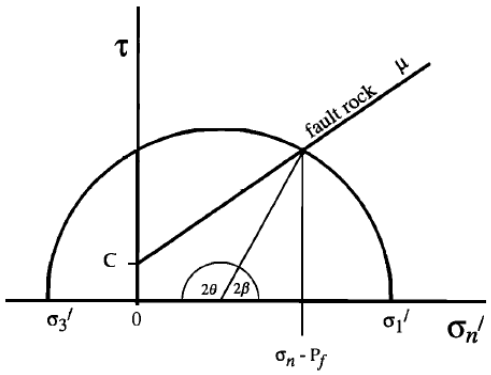

Figure 101 Formation Mohr-Columb failure envelope with effective stress

$$\sigma_1 - \sigma_3 = \frac{2C + 2\mu\sigma_3'}{(1 - \mu\tan\theta)\sin(2\theta)}$$

Considering mean effective stress

$$\sigma_m' = \frac{1}{2}(\sigma_1' + \sigma_3')$$

$$\frac{\sigma_1 - \sigma_3}{2}(\sin(2\theta) + \mu\cos(2\theta)) = C + \mu\left(\frac{\sigma_1' + \sigma_3'}{2}\right)$$

Then the effective minimum principal stress is obtained,

$$\sigma_3^{'} = \frac{-2C + (\sigma_1 - \sigma_3)(1 - \mu \tan\theta)\sin(2\theta)}{2\mu}$$

For normal faulting, the maximum principal stress is obtained by adding the stress difference at failure to the value of the minimum principal stress

$$\sigma_1^{'} = \frac{-2C + (\sigma_1 - \sigma_3)(1 - \mu \tan\theta)\sin(2\theta)}{2\mu} + (\sigma_1 - \sigma_3)$$

Then $\lambda_v = \frac{\sigma_1^{'}}{\sigma_1} = \frac{\sigma_1 - P_f}{\sigma_1} = 1 - \frac{P_f}{\sigma_1} = \frac{-2C + (S_1 - S_3)(1 - \mu \tan\theta)\sin 2\theta}{S_1 2\mu} + \frac{(S_1 - S_3)}{S_1}$

The above equation is the same as equation (7.4) in Chaper VII.

From equation, (7.5), (7.6), (7.7), (7.8), (7.9) in Chaper VII.

Then, for normal fault, the fluid pressure required for faulting activation.

$$P_f = P_{f0} - \frac{-2C + 2\mu P_{f0} - \mu S_{h0} - S_{h0}\sin 2\theta}{2\mu - b\mu - b\sin 2\theta - b\mu\cos 2\theta} - \frac{-\mu S_{h0}\cos 2\theta + S_v \sin 2\theta - \mu S_v 2(\sin\theta)^2}{2\mu - b\mu - b\sin 2\theta - b\mu\cos 2\theta}$$